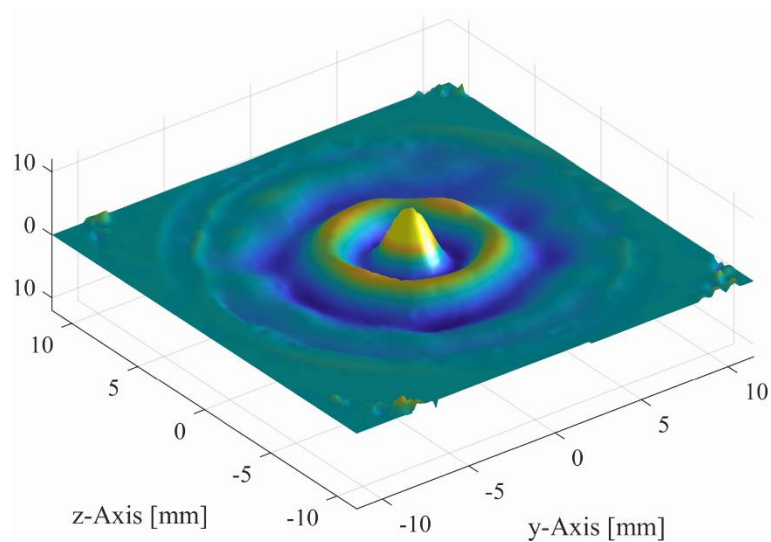


Investigation of Focused Transducers for Air-Coupled Ultrasound Testing



Scientific Thesis for Obtaining the Degree

B. Sc.

at the Munich School of Engineering of the Technical University of Munich

Examiner Prof. Dr.-Ing. Christian Große
Chair of Non-destructive Testing

Supervisor M. Eng. Janez Rus
Chair of Non-destructive Testing

Handed in by David Kulla

████████████████████

████████████████

Submitted 21.02.2019

Assignment Definition

Task specification for Bachelor's thesis

Title: Investigation of Focused Transducers for Air-Coupled Ultrasound Testing

Supervisor: Janez Rus, M. Eng.

Tel: +49 89289 27041

janez.rus@tum.de



Preliminary work and motivation:

The conventional ultrasound testing methods have been established since a long time for the defect characterization of the production parts, however their potential for the automatization is limited due to the coupling problem. Contrarily, the contact-free defect detection using so-called air-coupled ultrasound (ACU) does not require a couplant medium. This allows a faster and more cost-efficient performance of the tests. Challenges of the ACU testing methods result from the large acoustic impedance differences at the solid-material interfaces that cause large sound intensity losses. For this reason, powerful ultrasound sources, in the combination with the sufficiently sensitive receivers are required. According to the previous researches, a so-called optical microphone manufactured by the company Xarion and the piezo composite transmitter of the company Sonotec are considered suitable.

To fully utilize the potential of this measurement concept, the measurement chain components, their arrangement and the measurement data processing algorithms should be optimized.

Assignment Definition

The measurements take place at the chair of Non-destructive Testing, Centre for Building Materials in München-Pasing. The linear motion CNC table, the piezoelectric transmitters, the optical microphone and a laser-doppler vibrometer are provided.

Task and objective:

An optimization of the measurement system for air-coupled ultrasound testing with the optical microphone should be carried out with a special emphasis on the excitation parameter of the piezoelectric transmitter. The source should be characterized regarding its emitted sound field and surface movement.

Key tasks of the thesis:

- Study of the related topic with a reference to the previously conducted works
- Familiarization with the measurement setup
- Evaluation, analysis and interpretation of the data
- Characterization of the utilized ultrasound transmitters (sound field and surface movement)
- Measurement data validation regarding the measurement accuracy and measurement sensitivity

Requirements:

- Preliminary knowledge of non-destructive material testing methods
- Enjoyment of experimental work
- Knowledge of MATLAB is advantageous
- Ability to work independently and structured

The evaluation criteria are provided to the student. The thesis is accomplished with the written composition under consideration of the chair's layout and the submission of all the documents and the measurement data in the electronic form.

Conclusively a 30-minute presentation of the results is carried out at the chair, and the ensuing grading process is carried out. The corrected final version of the thesis is available to the examiners at least 10 days in advance.

Begin of the Bachelor thesis: immediately

Probable duration: 6 months

Declaration of Independence

Kulla, David

[REDACTED]

[REDACTED]

[REDACTED]

I hereby declare that I have written the present bachelor thesis independently. No other sources and aids than those given in the work were used. I have marked the literal or analogous citations.

This bachelor thesis was written under the scientific and content-related guidance of my supervisor. Central ideas and concepts were developed jointly with him.

Munich, February 11th, 2019

Kulla, David

Kurzfassung

Die luftgekoppelte Ultraschallprüfung hat das Potential, viele Prüfaufgaben realisierbar zu machen, die mit konventioneller Ultraschalltechnik nicht möglich sind. Ein hoher Automatisierungsgrad ist mit luftgekoppelter Ultraschallprüfung möglich, da keine Zeit für Anbringen und Abtragen eines Koppelmediums benötigt wird. Außerdem dürfen einige Materialien, z.B. Holz, nicht mit Flüssigkeiten in Verbindung gebracht werden, was eine Prüfung mit konventionellem Ultraschall unmöglich macht. Nachteilig für die Prüfung mit Luftultraschall ist die hohe akustische Fehlanpassung von Luft und Festkörpern, die zu großen Verlusten der Schallintensität bei der Materialprüfung führt. Daher wurden spezielle Prüfköpfe für den Luftultraschall entwickelt, die verschiedene Fokussierungsmechanismen verwenden, um die Effizienz der Schallerzeugung zu steigern.

In dieser Arbeit wurde eine senderseitige Untersuchung des luftgekoppelten Ultraschallprüfsystems vorgenommen. Dazu wurden fünf Prüfköpfe betrachtet: zwei planare Prüfköpfe, zwei sphärische Prüfköpfe und ein elektronisch fokussierter Prüfkopf mit separat ansteuerbaren Elektroden. Die Untersuchung erfolgte mit zwei Messinstrumenten: Einem optischen Mikrofon und einem Laser-Doppler Vibrometer. Mit dem optischen Mikrofon wurden zunächst die Schallfelder der Prüfköpfe vermessen. Daraus konnten die Nahfeld- bzw. Fokusslänge, der maximale Schalldruck und der Öffnungswinkel des Schallfeldes bestimmt und mit Herstellerangaben und theoretisch berechneten Werten verglichen werden. Diese verschiedenen erhobenen Werte weisen für jeden Prüfkopf eine große Diskrepanz auf, wohl aufgrund von fehlenden Normen, Fehlern in den Berechnungsformeln und nicht beobachteten systematischen Fehlern in der Messung.

Das Laser-Doppler Vibrometer wurde zur Charakterisierung der Oberflächenbewegung zweier Prüfköpfe verwendet. Die maximalen Geschwindigkeiten und Auslenkungen konnten aus den Daten gewonnen werden. Durch die hohe örtliche Auflösung war zudem eine Identifikation von einigen Moden möglich. Abschließend wurde eine Untersuchung des elektronisch fokussierten Prüfkopfes hinsichtlich der optimalen Phasenverschiebung der einzelnen Elektroden vorgenommen. Eine gute Übereinstimmung mit den vom Hersteller gemessenen Schallfeldern wurde beobachtet. Die Ergebnisse deuten darauf hin, dass die Fokussierung nicht durch Schallwellen in Luft, sondern durch Oberflächenwellen auf dem Prüfkopf erzeugt wird.

Die gewonnenen Daten und Erkenntnisse werden als Grundlage für eine weiterführende Untersuchung der Schallfelder mit Computersimulationen verwendet werden. Dies sollte auch die Diskrepanz in den Werten für die Schallfelder erklären.

Schlagwörter:

Luftultraschall, Schallfeldcharakterisierung, Optisches Mikrofon, Laser-Doppler-Vibrometer, Eigenmoden, phased-array, fokussiert, Prüfkopf

Abstract

Air-coupled ultrasound testing has the potential to realize many inspection tasks which are not possible with conventional ultrasonic methods. A high automatization is possible when using air-coupled ultrasound, as no time is needed applying or removing a coupling medium. Furthermore, some materials such as wood may not be subjected to liquids, making inspection with conventional ultrasound impossible. The high mismatch of the acoustic impedance between air and solids is disadvantageous for testing with air-coupled ultrasound, as it leads to high intensity losses when testing materials. Due to this fact, special transducers were developed for air-coupled ultrasound, which use different means of focusing to increase the efficiency of sound generation.

In this work a transducer sided investigation of the air-coupled ultrasound testing system was conducted. Five transducers were evaluated: two planar transducers, two spherical transducers and one electronically focusing transducer with separately controllable electrodes. Measurements were done with two devices: an optical microphone and a laser-doppler vibrometer. The sound fields of the transducers were firstly recorded with the optical microphone. Near field or focal lengths, the maximum sound pressure and the opening angle of the sound field were obtained and compared to the manufacturer specifications and to the theoretically calculated values. The differently obtained values deviated considerably for each transducer, potentially due to missing norms, errors in the equations or unobserved systematic errors in the measurements.

The laser-doppler vibrometer was used to characterize the surface movement of two transducers. The maximum velocities and displacements were obtained. The high spatial resolution additionally permitted an identification of some mode shapes. A concluding investigation of the electronically focused transducer concerning the optimal phase shift between the individual electrodes was carried out. A good agreement with the sound field data published by the manufacturer was observed. The results indicate that the focusing effect is not created by interfering sound waves in air but by surface waves on the transducer.

The obtained data will be used as a basis for a pursuing investigation of the sound fields with computer simulations. This should also clarify why the observed deviation between theoretical and experimental values occurred in the sound fields.

Keywords:

Air-coupled ultrasound, sound field characterization, optical microphone, laser-doppler vibrometer, mode shapes, phased array, focused, transducer

Table of Contents

Assignment Definition.....	I
Declaration of Independence.....	III
Kurzfassung.....	IV
Abstract.....	V
Table of Contents	VI
List of symbols.....	VIII
List of abbreviations	X
1 Introduction	1
2 Physical Principles.....	3
2.1 Properties of Sound	3
2.1.1 Sound Waves in Gases and Solids	3
2.1.2 Sound Pressure	5
2.1.3 Transmission and Reflection at Interfaces	5
2.1.4 Sound Attenuation.....	7
2.2 Generation of Ultrasound with Piezo Electric Elements	8
2.2.1 Piezoelectric Effect	8
2.2.2 Properties of Piezoelectric Materials	9
2.2.3 Structure of Piezoceramic Transducers.....	10
2.2.4 Ideal Sound Fields.....	11
2.2.5 Vibration Modes of Clamped Circular Plates	13
2.3 Optical Microphone.....	15
2.3.1 Pressure Dependency of Refractive Index	15
2.3.2 Structure and Functioning Principle.....	16
2.3.3 Internal Signal Processing and SNR	17
2.4 Laser Doppler Vibrometer.....	18
2.4.1 Heterodyne Interferometer	18
2.4.2 Decoders for Velocity and Displacement	19
3 Experimental Setup.....	21
3.1 Measurement Hardware.....	21
3.1.2 3-Axis CNC Machine and Coordinate System	21

3.1.3	Signal Generator and Amplifier.....	22
3.1.4	Utilized Transducers	23
3.1.5	Oscilloscopes	29
3.2	Scanning Measurement Configurations	30
3.3	Post-Processing of Measured Data	34
3.3.1	Data Visualization Methods	34
3.3.2	Filters and Averaging	37
3.3.3	Optimization of Data Conversion.....	39
3.4	Signal Flow and Disturbances in the Measuring Process	41
4	Results and Discussion.....	44
4.1	Transducer Sound Fields.....	44
4.1.1	Time-Evolving Sound Fields.....	44
4.1.2	Power Distribution of Sound Fields	52
4.2	Transducer Surface Scan.....	57
4.2.1	Mode Identification	58
4.2.2	Power Distribution and Inhomogeneities	67
4.3	Optimal Phase Shift for Electronically Focused Transducer	70
4.3.1	Theoretical Calculation.....	70
4.3.2	Experimental Validation.....	72
5	Conclusion	75
	Literature	78
	List of figures	82
	List of tables	85
	Appendix	86

List of symbols

Symbol	Unit	Basis-SI Units	Definition
c	[m / s]		Sound velocity
d	[m / V] or [C / N]	[m / V] or [C s ² / (kg m)]	Piezoelectric charge constant
a	[m]		Aperture radius
D	[m]		Transducer diameter
D	[C / m ²]		Dielectric displacement
E	[Pa]	[kg / (m s ²)]	Elastic modulus
h	[m]		Max. distance of chord and arc
f	[Hz]	[1 / s]	Frequency
J	[W / m ²]	[kg / s ³]	Sound intensity
K	[Pa]	[kg / (m s ²)]	Compression modulus?
M	[kg / kmol]	[kg]	Molar mass
N	[m]		Near-field length
L	[dB]	[-]	Sound pressure level
n	[-]		Refractive index
k	[1 / m]		Wave number
p	[Pa]	[kg / (m s ²)]	Pressure
i	[-]		Counting index
l	[m]		General length
R	[-]		Reflection coefficient
R	[J / (K mol)]	[(kg m ²) / (K mol s ²)]	Universal gas constant
R _s	[m]		Spherical radius
r	[m]		Radius (of a transducer)
ε	[-]		Strain
T	[-]		Transmission coefficient
T	[K]		Temperature
t	[m]		Thickness (of a transducer)
t _p	[s]		Phase shift
T	[s]		Period duration
S _R	[-]		Specific refractivity
Z	[Rayl]	[kg / (m ² s)]	Acoustic impedance
κ	[-]		Isentropic exponent

μ	[-]		Poisson's number
σ	[Pa]	[kg / (m s ²)]	Mechanical stress
ρ	[kg / m ³]		Density
λ	[m]		Wave length

List of abbreviations

ACU	Air-coupled ultrasound
CFRP	Carbon-fiber reinforced polymer
CLSM	Confocal laser scanning microscope
ECR	Event-controlled recording
LDV	Laser doppler vibrometer
NDT	Non-destructive testing
OPD	Optical path difference
RMS	Root mean square
SNR	Signal-to-noise ratio
SPL	Sound pressure level
PVDF	Polyvinylidene fluoride

1 Introduction

Non-destructive testing methods are increasingly used for quality control during production as well as in practical use. They have the inherent advantage over destructive testing methods that a total monitoring is possible, which is important for composite materials in complex geometries and many other materials. Ultrasound is especially popular under these NDT methods, as it is fast, cheap, easily applicable and there exist many sophisticated methods for data processing and interpretation. However, in conventional ultrasound applications, a liquid coupling medium is needed since the acoustic impedance of air is magnitudes away from that of any solid, leading to high losses at the interfaces. The necessity of a liquid in turn limits the potential of ultrasound in highly automated production processes and can prevent this method from being used at all, e.g. for materials like wood and porous materials which must not be subjected to water or gels.

The development of systems for air-coupled ultrasound has made testing various materials possible and promises to facilitate the automated testing by removing the need for extra coupling media. These systems use ultrasound transducers specifically designed for generating sound in air alongside low-noise amplifiers to overcome the extremely high sound energy losses. The first applications of this technology date back to the 1990s [Rogovsky 1991], however progress has mostly been made due to advances in piezo ceramic materials. The establishment of new broadband emission [Klaas Bente et al. 2018] and detection [Fischer 2016] methods has led to new possibilities in detecting flaws.

Three previous works have focused on researching these methods at the chair for non-destructive testing [Gamper 2017, Guruschkin 2015, López Baos 2018]. Special attention was paid to the so-called optical microphone, which can receive ultrasound over a wide frequency spectrum. The microphone called ETA 250 Ultra was compared to conventional ACU systems and was investigated intensively for its potential in testing various materials by Gamper (2017). He found out that it can detect smaller defects than the conventional receivers, i.e. it has a higher resolution. However, the microphone's sensitivity limited its use in highly attenuating materials such as CFRP plates, where the conventional transducers yielded more significant results. López Baos (2018) installed the prototype of a new version of the optical microphone (ETA 450 Ultra) at the chair for non-destructive testing alongside a complete system for testing plates. This microphone has a highly increased sensitivity, making it suitable to test even CFRP plates.

Since the prototype of the new Eta 450 Ultra used by López Baos (2018) was destroyed in an accident, it could not be used in this work. Due to this fact, it was decided to focus on the piezoceramic transducers used in the ACU setup and research their properties, especially of their sound fields and surface movement. The optical microphone is well-suited

for the recording of sound fields, as it has a small aperture and it is the only device that can deliver quantitative information on the pressure levels of sound at frequencies over 200 kHz [Steinhausen 2019].

This work aims to contribute to the questions how the ACU transducers can be used to their full potential and what data characterizing the transducer oscillation can be extracted. Specifically, what geometric changes to the measurement setup can be made, how does a phased array transducer for ACU work and what is the validity of the obtained data?

The data obtained of the transducer oscillation behavior will then be used as input for simulating the test setup and the sound fields will serve as a reference to compare the simulation results to. The simulations will be carried out by Ming Huang (Imperial College, London).

2 Physical Principles

This chapter gives an overview of the physical principles relevant to this work. Firstly, sound waves and their properties are introduced. Secondly, ultrasound is covered in more detail, focusing on its generation through piezo electric transducers and properties of piezo electric materials. This is followed by an explanation of the devices used to acquire experimental data, which are the optical microphone and the laser-doppler vibrometer. Here, the focus will lay on the different interferometers and signal processing.

2.1 Properties of Sound

In this section, the general properties of sound waves are introduced and discussed regarding the topic of this work.

Sound is, in contrast to light or other electromagnetic waves, bound to a medium. Sound waves cannot be transferred in empty space as there are no particles present which can oscillate. The following relation of frequency f , wavelength λ and sound velocity c is valid:

$$f \cdot \lambda = c. \tag{2.1}$$

2.1.1 Sound Waves in Gases and Solids

In solids, the two wave types depicted in Figure 2.1 can propagate. Longitudinal waves oscillate in the direction of propagation, causing a local change of normal stress, i.e. pressure. Therefore, they are also called *pressure* or *P-waves*. For transversal waves, the direction of oscillation is perpendicular to the propagation direction. To be able to transfer these *S-waves*, it is necessary for a material to support *shear* forces, which is the case for all solids and few liquids. Most fluids (most liquids and all gases) are not able to transfer shear forces, and therefore only longitudinal waves occur in them. Both wave types presented so far propagate in three-dimensional, infinite media. In real, finite parts other wave types can be excited, such as surface and plate waves which propagate at an interface surface and have especially low amplitude attenuation.

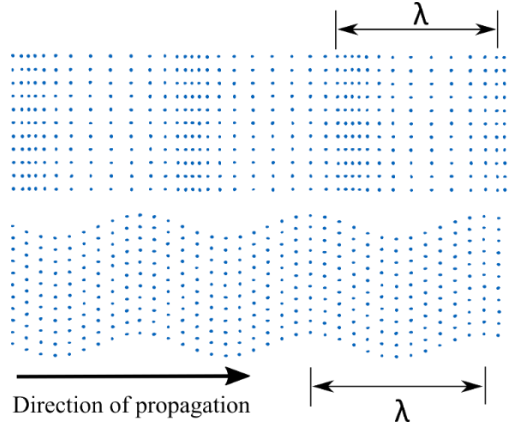


Figure 2.1: Wave types. Upper part: Longitudinal wave, lower part: Transversal wave.

Speed of sound

Longitudinal and transversal waves have, if they can be transmitted by the medium, different velocities. The longitudinal wave velocity is higher than the transverse velocity for all solid materials [Krautkrämer & Krautkrämer 1990]. For isotropic and nondispersive solids, the velocities for longitudinal and transversal sound waves can be expressed in terms of the density ρ , Young's modulus E and Poisson's constant μ :

$$c_L = \sqrt{\frac{E(1 - \mu)}{\rho(1 + \mu)(1 - 2\mu)}}. \quad (2.2)$$

$$c_T = \sqrt{\frac{E}{2\rho(1 + \mu)}}. \quad (2.3)$$

For ideal gases, the following relation

$$c = \sqrt{\frac{\kappa RT}{M}} = \sqrt{\frac{K}{\rho}}. \quad (2.4)$$

holds. Therefore, the (longitudinal) sound velocity can be calculated with the isentropic exponent κ , the universal gas constant R , the temperature T and the molar mass M of the gas or gas mixture. It can also be calculated with the *adiabatic compression modulus* K and the density ρ as in the second part of the equation, which furthermore holds for all liquids and gases. From the first part of equation (2.4) it can be observed that changes in temperature and molar mass influence the sound velocity. The molar mass of air is related to humidity; however, this is negligible compared to the influence of the temperature on the speed of sound. Table 2.1 shows sound velocities for selected temperature-humidity pairs, where this is visible. For comparison, values for water and two piezo electric materials are included.

Table 2.1: Sound velocities for air (at different temperatures and values of humidity), water and piezo electric materials. With data from [Krautkrämer & Krautkrämer 1990].

Material	Speed of sound c [m/s]
Air at 0 % relative humidity, 0 °C	331.4
Air at 0 % relative humidity, 20 °C	343.3
Air at 100% relative humidity, 0 °C	331.7
Air at 100 % relative humidity, 20 °C	344.3
Water (at 20 °C)	1483
Lead zirconate titanate	3800 - 4200
PVDF	1500 - 2600

2.1.2 Sound Pressure

For longitudinal waves, the sound pressure p can be described as the quotient of total normal force F acting on a surface (such as the eardrum) with an area A :

$$p = \frac{F}{A}. \quad (2.5)$$

A similar definition can be made for transversal waves, where the normal force is replaced with the shear force acting over the same surface.

The ambient pressure with $p_{\text{Ambient}} \approx 10^5$ Pa is large even compared to the maximum sound pressures of up to 200 Pa encountered in everyday life. Additionally, typical sound pressures have a very large amplitude range, making it suitable to use the logarithmic sound pressure level (SPL) to be able to differentiate sound levels at different magnitudes. The use of the SPL is further justified by the logarithmic perception of sound levels through the human ear [Hirsh 1952]. It is defined as follows:

$$L_p = 20 \cdot \log_{10} \left(\frac{p}{p_0} \right). \quad (2.6)$$

The SPL is expressed in the unit decibels (dB), where the sound pressure p is related to the reference pressure $p_0 = 2 \cdot 10^{-5}$ Pa which corresponds to the hearing threshold of a human ear at a frequency of 1 kHz. In this scale, a sound pressure change of 1 dB is just about noticeable by humans.

2.1.3 Transmission and Reflection at Interfaces

Interfaces play an important role when analyzing the sound waves, since all significant properties change abruptly. Generally, when an incident wave with sound pressure p_i coming from Medium 1 hits an interface, there will be a transmitted wave propagating into Medium 2 and a

reflected wave in Medium 1 with reversed direction, which is visualized in Figure 2.2. To predict the exact behavior of sound at an interface, the *acoustic impedances* Z of the materials comprising the interface are essential. The acoustic impedance is calculated as the product of material density ρ and longitudinal velocity of sound c . Acoustic impedances of different materials have a large range of about five magnitudes. Gases for example have both a lower density and lower sound velocity than liquids or solids due to the atoms in gases having greater distances from each other and no direct connection apart from random collisions. This causes the acoustic impedance of gases to be consistently lower than that of solids or liquids.

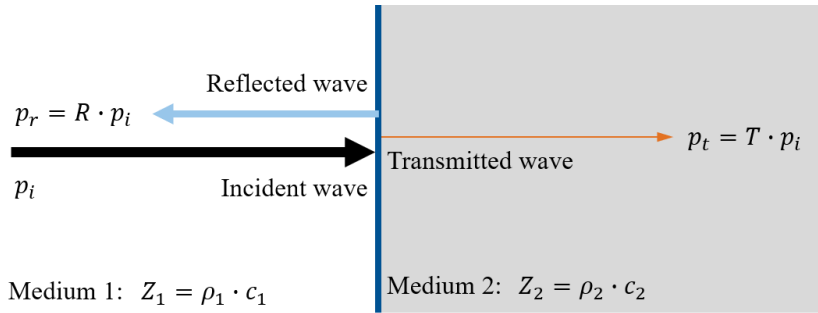


Figure 2.2: Schematic of sound waves at an interface.

Depending on the acoustic impedances of the involved materials, the sound pressure of the reflected and transmitted wave can be calculated with the reflection and transmission coefficients R and T from eqn. (2.7) for an incident wave perpendicular to the interface with initial sound pressure p_i (see Figure 2.2). Here, Z_1 refers to the acoustic impedance of the material with the incident sound wave, and Z_2 to the material in which the transmitted sound wave propagates.

$$R = \frac{Z_2 - Z_1}{Z_2 + Z_1} \quad \text{and} \quad T = \frac{2Z_2}{Z_2 + Z_1} \quad (2.7)$$

If Z_2 is large compared to Z_1 , it is possible for the transmission coefficient to reach approximately 2. Conversely, if Z_1 is much larger than Z_2 the reflection coefficient tends to -1. This at first seems to violate the conservation of energy, however the sound energy is not calculated with pressure only, but also relates to the acoustic impedance of the material. This becomes clear with the definition of the *sound intensity* J , which expresses the sound energy per unit of time and area (2.8).

$$J = \frac{1}{2} \frac{p^2}{Z}. \quad (2.8)$$

Here, the sound pressure p and the acoustic impedance Z of the material are needed.

Instead of having the incident energy (or sound intensity) equal the sum of reflected and transmitted intensities in an energy balance, in the case of sound pressure the terms must be summed according to the material the waves propagate in, i.e. the sum of incident and re-

flected pressures equals the sound pressure of the transmitted wave. This balance can be written in terms of reflection and transmission coefficients:

$$1 + R = T \quad (2.9)$$

If the incident wave is not perpendicular but oblique to the surface normal, the transmission and reflection coefficients as well as the angles of the transmitted and reflected wave may be calculated by modifying eqn. (2.7) with Snellius' law. In this case, mode conversions can take place at the surface (depending on the materials) and the resulting waves are a superposition of longitudinal and transversal waves.

2.1.4 Sound Attenuation

Ideally, sound pressure is only reduced by geometric means like the increasing surface of a spherical wave emitted from a point source. Here, the pressure decreases inversely with the distance to the source. This factor is called divergence and can be compensated for by means of focusing (see 2.2.4). In all real materials however, there are scattering and absorption effects acting in varying degrees to decrease the sound pressure further. These mechanisms are together called *attenuation* and in some cases *extinction* [Krautkrämer & Krautkrämer 1990].

Scattering is caused by inhomogeneities in the material. These inhomogeneities can be caused by genuine flaws (cracks, foreign inclusions) or intentional ones such as gas pores in foam-like materials. Some materials have an inherently inhomogeneous structure, such as cast iron, or metal alloys with differently orientated grains. At the interface of these inhomogeneities, the incident sound wave is diverted into many reflected and transmitted wave types, causing the original sound beam to be split up more and more. These partial sound waves are then absorbed along their prolonged paths through true absorption. The ratio of wavelength to the size of the inhomogeneity (called grain size in the next paragraph) is very important in this process, as it determines the amount of scattered sound energy.

“In the case of grain sizes of 1/1000th to 1/100th of the wavelength, scatter is for all practical purposes negligible. It increases very rapidly however, approximately as the third power of the grain size, to make itself felt at sizes from 1/10th to the full value of the wavelength, to such an extent that testing may become impossible if the material concerned is anisotropic” [Krautkrämer & Krautkrämer 1990].

True absorption is caused by a multitude of processes converting sound energy into random molecular or atomic movement (heat). For fluids, there are three main causes for this: Inner friction through high dynamic viscosity, heat transfer due to non-adiabatic nature of pressure, density changes in the sound wave, and molecular absorption where sound energy gets transferred into rotational or oscillating molecular movements [Lerch et al. 2009].

Absorption can be compensated for with higher transmission power or higher gain on the receiver side. The same cannot be done to influence the impact of scattering, as the amount of scattering increases with increasing power of the sound wave. To reduce scattering as well as absorption losses, lower frequencies can be used, as these sound waves with larger wavelengths are less influenced by attenuation mechanisms. This does however also limit the detectability of defects and therefore reduces the attainable resolution, as the minimum detectable defect can be estimated with one half of a wavelength.

In air and other fluids, the main factor causing attenuation of sound waves is true absorption. This true absorption is frequency dependent for sound waves above 100 kHz [Álvarez & Kuc 2008], resulting in a dispersive behavior where phase and group velocities are different.

2.2 Generation of Ultrasound with Piezo Electric Elements

Here, the principles for generating ultrasound waves in air relevant to this work will be introduced. According to [Lerch et al. 2009], ultrasound is defined as sound with frequencies between 10 kHz and 1 GHz and therefore mostly cannot be perceived by the human ear.

2.2.1 Piezoelectric Effect

Piezoelectric materials can be used to convert an alternating electrical voltage into a sound wave and vice versa. This is described by the so called direct piezoelectric effect or the inverse piezoelectric effect, respectively. The direct piezoelectric effect is caused by the alignment permanent dipoles through an external force, resulting in an electric voltage. The so-called inverse piezoelectric effect describes the physical deformation (with volume change) of a piezoelectric material caused by an externally applied voltage. If the direction of the force or the direction of the electrical field changes, the respective other quantity will change as well. In conventional ACU testing systems both the inverse and direct effect are used for transmission and detection purposes, respectively. If one uses the optical microphone for the detection, only the inverse piezoelectric effect is necessary to create the ultrasound wave.

For the inverse effect, the strain ε produced inside the material is proportional to the applied electrical field E . It is appropriate to use the piezoelectric charge constant d to fully relate strain and field strength. In equation (2.10), d is expressed in meters/volt [Panda 2017]. The charge constant can also be expressed in terms of the dielectric displacement D (equal to the total charge per unit area) and the mechanical stress σ .

$$d = \frac{\varepsilon}{E} = \frac{D}{\sigma} \quad (2.10)$$

A numerically identical charge constant can again be defined for the direct piezoelectric effect but with unit coulomb/newton. High charge constants result in a more effective generation of sound waves and are therefore desirable for this application.

2.2.2 Properties of Piezoelectric Materials

In the following, monolithic piezo ceramics are firstly introduced with focus of their ability of generating sound in air. Then, piezo composites comprising of piezo ceramics and polymers are presented and discussed with the same focus.

Piezo Electric Ceramics

Piezo Electric ceramics are the de-facto standard when it comes to ultrasound generation in conventional applications, where coupling media are used. There are commercially available raw materials and assembled transducers for most applications. Broadly used piezo ceramics include barium titanate and lead zirconate titanate (PZT) [Krautkrämer & Krautkrämer 1990]. Like most ceramics, they are brittle and stiff, thus requiring careful handling of the transducers manufactured from these materials. Due to their mechanical properties as solids, piezo ceramics have a very high acoustic impedance mismatch with gases, particularly with air. Sound velocities for two piezo electric materials are given in Table 2.1. Together with the density, an acoustic impedance of about $30 \times 10^6 \text{ Ns/m}^3$ can be calculated. This is about five magnitudes greater than the impedance of air at 20 °C with about 414 Ns/m^3 . Pure piezo electric ceramics are therefore not suitable for emitting high sound powers in air which are needed for material testing.

In ultrasound testing, many transducers are polarized in their thickness direction to emit longitudinal waves. To estimate the first eigenfrequency of a plate-shaped piezo ceramic, the following formula can be employed (2.11). This is usually the frequency of the excitation voltage.

$$f_0 = \frac{c_L}{2t} \quad (2.11)$$

Here, c_L is the longitudinal sound velocity in the piezo material and t is the thickness of the plate.

Piezo Electric Composites

Piezo electric composites are typically manufactured in the “dice and fill” technique. A piezo ceramic plate first is sawed in cuts parallel to each other and then sawed again after a rotation by 90°. The depth of the cuts is typically 80 % of the plate thickness. This yields an orthogonal array of small piezoceramic elements fixed on the base plate. The notches are then filled with a polymer material and undergo a heat treatment. The electrodes are applied next in for example a sputtering and galvanization process. If the transducer is to be physically focused, the composite is shaped spherically in the next process step. It is important to note that the sawing can cause the piezoelectric material to become partially depolarized.

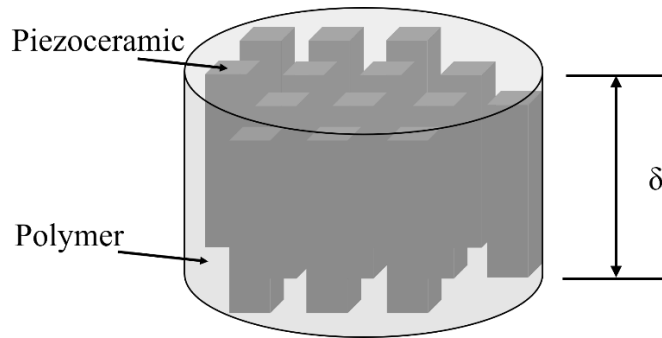


Figure 2.3: Schematic of a plate made from piezo-composite material.

The properties of the piezo composite vary with the ratio of piezoceramic to polymer matrix [Zhang et al. 2018]. Generally, the longitudinal wavelength and the acoustic impedance of the composite will increase with the fraction of piezoceramic material in it, since the ceramic is stiffer than the polymer and thus can transfer sound waves quicker. It is important to note that the middle-to-middle distance of the individual rods must be smaller than half of the shear wave’s wavelength of the polymer matrix for the composite to be able to vibrate uniformly [Stößel 2004].

2.2.3 Structure of Piezoceramic Transducers

The principle structure of a transducer for air-coupled ultrasound can be obtained from Figure 2.4. Each functional part will be explained from left to right. It may be advantageous to employ an (inductive) matching coil to facilitate excitation by the amplifier and transform the voltage supplied to the transducer. This increases the oscillation amplitude, and thus also the power output [Stößel 2004].

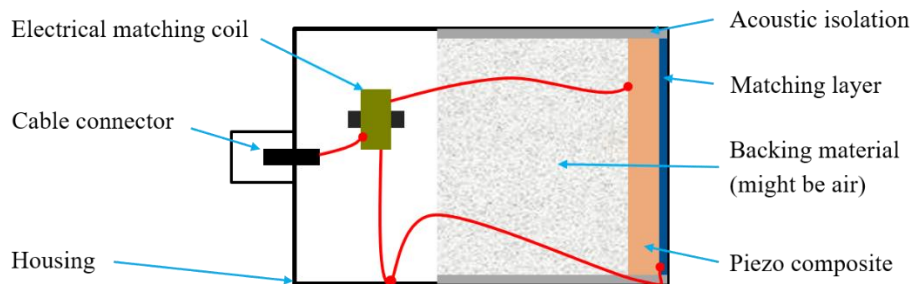


Figure 2.4: Structure of an ACU-transducer. Augmented representation following [Gamper 2017]

To change the oscillation behavior of the piezo element, it can be fixed to a damping material. This increases the transducer’s bandwidth as shorter pulses become possible, but the damping material also decreases the total power output. Therefore, in some transducers for air-coupled ultrasound a specific damping material is omitted, and the transducer is instead “air-backed”. As the acoustic difference between piezo element and air is greater than the difference between piezo element and the matching layer, thus more sound is emitted at the

front. This does however lead to increased pulse lengths compared to transducers with a solid backing material

As explained in section 2.2.2, piezoelectric materials have a high impedance mismatch compared to air. To improve the transmission coefficient from material to air, a matching layer can be used. Theoretically, this layer enables a full transmission of the sound energy. Its optimal acoustic impedance would be equal to the geometric mean of the impedance of the transducer and that of air. In practice however, a material with this acoustic impedance does not exist. Efforts are being made to develop materials with acoustic impedances close to the desired value and additionally with low attenuation coefficients. Porous soft rubber materials are promising candidates for this application, but are hard to manufacture and attach to the transducer surface [Alvarez-Arenas 2004].

The thickness of the matching layer t_{ML} should be optimally adjusted during manufacturing. A formula for calculating the ideal thickness is given in equation (2.12). It is proportional to the wavelength of sound in the matching layer λ_{ML} [Stöbel 2004]. Optimal transmissivity occurs when the initial and reflected waves are out of phase by $\lambda/2$. As whole wave lengths do not add to the phase shift, various optimal thicknesses can be found. It should be noted that in practice the maximum thickness of the matching layer is limited by attenuation.

$$t_{ML} = \frac{\lambda_{ML}}{4} (2i + 1) \text{ with } i \in \mathbb{N} \quad (2.12)$$

Perfect transmission only occurs for one desired frequency as the thickness depends on the wavelength. Thus, the matching layer acts as a narrow-band filter. This can result in so-called “ringing” where a sound pulse is prolonged and emitted in a narrow frequency range.

2.2.4 Ideal Sound Fields

According to Huygen’s principle, every point on a sound emitting surface can be seen as a source for an elementary wave. To construct the amplitude at an arbitrary point in front of this surface (inside the sound field), the elementary waves are superimposed according to their frequency and phase. A differentiation between the near field and the far field can be made when characterizing sound fields, as illustrated in Figure 2.5.

A point in the near field has large differences in its distances to the points on the transducer surface. Therefore, the phases of the elementary waves differ by a large margin, causing constructive and destructive interferences to appear. In the range of the near field length one last maximum occurs and the sound beam is constricted to its minimum, forming a focused area. The near field length of a plane circular surface can be calculated according to this equation [Deutsch et al. 1997]:

$$N = \frac{r_s^2}{\lambda} = \frac{f \cdot d_s^2}{4 \cdot c} \quad (2.13)$$

Here, r_s is the radius of the surface and λ the wavelength of the emitted sound. The frequency of the surface is denoted with f , d_s is the diameter of the surface and c is the sound velocity inside of the medium of propagation.

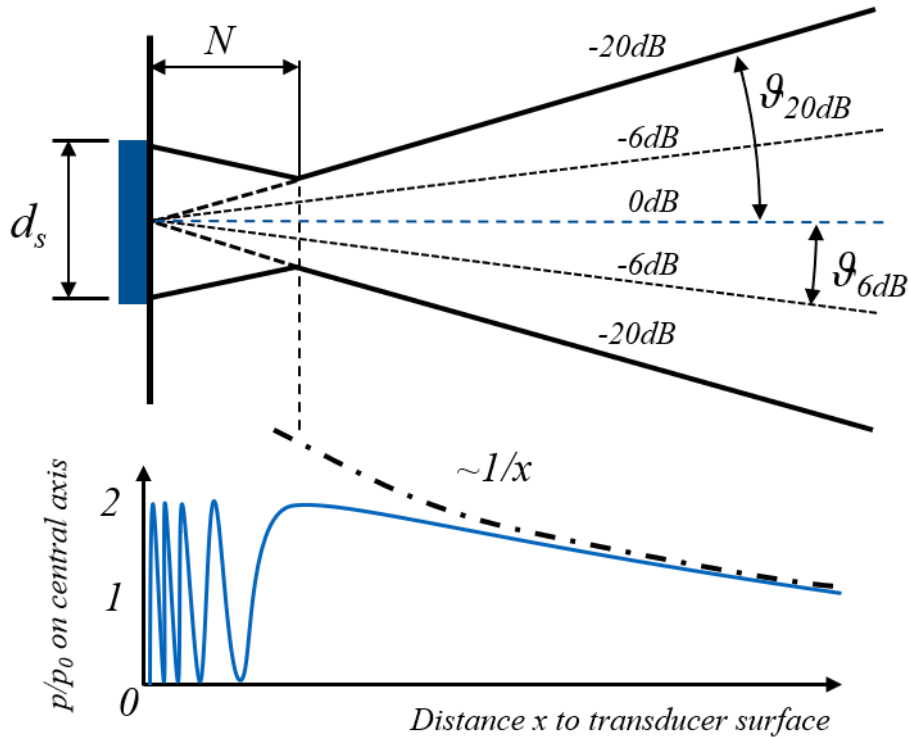


Figure 2.5: Schematic of the sound field emitted from a plane transducer and sound pressure distribution along the central axis. Graphic following [Krautkrämer & Krautkrämer 1990]

The far field begins after the near field distance and comprises an area where only constructive interferences occur. It is characterized by its opening angle ϑ , which is defined by the sound pressure level falling below a certain threshold compared to the central axis (-6 dB for a 50 % reduction or -20 dB for a reduction to 10 % for example). In the far field, only positive interferences exist. For this work, a -6 dB threshold will be used. The opening angle can be approximated by [Deutsch et al. 1997]:

$$\sin \vartheta_{-6\text{dB}} = 0.7 \frac{\lambda}{2r_s} \tag{2.14}$$

Where r_s is again the radius of the surface and λ the wavelength of the emitted sound.

Two closely related phenomena occurring in sound fields are grating lobes and side lobes. Side lobes can occur in sound fields of all kinds of transducers (planar, spherical) of sufficient diameter to wavelength ratio, for grating lobes the pitch of individual transducer elements has to be smaller than half of a wavelength [E. Konetzke et al. 2015]. The pitch is the distance between the centers of two adjacent transducer elements in a phased-array transducer, illustrated in Figure 3.7 (right) with horizontal lines. The grating lobes are caused by spatial aliasing and can deteriorate the steering and/or focusing behavior of the transducer.

Side lobes are present for all transducers with diameter larger than the wavelength they emit [Krautkrämer & Krautkrämer 1990]. They can therefore only be decreased by making the transducer smaller, which in turn limits output power. As output power is the main concern in ACU transducer design, the side lobes should be avoided as best as possible.

For a spherically shaped transducer, the focal length f_f (i.e. near field length) must be calculated using the geometric properties of the transducer [Kuttruff 1988]:

$$f_f = R_s - \frac{12 \cdot R_s}{(kh)^2 + 12} \quad (2.15)$$

Here, R_s is the spherical radius of the transducer, k is the wave number calculated according to $k = 2\pi/\lambda$ and h is the maximum physical distance between the chord connecting the edges of the transducer and the arc represented by the transducer surface. It is calculated with $h = R - \sqrt{R^2 - a^2}$, where a is the aperture radius.

The radius r_f from the central axis to where the intensity is halved (-6 dB) around the focal point can be similarly calculated by [Kuttruff 1988]:

$$r_f = 0.257 \frac{\lambda f_f}{a} \quad (2.16)$$

Where λ is the wavelength, f_f is the focal length and a is the aperture radius the geometric radius for spherical transducers.

2.2.5 Vibration Modes of Clamped Circular Plates

The displacement u of an oscillating ideal thin circular membrane with fixed circumference can be described with the following differential equation (in cylindrical coordinates r, θ, z):

$$\frac{\partial^2 u}{\partial t^2} = c^2 \left(\frac{\partial^2 u}{\partial r^2} + \frac{1}{r} \frac{\partial u}{\partial r} + \frac{1}{r^2} \frac{\partial^2 u}{\partial \theta^2} \right) \quad (2.17)$$

$$\text{for } 0 \leq r < a, 0 \leq \theta < 2\pi \text{ and } u = 0 \text{ for } r = a$$

Where a is the radius of the membrane. The general solution to this equation can be obtained with separation of variables and by employing the Bessel function. The resulting mode shapes for some selected configurations are depicted in Figure 2.6. Similar shapes can also be observed when performing a modal analysis with finite element methods on isotropic materials, e.g. steel [Tufoi et al. 2014].

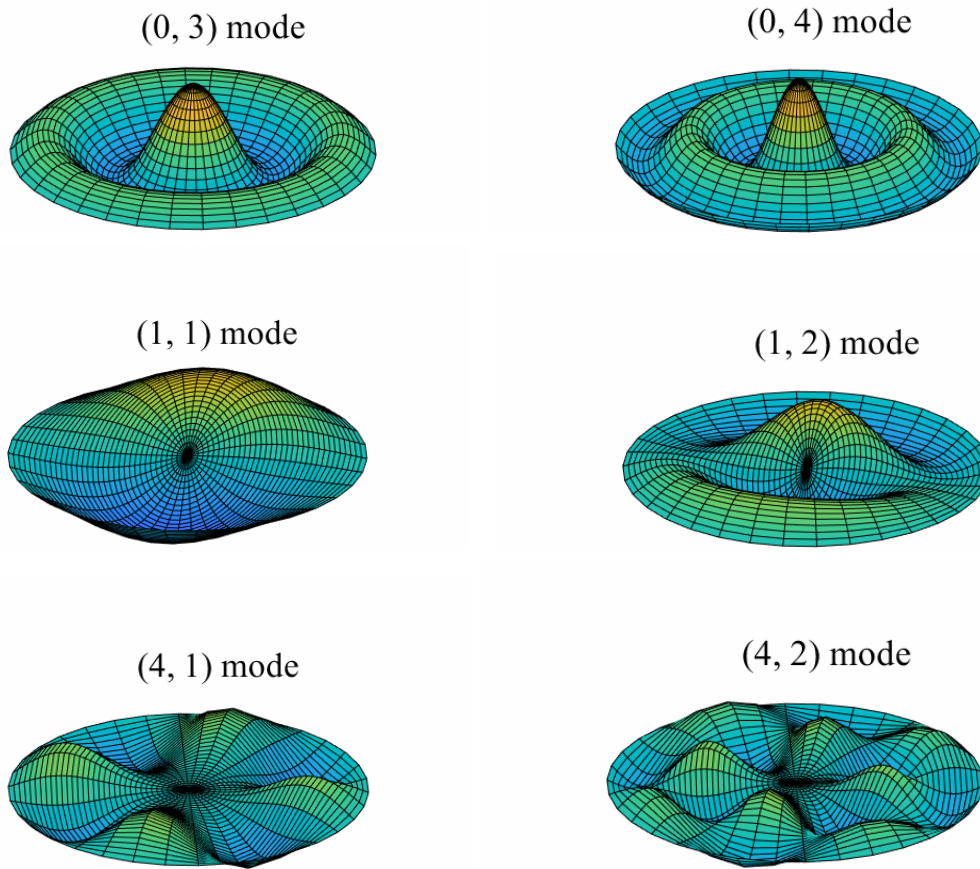


Figure 2.6: Selected vibration modes of an ideal circular membrane. The first index gives the number of nodal axes, the second the number of nodal rings (including the circumference). Recreated from [Alexandrov 2008]

Theoretical and experimental studies were also conducted regarding the vibration modes of circular piezo ceramic elements [Huang et al. 2004, Pohl et al. 2012]. The latter focused on lamb wave generation and thus analyzed the freely vibrating piezo and the one fixed on a surface. As such, the resulting mode shapes were quite different to the shapes presented above. Both works suggest that the out of plane and in plane vibrations of the piezo are decoupled only for a diameter-to-thickness ratio greater than 10. This is thought to be qualitatively true also for piezo composites, however no research regarding the vibration mechanics of circular piezo composite disks could be found.

According to experimental work [Pohl et al. 2010], the bonding of a piezo ceramic to another material influences its oscillation, as it decreases the maximum amplitude and shifts the resonance frequencies to higher values while decreasing resonance amplitude.

2.3 Optical Microphone

The general principles of an optical microphone are explained in the first half of this section. In the second half, the structure and properties of the microphone used in this work (*Xarion Eta 250 Ultra*) are presented.

The benefits of this device are that, compared to conventional ACU with piezoceramic transducers on sending and receiving sides, there is one less interface where transmission losses occur. The sound is measured directly in air, without moving mechanical components which inherently have a resonant frequency. This promises a broadband spectrum for measurement from 100 Hz to 1MHz [Xarion Laser Acoustics GmbH 2017] without significant frequency-dependent sensitivity. Another improvement is the reduced acoustic aperture resulting from the much smaller form factor of the optical microphone. This improves spatial scan resolution, as Gamper (2017) demonstrated.

2.3.1 Pressure Dependency of Refractive Index

For ideal gases, a simple derivation of the refractive index and its dependency on pressure and temperature can be made. It can be shown that the refractive index of a mixture of nonpolar gases can be calculated with the specific refractions of the constituents R_i and their densities ρ_i [Böttcher et al. 1973]:

$$\frac{n^2 - 1}{n^2 + 2} = \sum_i S_{R,i} \rho_i. \quad (2.18)$$

Extensive research has been carried out regarding the determination of the refractive index of air [Ciddor 1996, Edlén 1966, Owens 1967, Peck & Reeder 1972], increasing the accuracy of the formulae each time. Precise knowledge of the refractive index is essential when performing atmospheric measurements or accounting for changes in air quantities (humidity, CO₂ content) in laboratory experiments. The equations introduced by Ciddor (1996) were adopted as the basis for a new standard by the International Association of Geodesy and can be seen as definitive for the present. He provided values of the refractive index of dry air for a temperature of 20 °C, a CO₂ content of 450 ppm and a light source with $\lambda = 633$ nm. These values are given here in Table 2.2. For the given temperature and pressure range, the refractive index behaves linearly with respect to the pressure, as can be seen from the data.

Table 2.2: Phase refractivity of Dry Air with 450 ppm CO₂ ($\lambda = 633$ nm). Values by [Ciddor 1996].

Temperature (°C)	Pressure (kPa)	$10^8(n - 1)$	n
20	80	21458.0	1.000214580
20	100	26824.4	1.000268244
20	120	32191.6	1.000321916

The calculated slope is 0.268×10^{-8} . Thus, the refractive index can be approximated under laboratory conditions by

$$n = 2.68 \times 10^{-9} \text{ 1/Pa} \cdot p \tag{2.19}$$

Where p is the pressure between 80 kPa and 120 kPa, which are the limits of usual atmospheric pressure up to 1000 m above sea level.

It should be noted that the laser wavelength of the optical microphone is close to the one for which the refractive indices are calculated. The CO₂-content calculated with (450 ppm) however is presumably only half of that in a closed laboratory. Up until a CO₂-content of 1500 ppm, which corresponds to low air quality [Lahrz et al. 2008], the constant relating refractive index and pressure does not change with the given accuracy.

2.3.2 Structure and Functioning Principle

The general idea of the optical microphone is to measure the sound pressure in air with a laser beam. Since the optical path of light is significantly influenced by the refractive index of the medium it travels through and the refractive index of air changes with (sound) pressure, an optical microphone can measure sound waves without moving mechanical components.

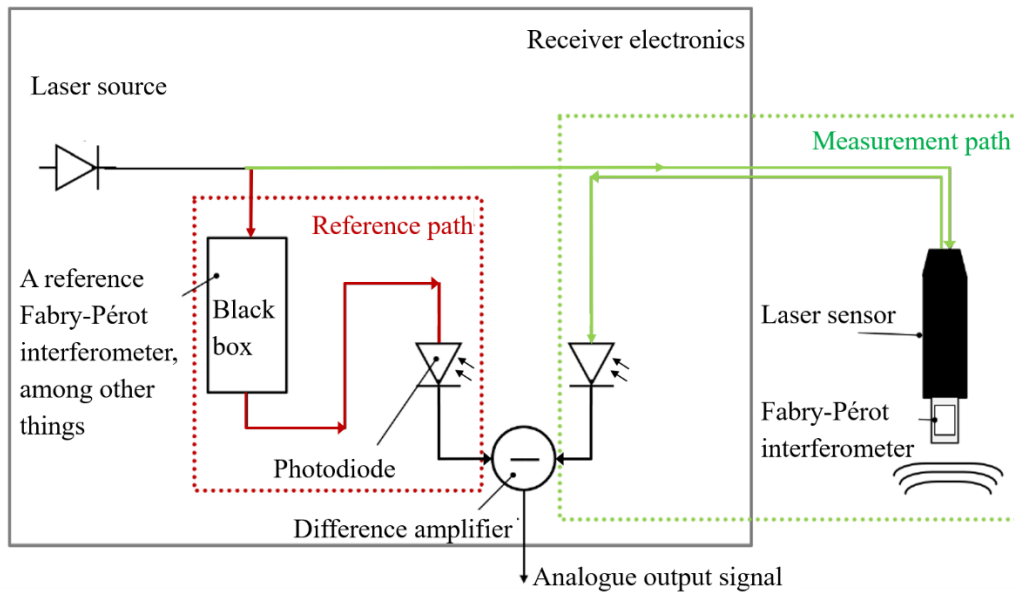


Figure 2.7: Internal structure of the optical microphone. Translated from [Guruschkin 2015].

In the following, the structure of the optical microphone will be presented. A laser beam emitted by a source (laser emitting diode, visible in Figure 2.7) is split into two parts, the reference and the measurement path. In the reference path (red color in the image), external influences like sound are kept out as good as possible. The laser beam travels through a fabry-pérot interferometer in which it is reflected back and forth many times by mirrors on both ends of a chamber. The mirror on one side has a slightly higher transmissivity, allowing a fraction of the laser to exit. This light is then directed to a photodiode, which converts the

light intensity to an electric voltage through the inner photoelectric effect. In the measurement path (green color), the fabry-pérot interferometer is opened to the environment to enable the propagating of sound waves. In denser air, corresponding to a higher SPL, light has a higher speed than in less dense air corresponding to a lower SPL. Through interference effects in the etalon the intensity of the laser beam is changed due to the different optical path length. This change of intensity is then detected by a photodiode. The electrical signals of both paths are then subtracted from each other, which filters any intensity changes of the laser source.

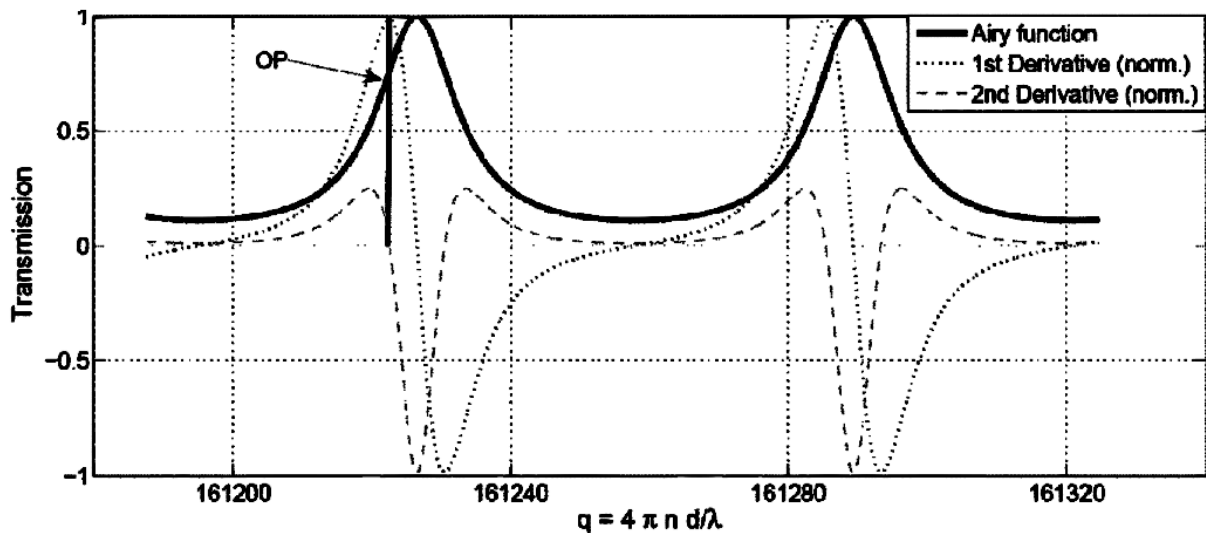


Figure 2.8: Airy-function for the etalon of the optical microphone. [US 2015/0139451 A1 2015]

The transmission rate of an etalon can be determined with the airy function of the parameter q plotted in Figure 2.8. This parameter is proportional to the refractive index n and the distance d between the two mirrors of the etalon. It is inversely proportional to the wavelength λ of the light, which is used to precisely determine the location of the operating point. To obtain a linear relationship between q and the transmission rate the OP is chosen to lay on the turning point of the rising edge, where the second derivative is zero.

2.3.3 Internal Signal Processing and SNR

The electrical signals, one from the reference and one from the measurement path are subtracted from each other. With this step, signal noise stemming from the laser source can be eliminated. The signal is then processed in such a way that it resembles the current pressure inside the etalon and amplified by a set value (- 12 dB, 0 dB or + 20 dB in the case of this work). A fixed-frequency high pass filter is then applied with a cutoff frequency of 100 Hz. In other models of the optical microphone settings ranging from 10 Hz to 1 kHz of the high pass filter are enabled. Since the refractive index of air is not only changing due to “short” events such as sound waves but also “long” events like changing temperature, humidity and static pressure changes (for example due to weather or current height above sea level), the operating point depicted in Figure 2.8 is determined each time the optical microphone is powered up.

This results in a startup time (until measurements can take place) of about five minutes. The operating point is then constantly monitored and adjusted, which enables the microphone to quickly adapt to changing conditions. This can however also lead to overshoot, causing a short disruption of the measurement [Gamper 2017].

The ETA 450 Ultra has a 12 dB higher signal-to-noise ratio (SNR) than the ETA 250 Ultra used in this work for the relevant frequencies above 200 kHz [Citation]. Consequently, the manufacturer states a sensitivity of 115,5 mV/Pa for the 450 Ultra and 5 mV/Pa for the 250 Ultra at 0 dB amplification. However, in the datasheet found online for the ETA 250 Ultra they state a sensitivity of 10 mV/Pa making this value unreliable for absolute predictions of sound pressure. To solve this problem, a calibration with known sources would be necessary.

2.4 Laser Doppler Vibrometer

The Laser Doppler Vibrometer (LDV) is, in its functioning principles, like the optical microphone. Both devices rely on interferometers to detect certain changes in the optical path of a laser. What is different in most (but not all) cases is the physical mechanism that causes the change of the optical path. While the optical microphone can only detect pressure changes in air due to the closed structure of the etalon, the LDV is best applied to measure vibrating surfaces. It relies on the reflection of a laser beam off a surface back to the interferometer, where the distance to the object can range from 20 cm to a few hundred meters. The limiting factor is the surface reflectivity which must be sufficiently large to allow for acceptable signal levels. For this work, the OFV-5000 model manufactured by *Polytec* was used. In the first part of this section, the interferometer is introduced with respect to its applications in this work. In the second part, the three decoders used to extract electrical signals from the interferometers are explained in detail.

2.4.1 Heterodyne Interferometer

The LDV can detect two main physical quantities through its Heterodyne Interferometer: Velocity and displacement of an object/surface. If the laser beam illuminates a surface moving with a certain velocity parallel to the beam, the light will be reflected with a frequency shift according to the doppler effect. It will also have a phase shift depending on where in the path the light got reflected. Therefore, the velocity information can be extracted from the frequency shift while the phase shift carries displacement information. The general structure of the interferometer is depicted in Figure 2.9. The light from the laser is first split at a beam splitter (BS 1), halving the intensities of each partial beam. The so-called measurement beam is directed through another beam splitter (BS 2) and a focusing lens onto the measurement object. It is then reflected to BS 2 and from there to the last beam splitter (BS 3). The reference beam is directed from BS 1 through a Bragg cell, which applies a frequency shift of typically

40 MHz (the laser light has a frequency of 4.74×10^8 MHz). Both partial beams are joined at BS 3 and detected on a photodiode measuring the periodic amplitude oscillations resulting from the frequency shift between them. The Bragg cell is introduced in the setup to allow for signed voltage output. If there was no constant frequency shift the direction of movement could not be detected.

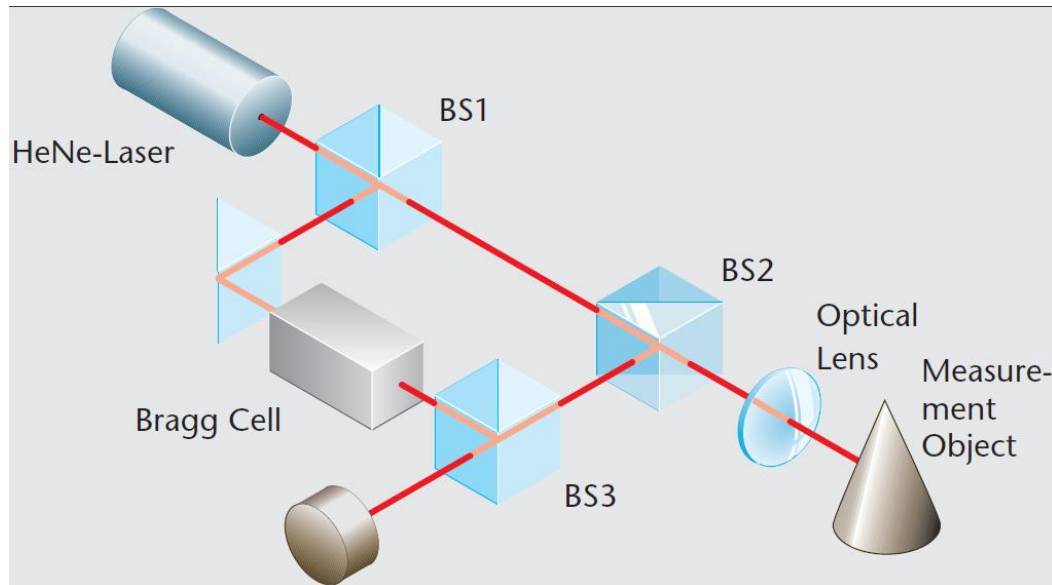


Figure 2.9: Functioning principle of the laser-doppler vibrometer. Image courtesy of [Polytec GmbH 2006].

One main limitation of the achievable signal quality is so called “speckle noise”. It can occur when the measured surface moves slightly in relation to the laser beam. It is caused by the interference of the light scattered from many different points of a rough surface [Martarelli & Ewins 2006]. To reduce the influence of the speckles it is possible to apply reflective foil or paint, thus changing speckle size, or to adapt the optics of the LDV [Rembe & Dräbenstedt 2015]. There are also speckle noise detecting algorithms which can be applied after the measurement has been completed [Cristalli et al. 2006].

In the application of the present work, the transducer surface was constantly moving in relation to the LDV device (perpendicular to the laser beam), illuminating different speckles each passing moment. This caused a random distribution of “bad pixels” which persisted even though the data was averaged over five measurements taken at slightly different positions and hence, different “speckle configurations”.

2.4.2 Decoders for Velocity and Displacement

In the present model, one velocity and two displacement decoders are built in. During the measurements it got clear that one of the displacement decoders could not be used to obtain reliable data, due to the prefixed range setting. Each decoder will be explained in the following.

VD-09

This digital broadband velocity decoder can be used for frequencies up to 2.5 MHz. There are eight measuring sensitivities supporting from 5 mm/s/V up to 1 m/s/V. A maximum velocity of 10 m/s is measurable. Each measuring range also has a corresponding maximum frequency, ranging in total from 0 Hz (DC-mode) to 2.5 MHz. In the measurements performed, first the range of 20 mm/s/V was used. However, data clipping occurred in this setting. Therefore, for subsequent measurements of the transducer surface, 100 mm/s/V was used.

DD-900

The DD-900 decoder is again a broadband digital decoder, but it outputs a signal corresponding to the displacement. The phase shift of the doppler signal is processed quasi-continuously, attaining a displacement resolution of under 1 pm. It has a maximum output voltage of ± 10 V. This decoder was set to a range of 50 nm/V in all measurements. The rounded resolution corresponding to a 0.3 mV change at the output was therefore 15 nm. It is important to note that the use of this decoder requires a velocity decoder to be built-in. As such, the specifications for frequency behavior etc. correspond to the set velocity range. R2Z mode was used as clipping behavior since the vibrations of the CNC table (see 3.1.2) were much larger than the available voltage range. In this mode, the output is set to zero when it reaches the maximum value, resulting in a sawtooth voltage for a constantly moving surface.

DD-300

This displacement decoder was designed for capturing high-frequency oscillations and pulses in the frequency band of 30 kHz up to 24 MHz. It has a built-in tracking filter. According to the data sheet, its maximum measurable amplitude is 75 nm, making it unsuitable for the measurement of the transducer surface vibrations as permanent data clipping occurs.

3 Experimental Setup

Additional systems used to perform the measurements are covered. In the first part of this chapter, the physical components of the testing system are presented, explaining their role for the measurement and their specific properties. Then, the digital signal processing methods are explained with regards to their potential to distort or to clarify measured data. Finally, a complete overview over the measurement chain is given and the errors of each component are discussed.

3.1 Measurement Hardware

An overview of the arrangement of components is given in Figure 3.1 with the signal path starting from the laptop. The structure of this chapter follows this signal path. As the optical microphone and the laser-doppler vibrometer were already covered in the previous section, they will not be considered again here. The signal path will be referenced again in section 3.4.

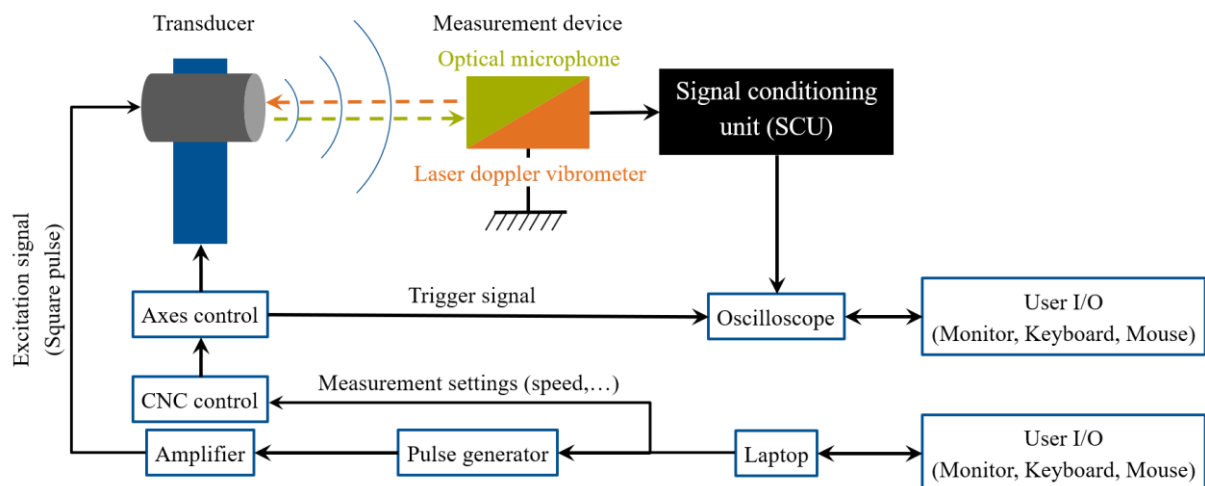


Figure 3.1: Schematic of the components in the measurement setup and their connection. The arrows of the dashed lines indicate the measurement point.

3.1.2 3-Axis CNC Machine and Coordinate System

The 3-Axis CNC Machine consists of the parts “CNC control” and “Axes control” in Figure 3.1. It is used to perform automated tests and was assembled by López Baos (2018). In these automated tests, a predefined area is scanned systematically and trigger signals are sent to the oscilloscope at defined intervals. It has a workspace area of $530 \times 500 \times 190$ mm (X-Y-Z axes) and a minimum scanning increment (in both scanning directions) of 0.05 mm. Its positioning reproducibility is accurate to ± 0.02 mm [isel Germany AG n.d.]. Figure 3.2 shows the *ISEL* CNC machine as well as its internal coordinate system. It was decided to adhere to these coordinate axes for the data visualization. During some of the preliminary tests it was observed that when considering the absolute power of the measured signal of the optical microphone with applied band pass filter, even rows have a different power compared to uneven

ones. Most likely, the stepper-motors of the CNC machine emit different frequencies depending on their direction of rotation which results in a change of the signal power. However, this has not finally been verified as the influence is unobservable when considering signals without a filter, which was the focus of this work.

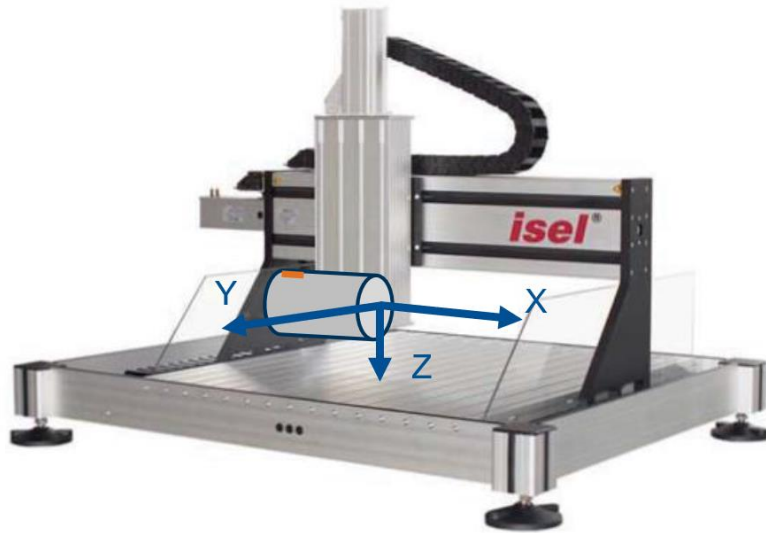


Figure 3.2: Right: Granty Table System – FB2 by ISEL with visualization of the transducer (not to scale) and coordinate axes (blue) [isel Germany AG n.d.]. The applied marker for transducer orientation is indicated in orange.

For the presentation of the measurement data, it was reasonable to define the coordinate system's origin as the middle-point of the transducer surface, as indicated in Figure 3.2. This results in a moving origin of the coordinate system, as the transducer was mounted onto the moving arm of the CNC machine in all measurements. Since the alignment of the transducer position relative to the measurement device had to be carried out manually each time the configuration was changed, the repositioning accuracy is expected to be as low as ± 2 mm. The origin of the coordinate system therefore might deviate from the middle point of the transducer surface in the visualization. However, as the measurements were obtained by scanning over a larger region, this positioning error only influences the physical position of the transducer relative to the axes in the figures, not the measured quantities themselves.

3.1.3 Signal Generator and Amplifier

The signal generator and amplifier produced by *SONOTEC* has four independent outputs with a maximum voltage of 800 V. In this work only square pulses were generated and used for excitation of the transducers, although in principle arbitrary signals are possible. This system is connected to the CNC table via a serial real-time connection and synchronizes with high accuracy the signal to the transducer and the trigger output in relation to the CNC table movement. This synchronization enables the time-evolving visualization of the transducer

sound fields and surfaces, as time shifts in the order of microseconds can already distort the image. This can be seen in the time-evolving sound fields in section 4.1.1.

Since the investigated transducers have a fixed maximum peak-to-peak Voltage (V_{pp}), the amplifier output for a given voltage was observed by directly connecting it to an oscilloscope. Not to damage the oscilloscope, the set voltage was limited to 40 V. In this low-voltage regime the behavior depicted in Figure 3.3 could be observed. Voltage spikes are present in the both the rising and falling edges of the signal, effectively tripling the peak-to-peak voltage which would be applied to the transducer. The spikes were still present when a transducer was integrated to the line of measurement, so they are not a result of zero-loading. It is therefore likely that the voltage spikes occur internally in the amplifier. The investigations could not be carried out at high voltages since the voltage dividers we used did not act linear in this case and thus did not warrant reliable results. In the observable regime the voltage spikes scaled linearly with the set amplifier voltage. As a precaution, the transducers were excited with at most one third of the specified peak-to-peak voltage.

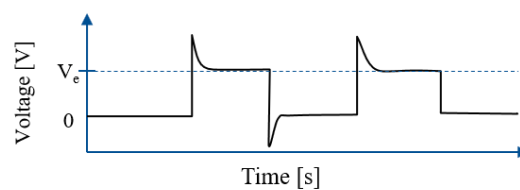


Figure 3.3: Voltage Peaks from signal Amplifier. Top: schematic drawing with high damping (but still not ideal), V_e is the set voltage. Bottom: actual oscilloscope output with connected transducer.

3.1.4 Utilized Transducers

The five transducers utilized in this work are shown in Figure 3.4. The transducers' specifications are presented in Table 3.1. Some values were not available due to no specification or testing protocol being provided by the manufacturer. Before measurements were made, markers were applied to the *SONOTEC* transducers to be able to position them in the same orientation each time the measurement configuration was set up. This marker was also used to rotate

the transducers in a specified manner (see 4.2.2). The different transducer types will be discussed in this section.



Figure 3.4: From left to right: *SONOTEC CF400 3E & CF400 (with markers)*, *The Ultran Group ULT200*, *Ingenieurbüro Dr. Hillger AT200 & AT75*

Table 3.1: Selected specifications of utilized transducers [Ing. Büro Dr. Hillger 2018, SONOTEC Ultraschallsensorik Halle GmbH 2018, The Ultran Group 2018]

Mnemonic	CF400 3E	CF400	ULT200	AT200	AT75
Transducer name	SONOSCAN CF 400 3E	SONOSCAN CF 400	NCG200-D13- P38	AirTech 200	AirTech 75
Frequency	400 kHz	400 kHz	200 kHz	200 kHz	75 kHz
Bandwidth	-	-	-	21 kHz	9 kHz
Active \varnothing	20 mm	20 mm	12.5 mm	11.1 mm	30.0 mm
Near-field length	50 mm/2	50 mm (focal length)	38 mm (focal length)	18 mm	50 mm
Sound beam \varnothing	-	4 mm	-	3 mm	8 mm
Wavelength in air	0.86 mm	0.86 mm	1.7 mm	1.7 mm	4.5 mm

Planar Transducers

The two transducers made by *Ingenieurbüro Dr. Hillger* (AT200 and AT75) are planar transducers without damping material i.e. they are air-backed [Gamper 2017, Stößel 2004]. The

planar surface still shows some focusing behavior through interference effects in the near field (2.2.4), although less pronounced than with other means of focusing. Since the scope of this work are “actively” focused transducers the planar ones were not intensively studied, but their results will be presented alongside the other transducers.

Physically Focused Transducers

One transducer of *SONOTEC* (CF400) and the one by *The Ultran Group* (ULT200) have a spherically shaped surface, resulting in a smaller sound beam diameter and near field length compared to the planar transducers. This is beneficial in two ways: The maximum sound power increases since the energy is focused on a smaller area and the transducer can be mounted in a closer position to the specimen under test, giving the setup more practical use and allowing higher frequencies to be used due to decreased attenuation.

As discussed in 2.2.4, the radius of curvature of the surface is important to determine the focal length, but they do not coincide. Since the radius of curvature is not given by the manufacturers in the specifications, measurements were performed with a confocal laser scanning microscope (CLSM), which in addition to the geometry also gave insights to the microscopic structure of the surface. The radius of curvature was determined by minimizing the sum of squared radial deviations over the acquired data, assuming the transducer surface should be perfectly spherical. The results for both transducers are shown in Figure 3.5. An abrupt vertical step is visible at $y = 1$ mm in the profile line of the CF400, evoked from the protruding steel bracket. It was not possible to perform a scan over the whole active diameter of the ULT200, as it has a similar but much higher steel bracket and the microscope has a small range in x-Axis direction. Thus, a step like in the profile line of the CF400 is not observable in the ULT200’s profile line.

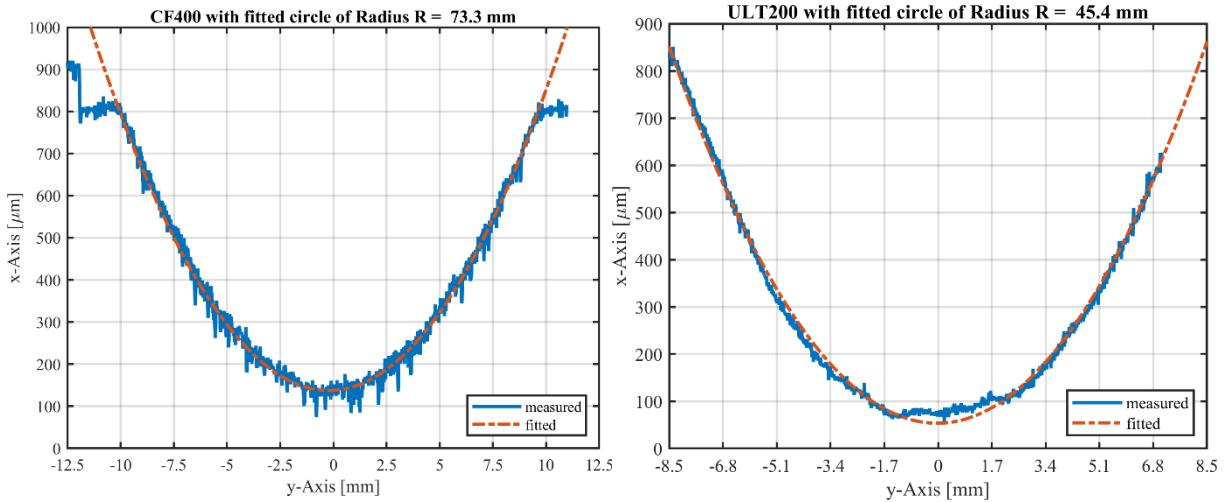


Figure 3.5: Profile lines of the two physically focused transducers measured with CLSM (5x magnification) and result of the fitting algorithm. Left: CF400 with radius $R=73.3$ mm, right: ULT200 with radius $R=45.4$ mm

The “noise” present in the profile lines, much more pronounced for the CF400, is in fact due to microstructures in the visible matching layer, as is clarified by the 3D-Surface view in Figure 3.6. It was measured with a 20x magnification compared to the 5x magnification for the profile lines. Additional images measured with the CLSM are depicted in Appendix A.

In the surface view, the depth of the vesicles is up to 80-90 μm , which coincides with the amplitude of the fluctuations in the profile line. This is a large value compared to the pores in other materials used as matching layer for 400 kHz ACU transducers, which usually measure only a few μm [Alvarez-Arenas 2004, Gronauer & Fricke 1986]. It also means that large attenuation is to be expected due to the vesicles, as they are about $1/10^{\text{th}}$ the wavelength of a 400 kHz wave in this material, assuming a speed of sound in the order of 500 m/s. There appear to be small solid spots in the middle of some vesicles (yellow color in the figure). It is not clear whether these are real or caused due to a reflection of light at the round outer surface.

A porous material as coupling layer is best suited for air-coupled ultrasound due to impedance matching (2.1.3). These materials have thusly a low sound velocity of only a few hundred m/s,

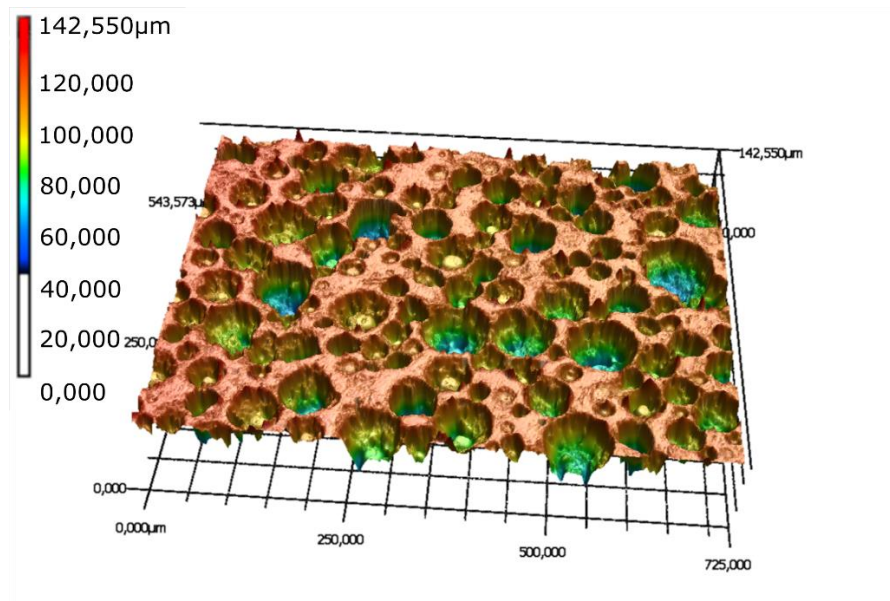


Figure 3.6: 3D surface of transducer CF400 measured with CLSM (20x magnification). The height of the vesicles is about 80-90 μm .

SONOTEC states in a publication that their spherical transducer cannot have a shorter focal distance due to “material limits” [Mück 2018]. This suggests that the ULT200 is made from a different material, since it has a much lower spherical radius and thus also a lower focal distance. According to the manufacturer, the material used in the transducer is a proprietary gas matrix piezoelectric composite [The Ultran Group 2018]. A more in-depth discussion of the transducer’s properties is given in 4.1.2. It is likely that the value for the focal length of 38 mm given by the manufacturer actually corresponds to the spherical radius of the ULT200, as explained in section 4.1.2.

Electronically Focused Transducer

The electronically focused or phased-array transducer has three separate inputs corresponding to three independent electrodes on its surface (Figure 3.7). The electrodes have the same surface area so that the capacitance and the emitted sound energy is equal for all of them.

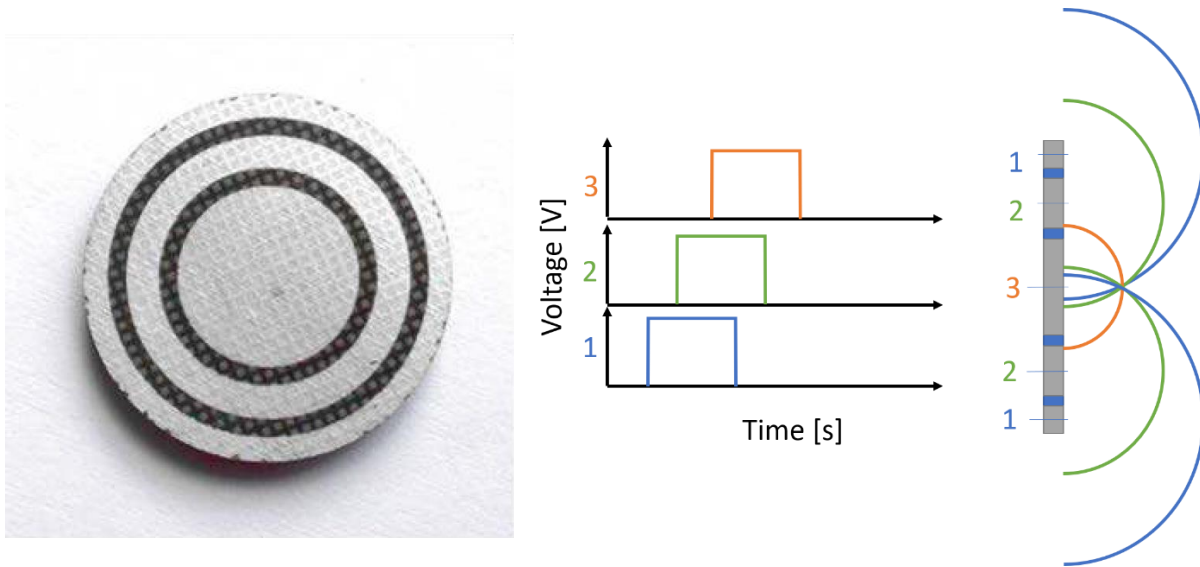


Figure 3.7: Left: Piezo composite transducer SONOSCAN CF400 3E (image by [Mück & Scheunemann 2018], licensed under CC 4.0) with three separate silver electrodes. Right: Schematic of phase shift and focusing effect.

As is visible from Figure 3.7 (left), the electronically focused transducer is made from piezo-composite material (see 2.2.2) onto which the electrodes are applied. In particular, there are no kerfs or other materials between the electrodes. This may promote crosstalk between elements [Lenz et al. 2013], deteriorating in theory the achievable focus effect. With the given transducer diameter of 20 mm the other dimensions of the transducer could be determined from the image. The edge length of the small piezo elements was determined to be 0.3 mm, their pitch (middle-to-middle distance) to 0.5 mm. Together with the specified frequency of 400 kHz it can then be determined that the minimum speed of the shear wave is 400 m/s, assuming that the condition for uniform oscillation presented in 2.2.2 is met.

The right side of Figure 3.7 shows the principle of the focusing effect through a phase shifted excitation. Depicted is a cross-section of the transducer where the electrode-covered areas are gray, and the electrode-free areas are colored blue. The center points of the circles are the intersection between the right surface of the transducer and the horizontal line marking the middle of the electrode-covered element. From the graphic one can see that the outermost ring must receive its excitation signal first, followed by the middle and the inner ring, which is also the typical configuration for a conventional focused phased-array transducer.

Due to the large pitch between the individual electrodes, which is about 10 times larger than the emitted wavelength, it is expected that prominent grating lobes occur when using the electrical focusing effect of the transducer, which diminish the achievable focusing behavior.

3.1.5 Oscilloscopes

Oscilloscopes record analog signals and either display them directly to the user or convert them to a digital signal for data processing and storage. Two oscilloscopes were used during this work. First, measurements were performed with the *TiePie HS5* since it can directly output its measured data to an easily processable .mat file. It soon became apparent however that the storage speed of the TiePie was not sufficient for the high data rates encountered during a scanning measurement. This is most likely due to the limitations of the USB-connection to the computer which has a certain bandwidth and latency and the oscilloscope does not have an internal storage for buffering. The minimum time to store a block of 1000 samples achieved by López-Baos (2018) was 40 ms with the TiePie compared to 2.5 ms with the second oscilloscope called TranAX. Smaller storage times are preferable since they enable a higher measurement frequency without data loss. The measurement frequency is directly influenced by the movement speed of the CNC table, so the scans can be performed much quicker with lower storage times. This is the reason why the TranAX oscilloscope was used for all further measurements, as the time effort for one measurement was lower even though data conversion was much more time-consuming. The relevant specifications and settings of the TranAX oscilloscope will be explained further.

An important factor in how the oscilloscope records data is the trigger setting. As the amplifier in the setup (see 3.1.3) provides a square pulse trigger signal which is highly synchronized to the transducer excitation output, this trigger signal acted as one input of the oscilloscopes. The other one being the input of the measurement device. Since the trigger signal has a finite width, the oscilloscope was set to record data starting from the rising edge, ensuring all signals coming from the transducer excitation were recorded. In ECR (event-controlled recording) mode, the number of blocks saved to one file can be freely adjusted. For scanning purposes, this number was always set such that the file transition overlapped with a line change of the CNC table to give enough time for accessing the hard-disk. For example, if one measurement line consisted of 201 measurement points (20 mm line length at 0.1 mm acquiring distance), the block number could be set to 201, 402, 603... files. It is advisable although not necessary to set the number of blocks such that the last point of measurement corresponds to the last block in a file.

The voltage range of the oscilloscope varied depending on the experimental setup. All surface scans were recorded with a range of ± 25 V, although due to the maximum output voltage of the encoders (2.4.2) only a range of ± 15 V would have been necessary. The discretization introduced by this mismatch error is considered negligible however, since the data was stored with a precision of 16 bit. For the sound field measurements, different ranges from ± 2.5 V to ± 10 V were chosen according to the signal level at near field length.

For sound field measurements, the recording frequency was set to 2 MHz, the same frequency López-Baos (2018) used. It fulfills the Nyquist-criterion for 400 kHz but does not generate as much data as higher frequencies would, which was especially important for the preliminary measurements done with the TiePie oscilloscope. The transducer surface scans were recorded with a sampling frequency of 20 MHz as it was not known whether higher frequencies occur in this measurement and the amount of data was less of a concern. Later, the use of such a high sampling frequency allowed for averaging with a precise window to subtract the static displacement of the transducer surface from the dynamic one.

3.2 Scanning Measurement Configurations

Sound field measurement and transducer surface scan differ mainly in their scanning directions and measurement device. The measuring process, however, is the same and takes place as follows: The CNC table continuously moves the transducer in a meander-like shape in relation to the measurement device. During this movement, the transducer is excited with a predetermined pulse in periodic intervals, and the recording of the measurement is started together with the excitation pulse.

The transducer is considered stationary for the duration of the measurement recording, even though the table never actually stops moving. This is justified by the relatively slow speed of the CNC table, meaning that during the typical excitation signal length of 12.5 μ s it moves only 1 μ m.

It is important to emphasize that for each measuring point where the transducer was excited, the complete response signal was recorded. All these point measurements recorded in an area scan were then arranged to yield C-Scan images as explained in 3.3.1. In both measurement types, we set the individual recordings to be 0.2 mm apart from each other i.e. the pixel size in the C-Scan images is 0.2×0.2 mm. The transducer received an excitation signal of five square pulses for most of the measurements; the only other excitation signal consisted of one square pulse. The amplifier voltage was mostly 100 V, as this voltage lays under one third of the specified maximum peak-to-peak voltage of all tested transducers.

For the sound field, we chose a total measurement size of 100 x 40 mm, as the distance between transducer and material surface will be hardly any larger than 100 mm in real applications (except for the AT75 transducer). Also, the chosen dimensions coincided with the sound fields published by the manufacturer [Mück & Scheunemann 2018, Steinhausen et al. 2016a], facilitating a direct comparison. The minimum distance in x-axis direction between transducer and optical microphone was configured to 5 mm; the lowest possible distance between the two could be 3 mm with the current mounting mechanism. A summary of the settings used for both measurement types can be obtained from Table 3.2. A step-by-step instruction of performing the measurements can be found in Appendix B.

Table 3.2: Settings for sound field measurement and surface scan. Some settings were maintained from the work of López Baos (2018)

Setting	Sound field (optical microphone)	Surface scan (LDV)
Measurement size	100 × 40 mm	23 × 23 mm
Measurement resolution	0.2 mm	0.2 mm
Measurement speed	80 mm/s	2 mm/s
Averaging number	1	5
Voltage	100 V or 10 V	100 V or 10 V
Number of pulses	5 or 1	5 or 1
Measurement device specific setting	0 dB or -12 dB amplification	100 mm/s/V velocity, 50 nm/V displacement
Sample frequency	2 MHz	20 MHz
Number of samples	1000 or 2000	5050
Min. distance to transducer	5 mm	~23 mm (constant)

As visible in Figure 3.8 and Figure 3.9, the measurement device remained stationary for the experiments, while the transducer was mounted to the moving CNC table. This prohibited the table movement vibrations from being recorded and thus improved the SNR. The optical microphone recorded the sound fields, as it was better suited for this application than the LDV due to its small spatial aperture (i.e. integration distance), visible in Figure 3.10. By using the optical microphone we did not require tomographic methods to reconstruct the sound fields [Jenderka et al. 2015] as every measurement point is independent from the others, which is another advantage over the vibrometer. However, as will be discussed in section 4.1.1, echoes may occur due to the presence of the microphone in the sound field. The LDV is well-suited to measure the transducer's oscillation behavior. No reflective tape was necessary since the surface of the measured transducers is white and therefore sufficiently good signal quality could be achieved.

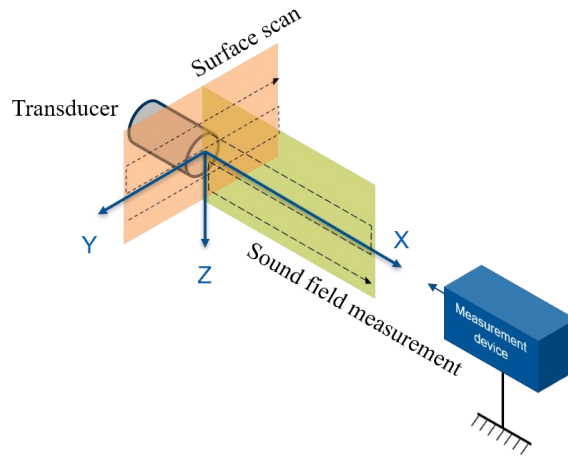


Figure 3.8: Spatial relation of transducer, measurement device (optical microphone or laser-doppler vibrometer) and scanning directions with coordinate system.



Figure 3.9: Photo of the arrangement for measurements with the laser-doppler vibrometer.

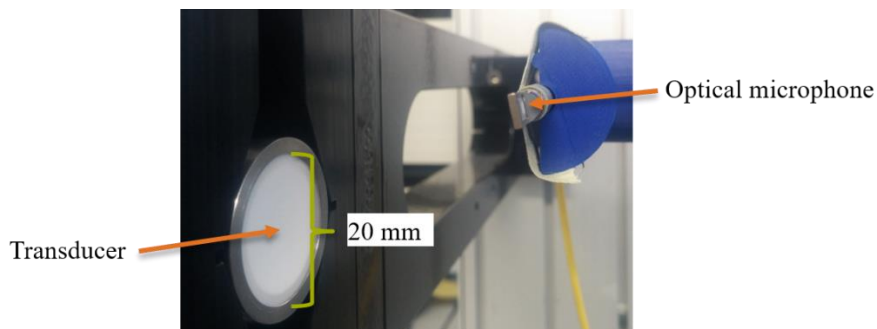


Figure 3.10: Photo of the optical microphone (with large deviation from vertical alignment) in front of the transducer. The transducer is mounted to the moving arm of the CNC table. The yellow fiber optic cable is visible in the background.

As mentioned above, the LDV can measure sound fields as well, although the experimental setup would require additional parts. Firstly, a rigid reflective surface would be need-

ed, preferably completely decoupled from the CNC table and the transducer, as any movements of this surface would cause errors in the measurements. To obtain absolute values of the sound field in a plane, a device rotating the transducer and appropriate post-processing methods would be needed. As neither of these two parts were directly accessible at the start of this work, the sound fields were recorded with the optical microphone. However, with this method the volumetric sound field is measurable in one experiment in contrast to the measurement with the optical microphone, where only one plane is evaluated. It might be interesting to perform these measurements and compare them with the results presented here.

As an alternative to performing the surface scans, a manual acquisition of the oscillation movement data was evaluated, and some measurements were performed this way. Speckle noise can be eliminated this way, as the position of the transducer can be slightly adjusted if speckle noise occurs. Another advantage is that a higher averaging number is possible this way, as the oscilloscope has a functionality of only saving the averaged data in manual mode. As this function could not be implemented in the time frame of this work for the automated ECR mode, a lower averaging number had to be used for the surface scan. As the scanning method gave good results with the averaging and moving median filter, the manual data acquisition was not pursued, as the resolution in the automatic scan was much better, especially for a two-dimensional manual scan.

Effect of the Sound Field on the Vibrometer Measurement

As can be derived from Figure 3.8, the laser beam of the vibrometer travels through the sound field in the air before being reflected on the surface. It is therefore of interest to compare the change in optical path caused by the sound waves to the amplitude of the transducer movement. This can influence the displacement measured by the laser doppler vibrometer but not the velocity as the frequency of the light is constant through different media. Since the refractive index can be approximated as linear with respect to pressure (see 2.3.1), the optical path difference (OPD) can be calculated with the following equation:

$$OPD = \int_0^d \Delta n(s) ds \quad \text{with } \Delta n = \Delta p \cdot 2.68 \times 10^{-9} \text{ 1/Pa} \quad (3.1)$$

Here, d is the physical distance of the light beam traveling through a medium with a difference of refractive index Δn with respect to the surrounding medium. It should be noted that in the case of the LDV, the laser beam travels the same distance twice since it is reflected at the transducer surface and any air movement is negligible compared to the speed of light. The constant relating the pressure difference from ambient air Δp to the difference in refractive index is also given in the equation.

To obtain meaningful estimations for the quantities needed, the following is considered: Before the transducer surface starts moving, the air in front of it is at ambient and uni-

form conditions. If the first movement of the transducer is forward (this depends on the excitation voltage), the air directly in front of the transducer is compressed, causing an optical path difference due to the higher pressure according to equation (3.1). When the transducer then returns to its original position, the compressed air has a thickness of half a wavelength. The transducer then starts its cycle in the reverse direction, expanding the air in front of it and thus reducing the optical path difference due to the lower than ambient pressure. An equivalent consideration is possible if the first movement of the transducer surface is in backwards direction, and all other oscillations afterwards. The optical path differences of complete waves equate to zero in the integral. This consequently leads to the estimation of d with the wavelength $\lambda = 0.86$ mm of the sound waves from the 400 kHz transducers that were measured with the vibrometer.

The sound field measurement of the CF400 transducer was considered for the estimation of the difference in ambient pressure. A maximum voltage of 7 V was recorded by the optical microphone at a distance of 50 mm, resulting in a sound pressure of about 1 kPa according to the conversion constant given by the manufacturer [Xarion Laser Acoustics GmbH 2017]. This can only serve as a rough estimate, as the conversion constant given in the data sheet delivered with the optical microphone is only half the value of the downloadable one and the microphone also has not been calibrated. With these values, one calculates the maximum optical path difference of the laser beam to 2 – 3 nm, which corresponds to about 1 % of the oscillation amplitude of the transducer (see 4.2.1). This error shifts the positive and negative parts of the oscillation relative to each other and thus is not affected by the applied filtering method.

3.3 Post-Processing of Measured Data

In this section, first the various methods for data visualization used in ultrasound imaging and this work are laid out. Then, the use of filters in the data processing is discussed. Finally, a short evaluation of the optimizations done for improving the data conversion process is given.

3.3.1 Data Visualization Methods

There are a multitude of visualization methods in ultrasound testing, depending on what kinds of data one wants to display. These conventional methods were extended during this work using moving images.

A-Scan

To visualize a signal at a single point in space, the A-Scan (referring to the signal amplitude) is used. Here, the electrical voltage from a receiver is plotted against the time it takes the signal to be recorded. The A-Scan is the basis for line- and spatial representations. There

are different forms of presentation of the A-Scan. In its “Amplitude” form, the Signal is rectified before plotting, which results in the loss of phase information. The HF-image (high-frequency) represents the actual voltage fluctuations without any modifications. Conclusions about the amount of damping in the transducer can be obtained from this representation.

B-Scan

Adding a line of consecutive A-Scans together, one can obtain a B-Scan by encoding each signal amplitude with a color or brightness. This results in a 2-dimensional color-coded image visible in Figure 3.11. In conventional pulse-echo configurations (with coupling medium), the depth of a flaw can be determined with this method of presentation. It is important for each A-Scan to be recorded at the correct distance from the last one and hence, electronic precision manipulators are frequently used. There are other ways of generating a B-Scan from a line of A-Scans, for example if not the amplitude is encoded, but the frequency power after a Fourier-transformation. In this case, the axes of the image are space and frequency instead of space and time.

The obtainable information of a B-Scan is strongly influenced by the color-coding. Small differences in data can be highlighted through abrupt changes in the colormap, which is used to determine the color of a pixel from its signal amplitude. In this work, only linear colormaps were used for B-Scan and C-Scan images. However, the range of the colormap was sometimes adjusted manually to increase visibility. This will be mentioned in the description of the figure.

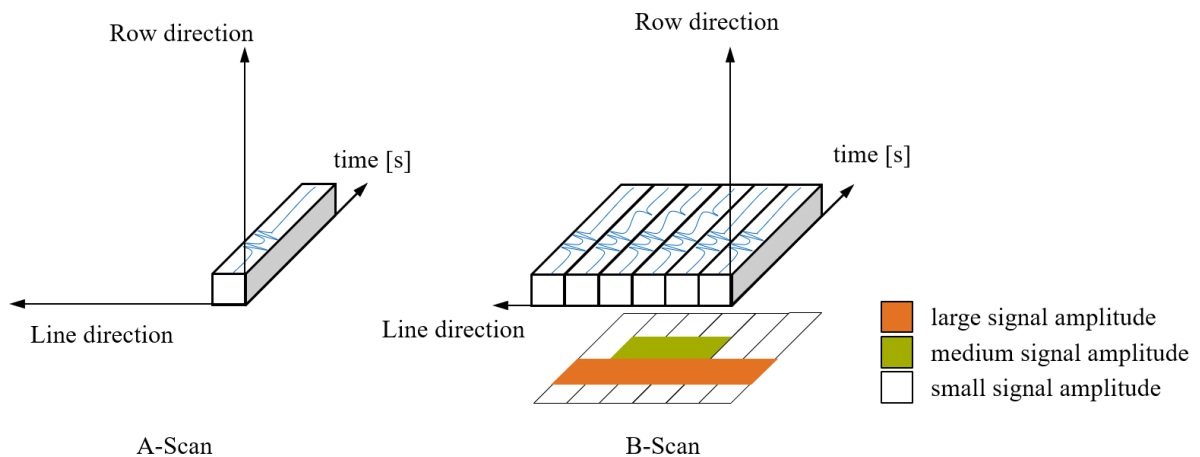


Figure 3.11: Visualization of the A-Scan and B-Scan representations. Row and Line direction represent the moving directions of the scanning device. Augmented representation following [Grager 2014]

C-Scan

To obtain a C-Scan image, multiple consecutive B-Scans are processed and visualized again in a 2-dimensional image. Each pixel in a C-Scan represents one A-Scan and therefore one point in space. It is possible to create a C-Scan image by moving the scanning device in a

meander-shaped path over the surface under test. The same considerations about color-mapping as with the B-Scans apply for the C-Scans. A multitude of processing methods are possible to obtain the final C-Scan image, and a few of them are presented in the following. Generally, the C-Scan only shows a fraction of the measurement information. It should be noted that in some cases it may be sensible to visualize a C-Scan as a three-dimensional surface instead of a colored two-dimensional image.

The first method, used by López-Baos (2018), is to analyze the frequency spectrum of the complete recorded signal and plot the value of its highest amplitude. This method is tailored to a transducer with narrow bandwidth, as no meaningful data can be obtained with a broadband sound source. When performing a band pass filter beforehand, the SNR of the image may be increased a lot with this method.

If the power of the recorded signals is of interest, the sum of the absolute squares of their time-domain samples can be calculated and divided by the signal length. Equivalently, the square of the RMS (root mean square) level can be calculated, which also represents signal power. This was done to obtain the power distribution images from sound field and surface scan data. The whole signal length was considered as the time window, as only relative differences of the power were of interest.

For the last method presented here, only a very small number of consecutive samples of a signal (a narrow window) are considered, starting from only one sample. Then, the average amplitude of these samples is displayed just like in the B-Scan. The difference here is that, with a single image, one only obtains information about one time instant. We decided to remove this limitation by creating a video of the C-Scans for each sample, as this method of data visualization requires no filtering or other post-processing with suitable data. In this written version of this work, individual frames of interest were extracted from these videos as depicted in Figure 3.12.

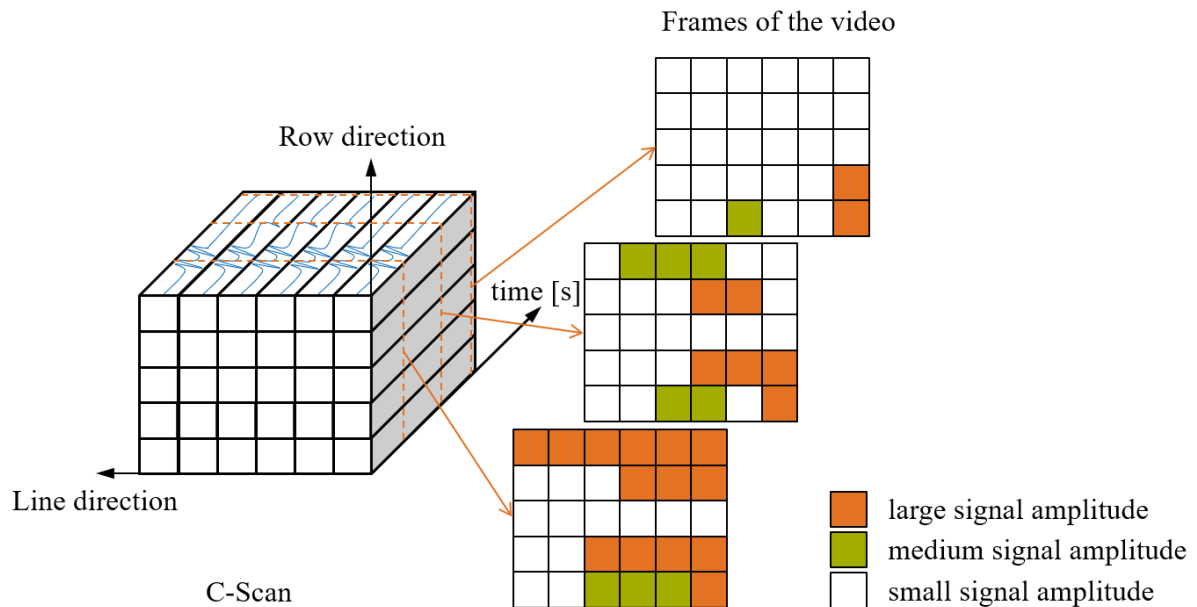


Figure 3.12: Visualization of the volume-scan and the extraction of C-Scans as video-frames at different time instances. The axes are the same as in Figure 3.11.

The term volume-scan refers to all the data obtained while performing measurements and capturing the complete A-scan at each measurement point. In the course of this work, volume-scans were the only form of measurement, as the other forms of presentation can all be extracted from them.

3.3.2 Filters and Averaging

Digital signal processing is valuable to improve the clarity and interpretability of data. However, if it is done carelessly the data can become skewed and false conclusions can be obtained. For this reason, the applied methods of signal processing are explained and discussed here.

Sound Field

The use of a narrow IIR band pass filter was suggested by Lopéz-Baos (2018) for the visualization of transducer sound fields. The SNR is improved through this method, and the sound field is clearly visible at greater distances of up to 200 mm from the transducer surface. However, the use of such a narrow bandpass filter significantly changes the phase information of the signal and shifts it in the time domain, rendering it useless for visualization in a video. Additionally, the sound fields recorded in this work had a measurement region of only 100 x 40 mm, so the visibility improvement in the regions further away did not matter. Thus, no filter was applied to the sound field measurements. The SNR in the measurement data was sufficient to obtain clear images.

Surface Scan

To present the transducer surface displacement data measured by the laser doppler vibrometer in a sensible range, a kind of filter was needed. Otherwise, the high-amplitude abrupt jumps and slow drifts would have distorted the image. The abrupt jumps were caused by the R2Z-method where the signal is set to zero upon reaching the maximum value (explained in section 2.4.2). Slow drifts most likely caused by the low-frequency vibrations and movement of the CNC table. As the signal frequencies of interest should be conserved as best as possible, only the static displacement was to be subtracted from the data. This static displacement was calculated with a moving mean filter applied to each recorded signal and each resulting data point was subtracted from the original one. The moving mean filter had a window size of one period length of a 400 kHz oscillation to smooth out the transducer's dynamic movement as good as possible.

Speckle noise as explained in 2.4.1 is clearly visible when looking at an unfiltered transducer surface image like Figure 3.13 (left). To improve the SNR and image quality, a one-dimensional moving median filter with a window of three pixels was applied first in horizontal and then in vertical direction. Different kinds of moving filters were examined beforehand, such as moving mean, Savitzky-Golay or gaussian averaged filters. The moving median filter is best suited for this application however, as it can smooth outliers such as speckle noise pixels with a very small window size as visible in Figure 3.13 (right). Moreover, it barely influences the shape of the underlying signal.

In some measurements, lines of data were corrupted due to unknown causes. Consequently, some parts of the image had to be repositioned manually and the corrupted A-Scans exclusively had zeros as their voltages. To smooth out the affected pixels, every A-Scan comprising of only zeros was set to "NaN" in the MATLAB matrix and thus was itself not considered by the moving median filter. The value of the corrupted pixels was therefore determined by the surrounding "good" pixels.

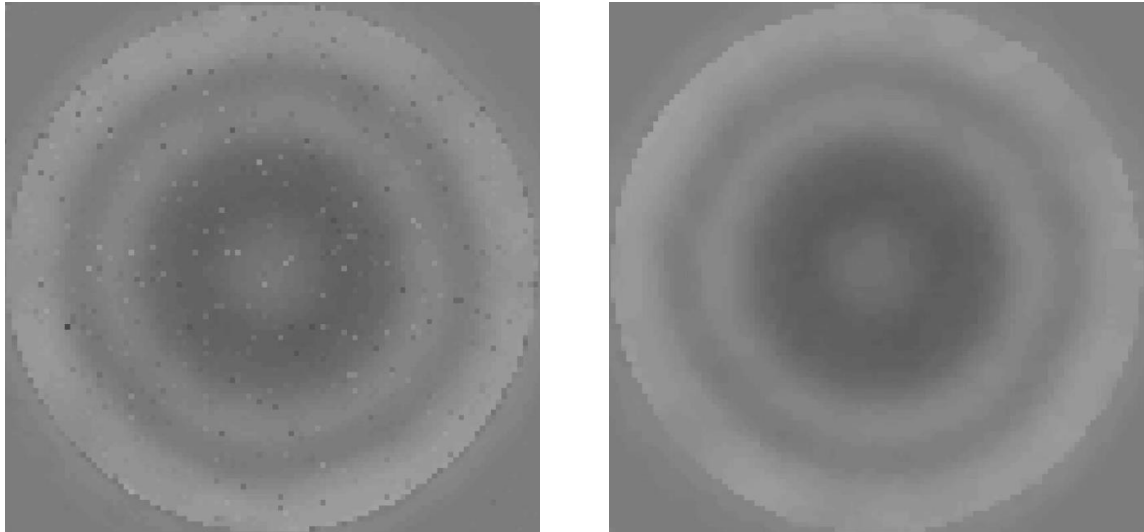


Figure 3.13: Transducer surface with speckle noise (left) and with smoothed-out speckle noise (right). The two images were taken from measurements with the same configuration.

3.3.3 Optimization of Data Conversion

We used the existing MATLAB scripts of López-Baos (2018) as a baseline and optimized them. A hindrance in the measuring process was the long time needed to convert data output by the TRANAX oscilloscope into a usable format. This prevented the insights of one measurement from influencing the settings for the next measurement. Due to the long time (20-30 Minutes) it took to convert the data the visualization was mostly done at the end of a measurement series. Figure 3.14 visualizes the data flow from the measurement to the final C-Scan images or volume-scan videos.

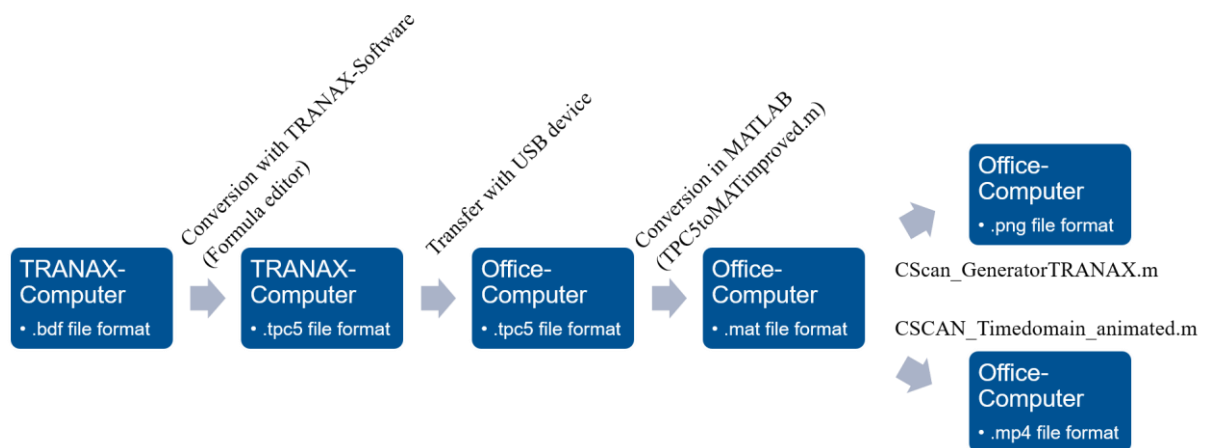


Figure 3.14: Data flow for the TRANAX oscilloscope, which was used for all measurements in this work. The .bdf files are created when measuring in Single- or Multichannel ECR-mode

Firstly, we replaced self-written functionalities in the script for generating C-Scans by onboard functions of MATLAB. This not only made the code shorter, but also decreased runtime and increased understandability as these functions are well-documented. Then we

created the script for generating videos of the volume-scan with the experience gained from rewriting the C-Scan script by López-Baos.

The improved “TPC5toMAT.m” was written after careful examination of the original file’s runtime where we discovered the function accessing the current state of the computer’s RAM dominating the time it took the function to execute. It was called for each A-Scan, typically 13,000 times for one measurement file. Since the data returned by this function did not change over time, it could be called only once in the processing of the measurement file without further affecting the functionality. This resulted in a time reduction of 0.039 s per pixel, so about 500 s for a typical measurement. A further improvement was made in the data output of the script, which is now the complete volume scan as a three-dimensional matrix. Its rows and columns (first and second dimension) correspond to the rows and columns in the measurement. The third dimension corresponds to the time dimension as indicated in 3.3.1. This data output is advantageous not only from a usability standpoint as compared to the old output of one measurement row per file, but also in improving runtime in the next scripts processing the data as they must access only one file from the hard-drive. Another new output of the “TPC5toMATimproved.m” script is a table (.mat file) of the measurement settings, which must be entered by the user before the conversion takes place. This ensures that settings and data are stored together as it is imperative to know for example the number of A-Scans that were recorded in the measurement. The output of a separate settings file also enables processing of multiple volume scans from one script, as the settings can be imported for each measurement along with the data.

The complete optimized scripts used for the data conversion and processing in this work are available in Appendix C.

3.4 Signal Flow and Disturbances in the Measuring Process

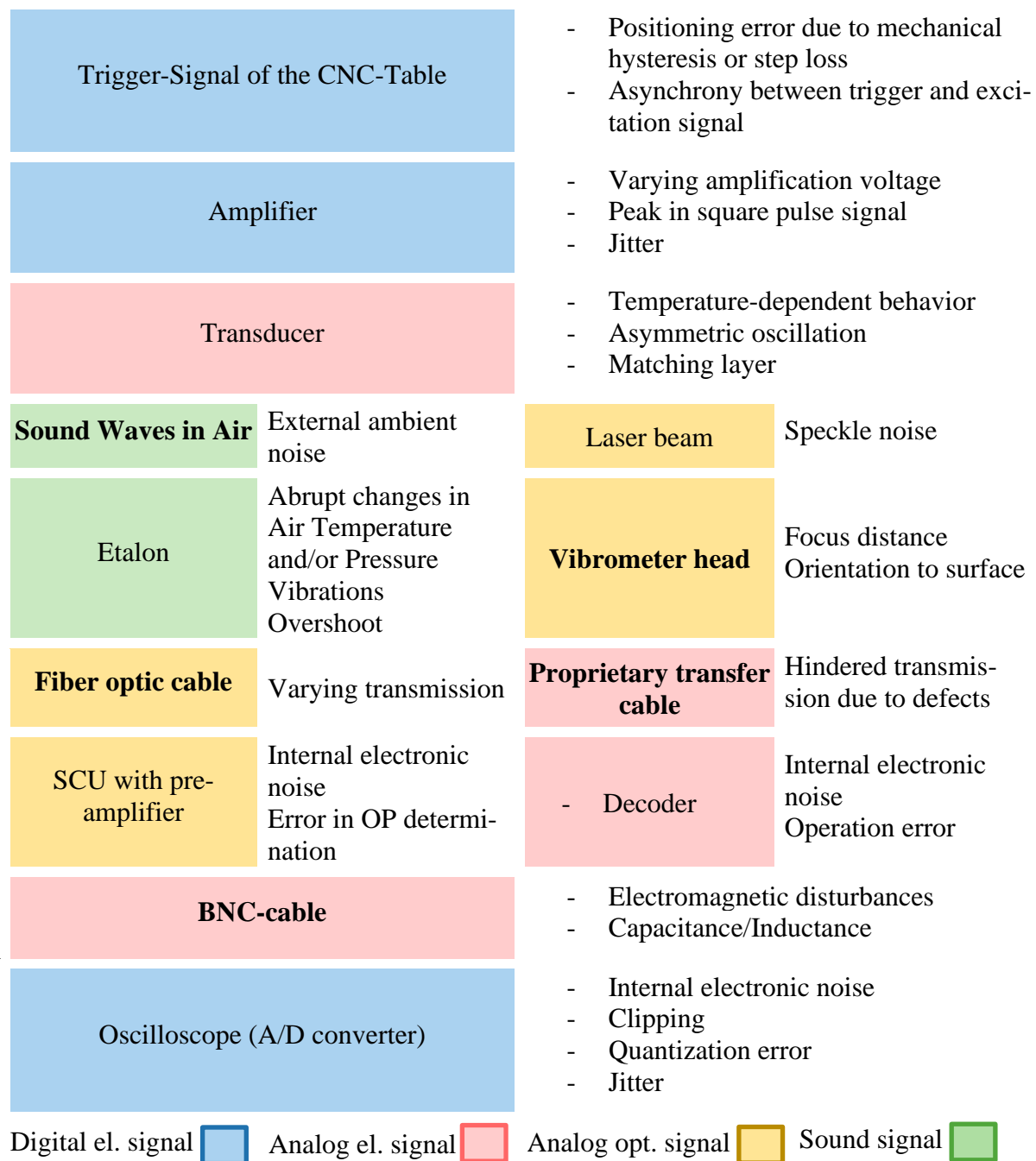


Figure 3.15: Overview of the signal flow in the measurement setup (in downwards direction). The left column contains the device or medium in which the signal travels, in the right column some disturbances are given. The rows of the measurement device are split, since optical microphone and vibrometer were used interchangeably at this point. The colors reference the input signal type of the respective device. Augmented representation following Gamper (2017).

Every element in the signal flow depicted in Figure 3.15 may alter the signal through inner and outer disturbances. However, the knowledge about which component acts on the signal and how it does so is insufficient for each single measurement as the disturbances can change over time. It is possible to estimate the most likely error with models and statistical methods, based on all accessible information. Repeating measurements and averaging results

can reduce statistical errors to negligible levels, however systematic errors will prevail. The error introduced into the signal by one “actor” is passed on down the signal flow and might be highly amplified by the end. Therefore, it is important to pay special attention to the first components of the signal flow when performing error analysis.

Multiple components mentioned in Figure 3.15 have been discussed in this chapter (or will be in the next chapter) regarding their influence on the signal. Here, the parts with bold text will be shortly explained and discussed.

Sound waves in Air

The influence of ambient noise might be significant in production environments. However, due to the broadband behavior of the optical microphone these noises can be filtered out if their frequencies are known. For this work, ambient noise was negligible since the sound field measurements were conducted in a mostly quiet room, and other sound sources had very different frequencies compared to the transducers.

Vibrometer Head

One LDV can inherently only measure movements perpendicular to the laser beam. If a surface is moving in its normal direction but is not perpendicular to the laser beam, a geometric error occurs where the measured deformation amplitude is reduced compared to the actual amplitude. In the extreme case of the beam and the surface laying in the same plane, this results in the surface movement not being measured at all. To obtain accurate measurements, it is therefore necessary to position the LDV head perpendicular to the surface as well as possible. When measuring vibrating spherical surfaces, it might be necessary to reposition the head such that it is perpendicular to each measured point. However, as the spherical radius of the physically focused transducer is much larger than its aperture radius, the geometric error can be neglected even if the vibrometer is not adjusted during the measurement.

Proprietary transfer cable

Barely any information about the transfer cable connecting the LDV head to the encoders is available other than that it transfers analog electrical signals. However, the cable is known to be very fragile and prone to break when loaded with a torsional force. Therefore, the cable was moved as little as possible overall and the least amount of torsion was applied to it. Other weak points are the joints of the cable to the connectors, which is why a tension relief was always applied when mounting the cable.

Fiber optic cable

Gamper (2017) found out that small bending radii of the optical microphone’s fiber optic cable deteriorate the signal amplitude even while staying above the minimal specified bending

radius. Therefore, the cable was kept as straight as possible for the sound field measurements, although some bends were inevitable to position the microphone correctly.

BNC-cable

The BNC-cable showed influences on the signal recorded by the oscilloscope in section 3.1.3. Namely, it changed the oscillation frequency of the spike oscillation. It is not clear whether this effect is caused by the impedance or the inductance added to the circuit by the cable.

4 Results and Discussion

In this chapter the results of the measurements will be discussed. In the first half, the transducer sound fields will be presented. Characteristic properties such as the sound velocities, maximum sound pressure level and beam diameters will be introduced. Then, the different transducer types will be compared based on the findings. The second half of this chapter will deal with the transducer surface scans, first again introducing the characteristic properties with focus on the mode shapes. Afterwards, the power distributions of the surface scans are presented and the visible inhomogeneities are explained. The electronically focused transducer will be covered in-depth in section 4.3, where its sound fields for different phase shift configurations will be discussed. Its obtained quantities are presented together with the other transducers in the previous two sections.

4.1 Transducer Sound Fields

The first section presents the results of the time-evolving sound fields for the physically focused transducers, where individual pressure domains can be identified. The second section discusses the sound fields' power distributions which are in their form more similar to the ideal sound field presented in Figure 2.5. Additionally, the results for all transducers introduced in 3.1.4 are shown.

The alignment of the optical microphone showed no visible deviation from vertical alignment, unless stated otherwise. Asymmetries in the sound field were therefore not caused by the directional sensitivity of the microphone.

4.1.1 Time-Evolving Sound Fields

Three frames extracted from the time-evolving volume scan (see 3.3.1) are visible in Figure 4.1. The frames show the sound wave in the near field, at the near field length, and in the far field respectively. Frames were chosen in which the second zero crossing of the sound wave fell exactly on an axis tick, i.e. at $x = 20$ mm, 50 mm and 100 mm.

Sound Velocity

From the distance traveled by the sound wave and the time taken for it, it is possible to calculate its phase velocity. The resulting velocities of the three sections (20 mm to 50 mm, 50 mm to 100 mm and 20 mm to 100 mm respectively) are given in

Table 4.1, along with the velocities resulting from same procedures for the other transducers that were investigated. The data show that the velocity from the section 20 mm to 50 mm is consistently lower (except for the CF400-3E) than for the other two sections, and the velocity calculated from 20 mm to 100 mm is close to the mean of the other two sections. The anomaly in the phase velocity of the electronically focused transducer is thought to be caused by the

shift in the excitation of the center electrode by $1.8 \mu\text{s}$ with respect to the outer electrode. It can further be observed that the averaged values of section 1 and 2 (weighted by the distances they comprise) match well with the velocity from the third section. This match is accurate to 0.01 m/s in the calculation. However, as the measurement increment is 0.2 mm , the precision of the method only permits three significant digits to be displayed here.

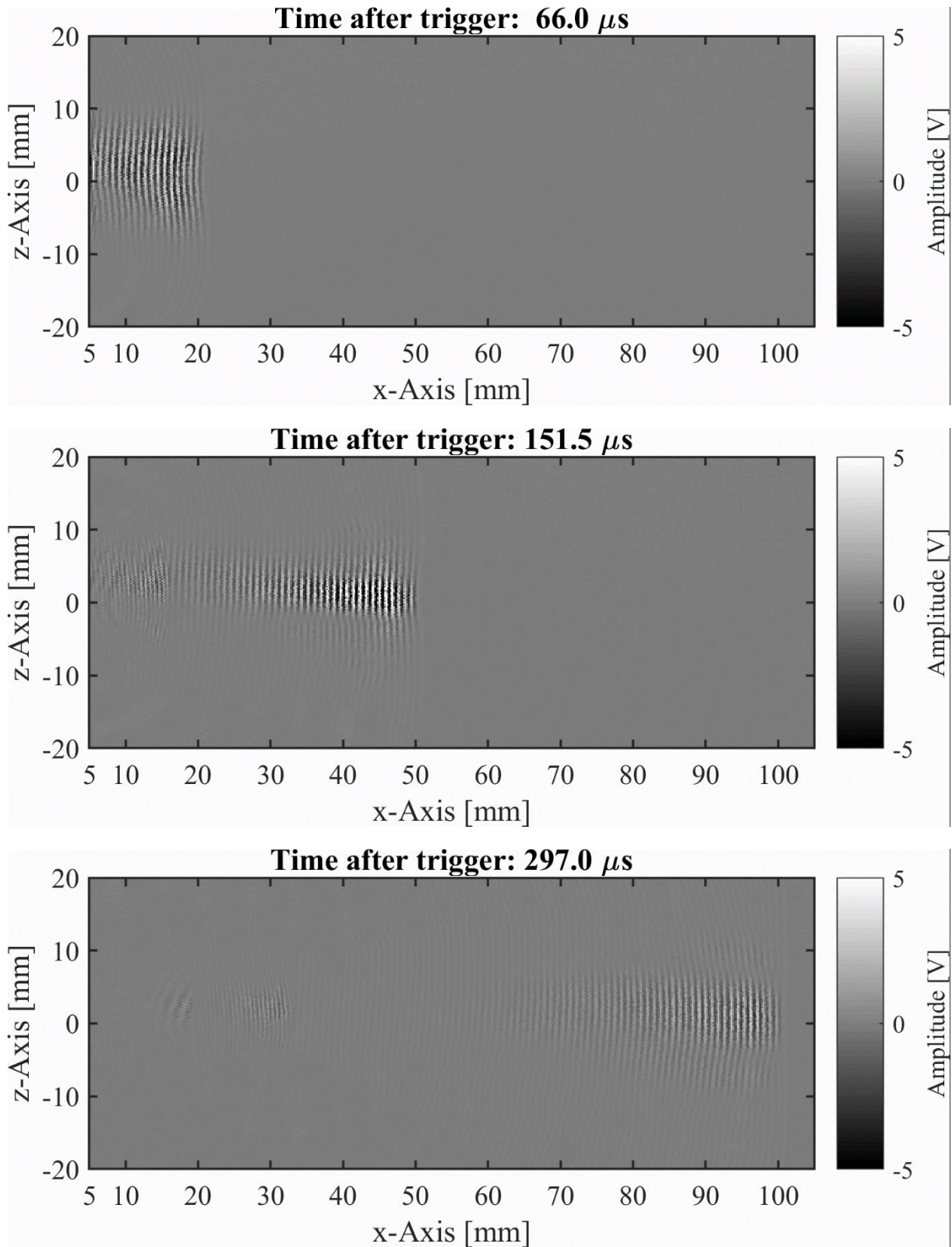


Figure 4.1: Extracted frames of the sound field time-evolution. Transducer: CF400. The title of each frame includes a timestamp indicating the time since the trigger signal (rising edge). The axes indicate the respective distance to the center of the transducer surface.

Table 4.1: Results of the phase velocity obtained from the transient sound fields for three different sections. Section 1: 20 mm to 50 mm, Section 2: 50 mm to 100 mm, Section 3: 20 mm to 100 mm. The velocities are all given in [m/s].

Transducer	Section 1	Section 2	Section 3	Average of 1 & 2
CF400	351	344	346	346
CF400-3E	345	346	346	346
ULT200	348	346	347	347
AT200	-	347	-	-
AT75	353	348	350	350

The explanation as to why the velocities in the three sections are different in the first place relies on the theory introduced in 2.1.4. Note that phase and group velocity of a wave only match exactly in a dispersion-free medium. It has been shown however that under ambient conditions ($T = 20^\circ \text{C}$ and $P = 101325 \text{ Pa}$) air is dispersive for sound waves above 100 kHz [Álvarez & Kuc 2008]. Therefore, the phase velocity is a function of frequency and the results in

Table 4.1 match neither each other nor the calculated velocities presented in Table 2.1. The dispersion is also an indicator for the attenuation of the sound waves, which would otherwise be practically unobservable in the short distance covered by the measurement.

Echoes

Another noticeable effect when looking at the time-evolving sound field of the CF400 transducer are the second and third wave trains that propagate behind the first. These are identified as echoes from the initial sound being reflected first by the microphone and then by the transducer at least once before being picked up by the microphone. During measurements, additional tests were conducted with porous foam mounted between the microphone and its (comparably large) mounting frame in order to reduce the reflected sound and thus the echoes. However, the foam used did not have the expected behavior and reflected the sound instead of absorbing it, causing additional interferences. Therefore, only data recorded without foam is presented here.

In Figure 4.2 a frame of the time-evolving sound field is depicted with color scale expanded around zero. This results in the waves with lower amplitude being visible while losing all detail of the amplitude in the primary wave train. The echoes occur in the region of $x < 35 \text{ mm}$. They seem to each have a smaller wavelength than their preceding wave front. This is caused by the frequency of the sound staying constant when being reflected, but the time it takes for the sound to be recorded by the microphone increases by twice the travel time between transducer and microphone per echo order. Therefore, the virtual sound velocity of

the first order echo is reduced by a factor of three compared with the actual sound velocity, the second order echo by a factor of five, and so on. Consequently, the apparent wavelength in the image is reduced by the same factor while the frequency remains at its original value ($\lambda = c / f$). This causes spatial aliasing in the case of the second order echo, since the virtual wavelength cannot be resolved by the chosen resolution. It is hypothesized that the spherical curvature of the transducer focuses the echo on the microphone, making it much more pronounced when observing physically focused transducers compared to the planar transducers.

Focusing Behavior

A focusing behavior can be clearly observed from the first frame to the second in Figure 4.1, causing the maximum measured voltage to rise. One frame (not shown here) showed voltages of up to 7.0 V, which would correspond to a sound pressure of 1.4 kPa or a SPL of 157 dB. However, these values should not be taken as absolute, as the factor given by the manufacturer for relating voltage and pressure was not validated. The maximum voltages along with the calculated SPL for all the measured transducers are obtainable from Table 4.2. Due to the uncertainty in the conversion factor described in section 2.3.3, an error of ± 1.5 dB is estimated in the given sound pressure levels. It should be noted that the SPL of the ULT200 would be higher if the set voltage range had not been exceeded. Therefore, the error of this value is considered to be much larger.

Table 4.2: Maximum measured voltages and calculated SPL (considering the amplification) for the sound field of each measured transducer. *The recording range for the ULT200 was set too low, thus data clipping occurred.

Transducer	Maximum voltage [V]	SPL [dB]
CF400	7.08	157 \pm 1.5
CF400-3E (0-900-1800 ns)	6.27	156 \pm 1.5
ULT200*	2.56*	148*
AT200 (-12 dB)	2.54	160 \pm 1.5
AT75 (-12 dB)	5.08	166 \pm 1.5

The second frame shows a wave front with an asymmetry with respect to the x-axis. When looking at the moving video, one might have the impression of the wave traveling diagonally upwards, however, this is not the case as the normals (rays) of the individual partial waves point (with few local deviations) in the x-axis direction. The asymmetry is rather a consequence of the asymmetric transducer oscillation behavior, which will be discussed in more detail in section 4.2.2. If the transducer were rotated by 90 degrees about the central axis, this asymmetry would presumably disappear.

Results with Lower Colormap Amplitude

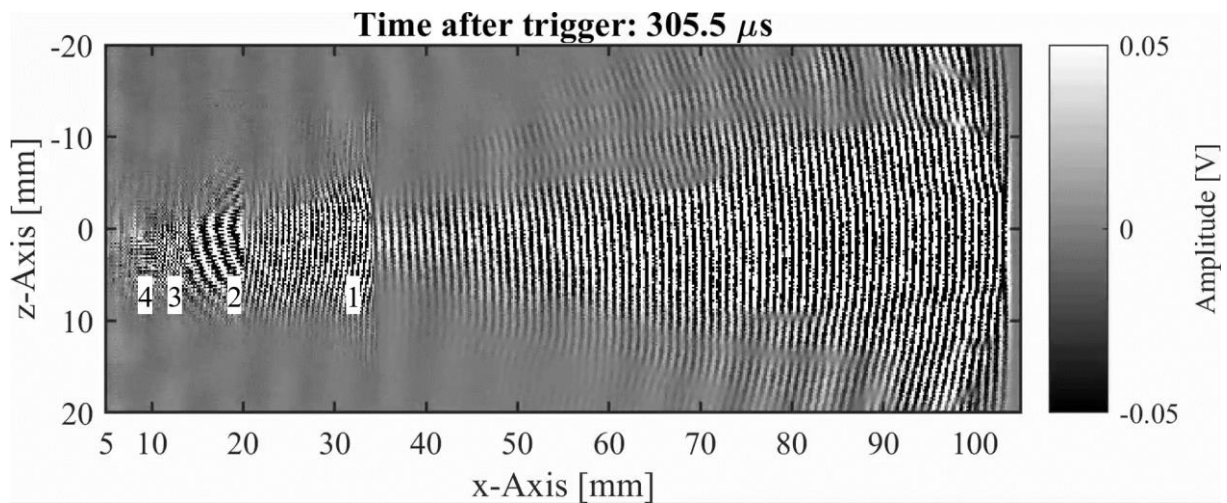


Figure 4.2: Frame of the time-evolving sound field with drastically reduced colormap limits. Echoes up to the fourth order are visible (marked) and their wavelengths are distinguishable. An oscillation with lower frequency and amplitude is also observable. The same plotting conventions as in Figure 4.1 apply.

When observing areas upwards and downwards from the central (horizontal) axis in Figure 4.2, one notices another oscillation with both lower amplitude and frequency (i.e. longer wavelength). This oscillation is also present in the sound field of the electronically focused transducer of the same manufacturer, but no other transducer showed a similar behavior. Analyzing the spectrum of the points where this oscillation is visible reveals a frequency of about 56 kHz, which matches observed peaks in the transducer's surface scan (section 4.2). Besides this oscillation, another oscillation with a frequency around 800 kHz can be observed both in sound field and surface scan frequency spectra. At this stage it is not clear which part of the transducer (piezo-composite material, backing material, matching layer or matching electronics) causes these oscillations.

Characteristics of the Other Transducers

The near field is practically non-existent in the measurements with the ULT200 depicted in Figure 4.3, as its spherical radius is much smaller and the focusing effect is therefore much larger than with the CF400. Moreover, the active surface diameter of the ULT200 is only 12.5 mm compared to 20 mm for the CF400. This results in the generation of pronounced side lobes visible especially in the first and second frames. They can also be observed in the power distribution (Figure 4.6). In the first frame, close to the transducer surface the wave front is still concave while becoming more straight further along the x-axis. The second frame shows that the waves in the area with high amplitude have straightened out completely, while the side lobes are already convex. In the third frame, all parts of the wave train are convex. A similar evolution of the wave shape can be observed in the images for the CF400.

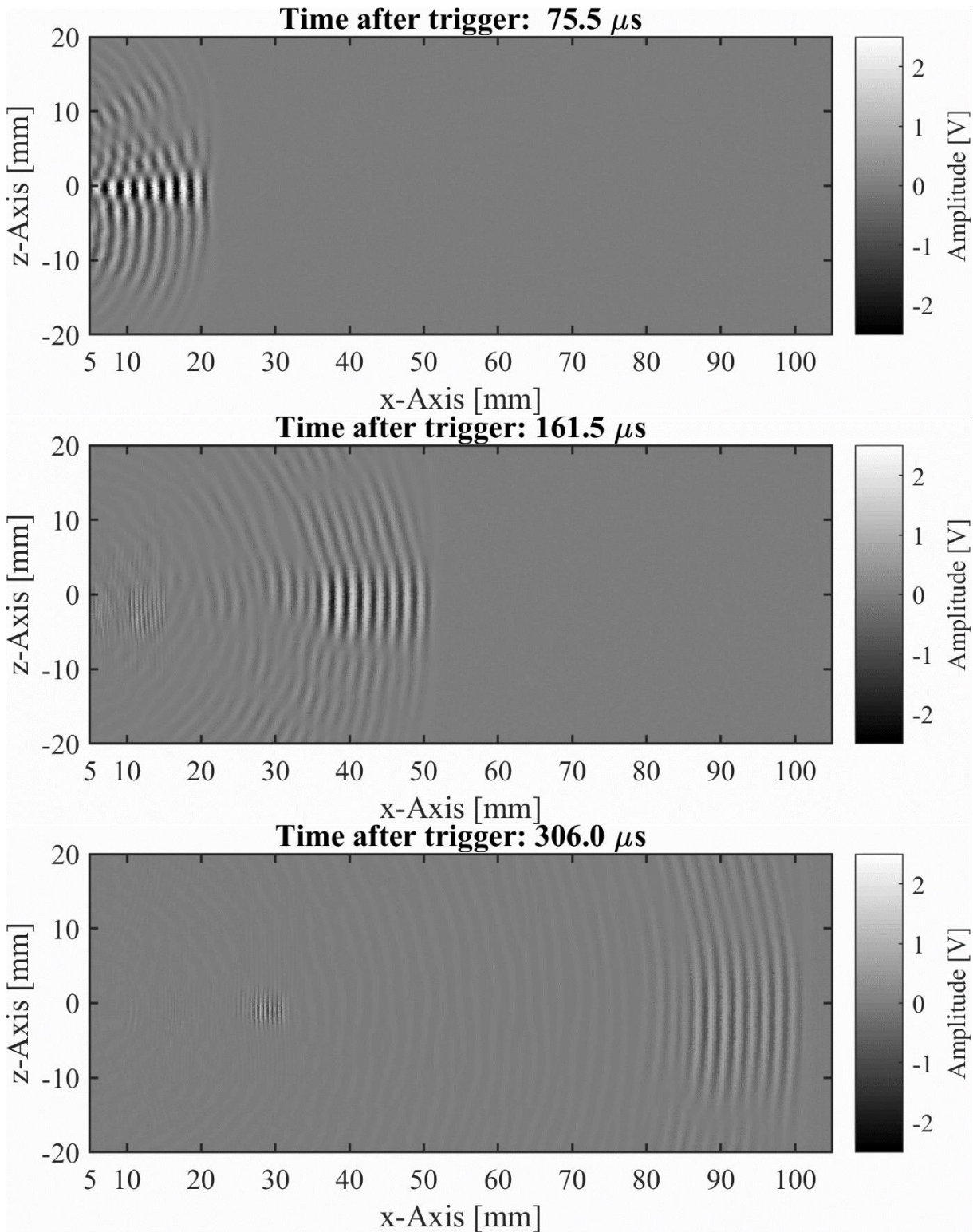


Figure 4.3: Extracted frames of the sound field time-evolution. Transducer: ULT200. The same plotting conventions as in Figure 4.1 apply.

An obvious difference between the sound fields of the CF400 transducer presented in Figure 4.1 and the ULT200 shown in Figure 4.3 is the sound’s wavelength. The wavelength is twice as large for the ULT200 than for the CF400 due to their respective excitation frequencies. By measuring the distance over an integer number of waves, as illustrated in Figure 4.4,

and dividing by that number, the wavelength can be determined with increased accuracy compared to the measurement of only a single wave. The results for this procedure are summarized in Table 4.3. It is notable that for both 200 kHz transducers the measured wavelength value was higher than the value calculated from excitation frequency and speed of sound. For the other transducers, the measurements agree with the calculated values within the margin of error. The most likely explanation for the deviation of the 200 kHz transducers is that their eigenfrequencies are lower than the specified 200 kHz. For the ULT200 this could be confirmed as it has a peak frequency of 186 kHz according to the inspection record given by the manufacturer.

Table 4.3: Wavelengths of the transducers (measured and calculated).

Transducer	i	Measured wavelength [mm]	Calculated wavelength [mm]
CF400	20	0.89	0.86
CF400-3E	20	0.88	0.86
ULT200	11	1.8	1.7
AT200	11	1.8	1.7
AT75	7	4.5	4.5

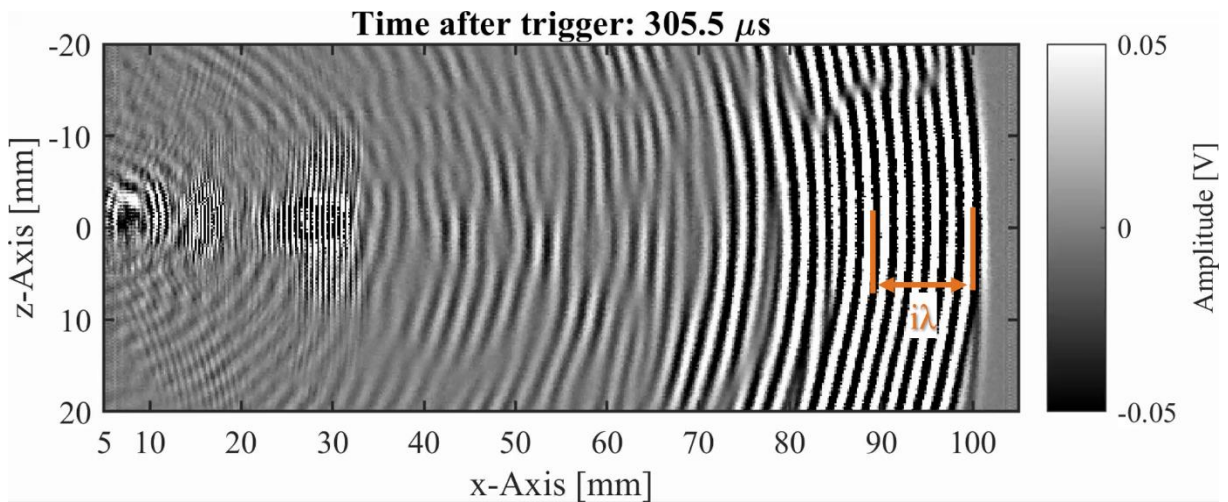


Figure 4.4: Frame of the time-evolving sound field of the ULT200 transducer with drastically reduced colormap limits. Interference patterns are visible in the middle and echoes with different propagation directions are observable. The method of determining the wavelength is visualized in orange. Here, $i \in \mathbb{N}$. The same plotting conventions as in Figure 4.1 apply.

The transducer surface of the ULT200 is mounted in a recessed position in relation to the steel mounting bracket. This causes interference patterns in the traveling wave, and echoes not necessarily parallel to the original wave front. The origin of the artifact at $x = 7$ mm and $y = -3$ mm in Figure 4.4 is again spatial aliasing. It represents the fourth order echo.

Compared to the similar visualization of the CF400, the ULT200 shows less damping behavior, as there are still parts of the original frequency clearly visible in Figure 4.4 for $x < 30$ mm, which is not the case for the CF400. It is therefore likely that damping in the CF400, and by extension the CF400-3E, is significantly higher than in the ULT200. This can also explain the low-frequency vibration observed for the CF400 transducer as the system of piezo composite plate and damping body will have a lower eigenfrequency than the piezo composite alone.

4.1.2 Power Distribution of Sound Fields

The power distribution was determined as the square of the RMS level of the obtained signal at each point, according to 3.3.2. The recorded signal considered for the calculation had a length of 500 μ s. The results will be discussed in the same order as the transient sound fields. Additionally, the results of the planar transducers (AT200 and AT75) will be shown in this section.

CF400

A focusing effect can be observed in the sound field of transducer CF400 depicted in Figure 4.5. The near field length is somewhere between $x = 30$ mm and $x = 40$ mm, converging and diverging fields are visible in the greenish color. The near field is broadened by the echoes, which is especially visible at the horizontal line of higher intensity at $z = -12$ mm. Furthermore, the interference of the echoes with the original sound wave is observable at $x < 15$ mm, 0 mm $< z < 10$ mm. Due to the long pulse length, the first wave train has not decreased before the echoes arrive and thus the two components interfere. This creates a wave-like structure in the power distribution images, the wavelength of which matches that of the first echo. The effect can also be observed in the sound fields of the other transducers.

Two side lobes separate at $x \approx 60$ mm, where the one below the $z = 0$ axis is stronger than the side lobe above. Smaller (ray-like) side lobes are visible at lower x -values with higher divergence angles than the main lobes or the prominent side lobes. These characteristics will be observed in varying degrees in the sound fields of the other transducers as well. The measured sound field and values extracted from it agree well with the results of the CF400's manufacturer [Mück & Scheunemann 2018]. It should be noted however that the resolution and sensitivity of the images presented here exceeds the ones of the manufacturer due to the use of the small-aperture optical microphone.

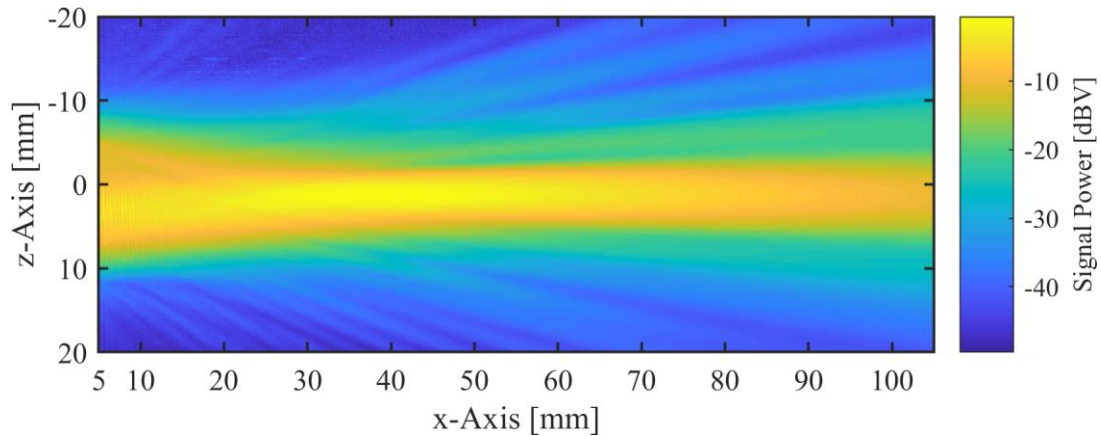


Figure 4.5 Power distribution of transducer CF400 (physically focused). Settings: 100 V, 5 pulses, 0 dB gain.

The calculated focal length by using the spherical radius obtained in section 3.1.4 is 49.6 mm, which agrees well with the specifications by the manufacturer (50 mm). The measured focus point (i.e. point with highest signal power) is at $x = 38$ mm, however the manufacturer states that positioning the transducer 50 mm from the target surface is advisable due to the separation of side lobes [Mück & Scheunemann 2018]. The diameter of the sound beam at this point is 4.2 mm, which is much larger than the value calculated with equation (2.16) of 1.1 mm. The x -axis positions of the point of highest amplitude, the -6 dB radius at that position and an estimation of the -6 dB opening angle are listed in Table 4.4, where the calculated values for these quantities are also given.

Other Transducers

The sound field of the physically focused ULT200 in Figure 4.6 shows much more pronounced side lobes than the CF400. This is caused by the lower spherical radius, i.e. the more concave shape of the transducer surface. The side lobes are not entirely symmetric with respect to the central $z = 0$ axis, three lobes can be observed above and four can be observed below it, with the opening angle of the main lobe being also asymmetric. A very small near field distance can be observed, as the field is diverging from the start, corresponding to a distance of 5 mm to the transducer housing. It should also be noted that due to a faulty range setting on the oscilloscope data clipping occurred and the near field length is not precisely determinable.

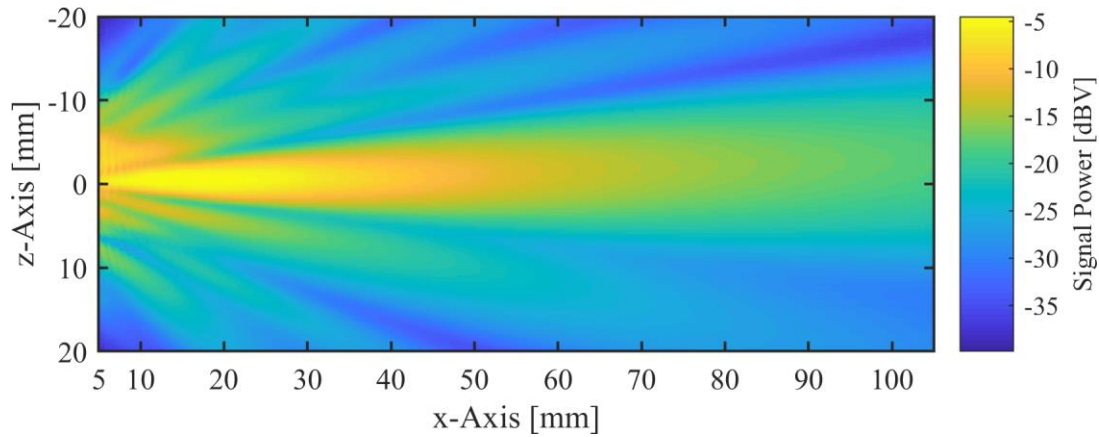


Figure 4.6: Power distribution of transducer ULT200 (physically focused). Prominent side lobes are visible. Settings: 100 V, 5 pulses, 0 dB gain.

The sound field of the AT200 depicted in Figure 4.7 clearly shows the influence of the incorrect trigger setting, as the area $x < 15$ mm is comprised only of the echo. It is furthermore visible that this is not a focused transducer, as the divergence angle is very large compared to the previously presented figure. This transducer and the AT75 had to be recorded with a gain of -12 dB on the optical microphone, as the occurring SPL would have otherwise exceeded its maximum output voltage.

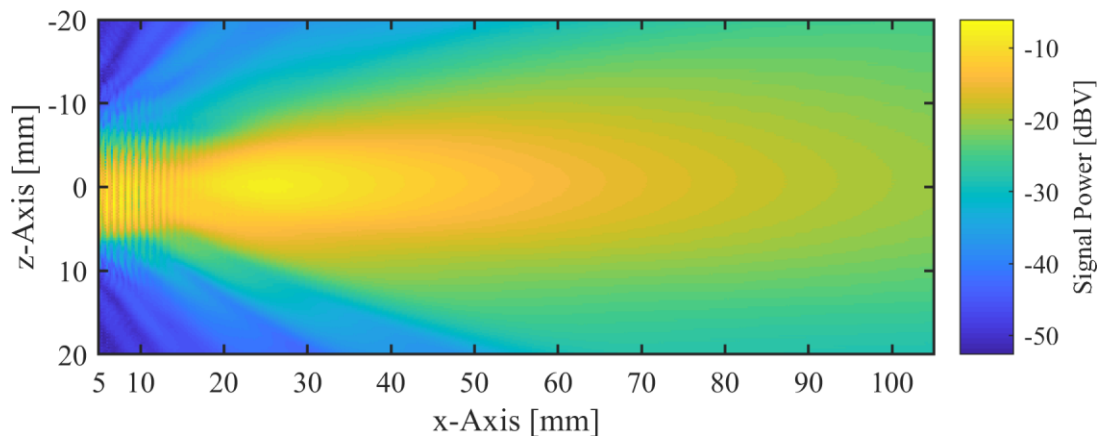


Figure 4.7: Power distribution of transducer AT200 (planar). As the trigger setting was incorrect for this measurement, the first 15 mm on the x-Axis are defined by the echo. Settings: 100 V, 5 pulses, -12 dB gain.

Figure 4.8 shows the power distribution of the AT75 transducer. The chosen measurement dimensions are too small for this transducer, which has an active diameter of 44.5 mm. Thus, no differentiation between near field and far field can be made, however some small side lobes can be perceived in the upper and lower left corners. Up to $x = 30$ mm, influences of the echoes are visible.

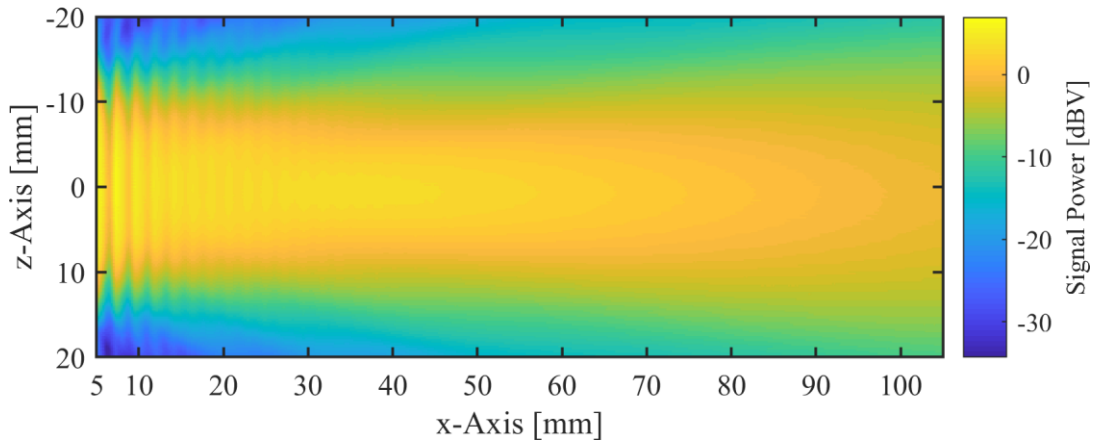


Figure 4.8: Power distribution of transducer AT75. The measurement area is not large enough to fully depict the sound field. Settings: 100 V, 5 pulses, -12 dB gain.

Comparison with Calculated Values

It is visible in Table 4.4 that most measured values have a large discrepancy to their calculated counterparts. The good agreement of the measured focal length presented here and the value published by the manufacturer for the CF400 was mentioned above. The calculated value for this transducer also agrees with the manufacturer specifications. It therefore seems likely that there is a systematic error in the formula (2.13) used to calculate the focal length. For the near field lengths of the AT75 and the electronically focused transducer the observed deviations are especially large. As can be seen, the calculated values lay outside of the measurement area of 105 mm in front of the transducer, and the width of the measurement with 40 mm is too small to depict the large field of the AT75. Thus, the measured value is not the near field length, but another point of maximum amplitude in the near field, as depicted in Figure 2.5. The electronically focused transducer is not expected to behave as a planar transducer, explaining the large deviation. For the ULT200, the calculated focal distance from the measured spherical radius is 7.8 mm. The manufacturer however states a focal length of 38 mm, which coincides to a spherical radius of 302 mm with the given active diameter and nominal frequency. These values show a high discrepancy to the measured ones. Therefore, it seems likely that the manufacturer gave the spherical radius as focal length.

Table 4.4: Extracted values of the sound fields compared with calculated values.

Transducer	Near field / focal length		-6 dB radius		-6 dB opening angle	
	Measured	Calculated (2.13)&(2.15)	Measured	Calculated eqn. (2.16)	Measured	Calculated eqn. (2.14)
CF400	38.2 mm	49.6 mm	2.1 mm	1.1 mm	4°	1.7°
ULT200	~ 13.8 mm	7.8 mm	1.8 mm	0.6 mm	9°	5.5°
AT200	24.8 mm	18.0 mm	5.1 mm	1.4 mm	23°	6.2°
AT75	35.8 mm	108.2 mm	10.0 mm	5.7 mm	-	4.1°
CF400-3E (0-900-1800)	17.6 mm	116.6 mm	3.0 mm	2.6 mm	2°	1.7°

The calculated values for the sound field radius at near field length show significant deviations to the measured values for all transducers. To understand this better, a closer analysis of the equation (2.16) would be necessary to determine how the constant factor (0.257) in it is initially calculated. With this knowledge a statement would be possible whether the equation or the measurement is the cause for the large deviation.

For the measurement of opening angles, the maximum amplitude of each measurement column was taken, and the other values of the column were normalized with respect to it. This accounts for sound intensity loss due to attenuation and allows for a clearer identification of the far field. An exemplary image with lines marking the edges of the -6 dB (corresponding to an intensity loss of 50 %) is displayed in Figure 4.9 for the ULT200 transducer. Measured and calculated opening angles (indicated in orange) obviously do not agree. It is also visible that the downwards angle is larger than the upwards angle. The effect of the echo close to the transducer surface and the first side lobes are also visible in this image due to their relative intensity. For the AT75 the opening angle could not be determined with this method, as no far field could be observed.

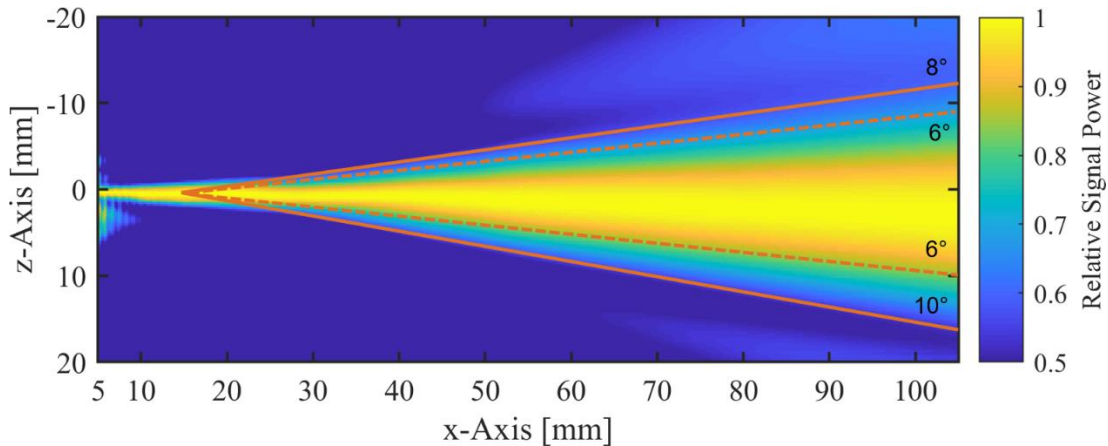


Figure 4.9: Visualization used to determine the opening angle with modified colormap. Transducer: ULT200. Orange lines: measured (full) and calculated (dashed) opening angles (rounded to full degrees). An asymmetry in the divergence angle is visible.

The question arises why there is such a large difference between analytical calculations, the manufacturer specifications and measured data. There are no widely accepted norms for characterizing sound fields of ACU transducers, so it is not always clear for example what methods the manufacturers use to determine quantities such as the near field or focal length [Steinhausen 2019]. This already starts at the definition of the two mentioned terms, as became clear for the ULT200 transducer. Another factor leading to the discrepancies are the equations which may not consider key properties of the transducers generating the sound field and finally, different measurement configurations may lead to different results. We hope to determine the source for these errors by comparing the analytical predictions and the measured data to simulations.

4.2 Transducer Surface Scan

Measurements of the surface oscillation were recorded for the CF400 and CF400-3E transducer only. In the first section, the oscillation modes of the transducers will be analyzed and compared to the results from similar studies, especially [Pohl et al. 2012]. The second section will deal with the inhomogeneities observed in the surface oscillation and power distribution data. All figures shown are obtained from the displacement data processed according to 3.3.2, unless stated otherwise.

It should be noted that the laser or the LDV shone onto the matching layer of the assembled piezoceramic transducer, not the piezo element itself as has been realized in other works [Huang et al. 2004, Pohl et al. 2010]. Since the matching layer has a low acoustic impedance it tends to be a soft material i.e. it has a low modulus of elasticity. This can result in large deformations which do not necessarily relate to the movement of the piezo composite (see 3.1.4). The most probable influences are change of phase and damping of certain frequencies. Some previous work has been done in measuring similar transducers with applied

matching layer, where the possibility of spatially resolving the oscillation was determined [Steinhausen et al. 2016a].

It should also be noted that the mode shapes presented in Figure 2.6, which are referenced in this section, are vibrations of a membrane. In the case of the transducer surface it is assumed that the vibrations take place on a finite volume (consisting mainly of the piezo element and backing material) and not a two-dimensional membrane. However, as the theory of membranes is well understood and easy to implement, this model was taken as a starting point.

4.2.1 Mode Identification

As in section 4.1.1, a few characteristic frames are presented for each transducer measurement. The frames were selected according to the clarity of the observed shape. First, the velocity data of the CF400 excited with 100 V and 1 pulse is presented (Figure 4.10), as it best shows this transducer's oscillation behavior. The typical excitation with five pulses at 400 kHz has a total length of 12.5 μs ($5 \times 2.5 \mu\text{s}$). The time displayed on each frame shows again the time since the initial trigger signal, making a clear allocation of the "first", "second" etc. frames possible.

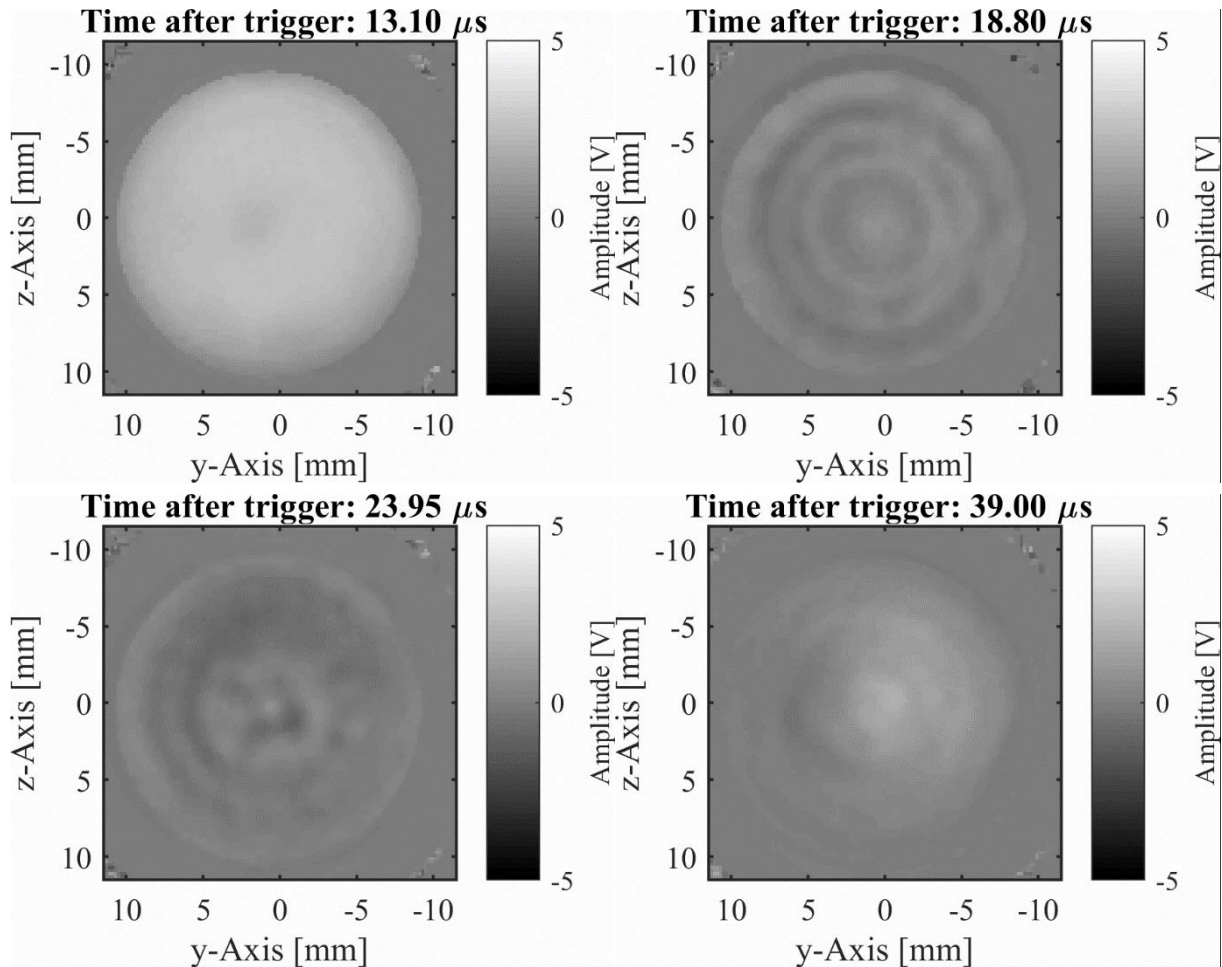


Figure 4.10: Selected frames of the surface scan (velocity data). Transducer: CF400 with 100 V and 1 pulse excitation, rotated 90° counter clockwise.

CF400

In the first frame, the transducer is almost uniformly deformed due to the excitation voltage. Only a small spot in the middle has a lower amplitude than the surrounding area. No mode shapes are observed here. As this is the only excitation pulse received, everything after the initial pulse is considered a free vibration. The second frame (time 18.8 μ s) shows what are presumably concentric surface waves traveling inwards. The inwards traveling direction of the waves reverses at about 30 μ s, where after similar waves are observed traveling outwards. Three concentric rings of positive voltage and a circle in the middle of the transducer surface are visible in the second frame. At one and four o'clock the rings are not distinguishable from the areas with negative voltage. The third frame shows a cross shape in the center of the transducer surface, which in the video seems to match the (4,1) mode presented in Figure 2.6. In the fourth frame, a mode shape closely resembling the (1,1) and (1,2) mode from the same graphic is visible. This is the longest lasting shape observable on the transducer, vibrating for well over 100 μ s. It is the main cause for the asymmetric power distribution observable in Figure 4.14. Similar mode shapes as this were also found in other works investigating

monolithic piezo ceramic disks, however in their measurements they did not observe an asymmetric behavior [Huang et al. 2004, Pohl et al. 2010].

CF400-3E

Three main configurations of the electronically focused transducer were tested. The power distribution was determined again as the square of the RMS level of the obtained signal at each point. First, only the inner electrode was excited, afterwards only the outer electrode. The last test was conducted with a phase shift of 0-900-1800 ns. The displacement data will be presented as a three-dimensional surface.

The first frame in Figure 4.11 shows the excitation of the inner electrode only. It is visible that the border of the electrically excited surface is much more gradual than in Figure 4.10, where the whole transducer is excited. This is caused by the abrupt change in mechanical properties at the border of the transducer for the case depicted in Figure 4.10. The smoothing the transition region of the inner electrode is electrical crosstalk, where the electric field penetrates the surrounding areas of the transducer surface. The second frame then shows the situation 0.4 μ s after the first. A small circle in the center with a radius of 1.1 mm is oscillating phase shifted to the adjacent region. This area exceeded the maximum measurable velocity of the LDV in the first measurements, which caused an artefact vibrating with three times the frequency of the surrounding area. This artefact did not occur for the displacement measurement; hence this data is presented here.

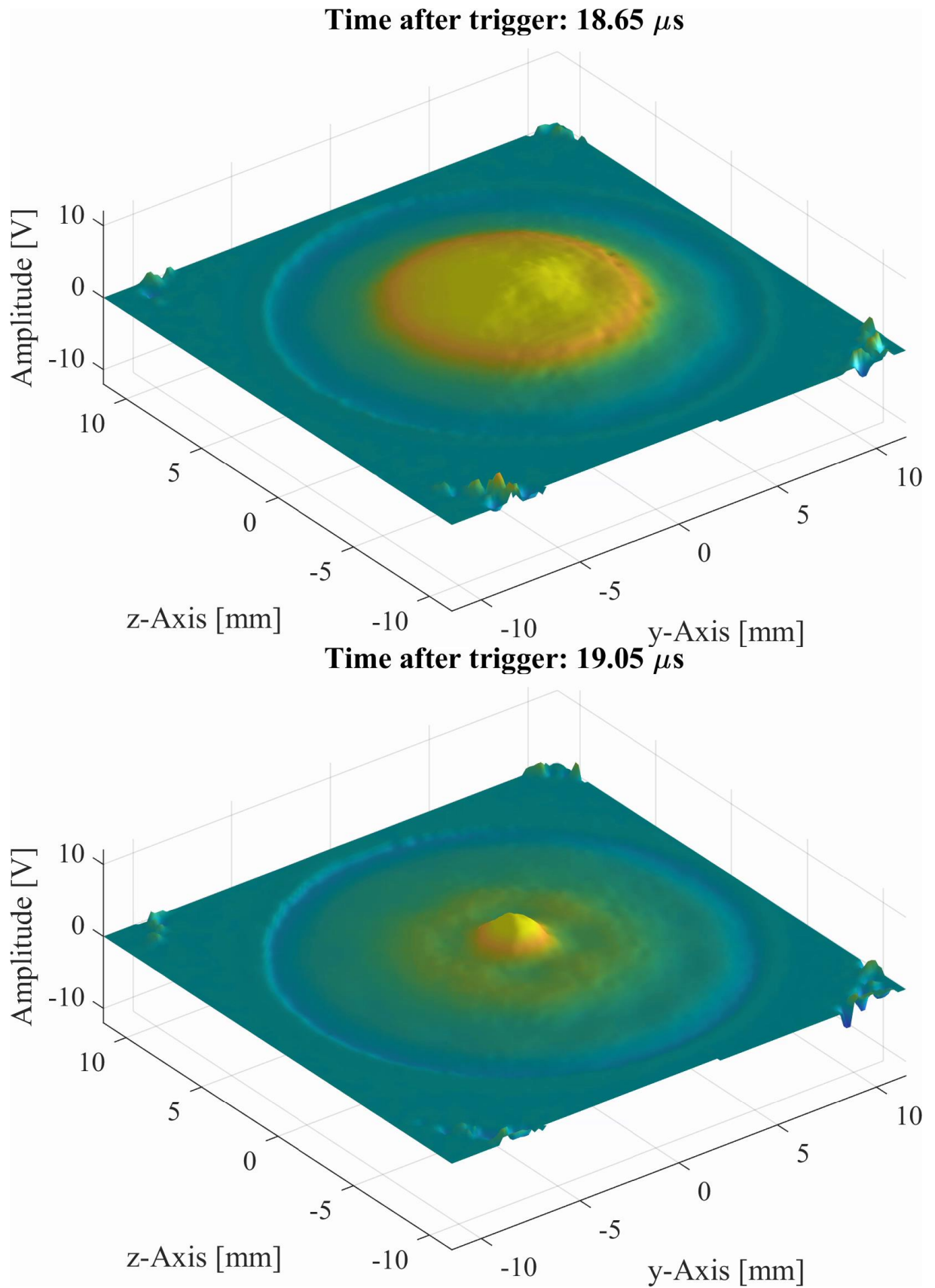
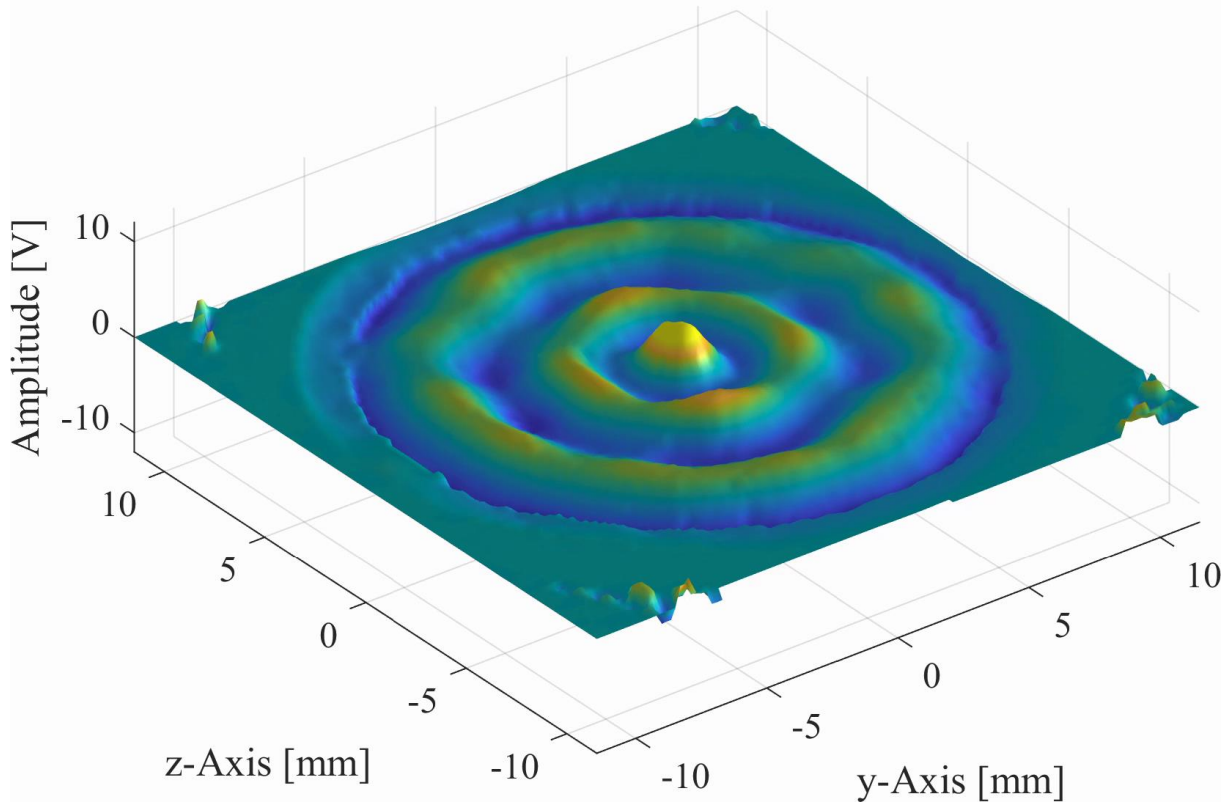
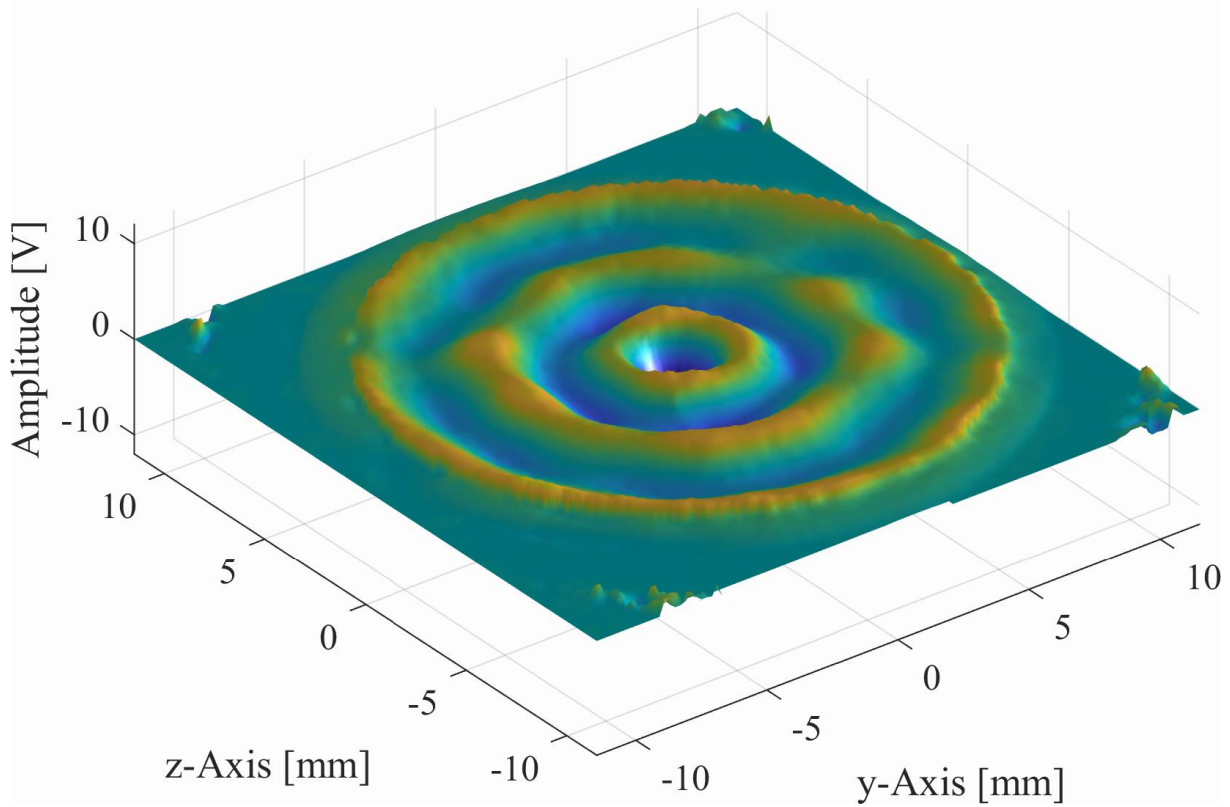


Figure 4.11: Selected frames of the surface scan (displacement data). Transducer: CF400-3E with excitation of inner circle only (100 V, 5 pulses). Note the small time difference between the frames.

Time after trigger: 22.90 μs



Time after trigger: 24.05 μs



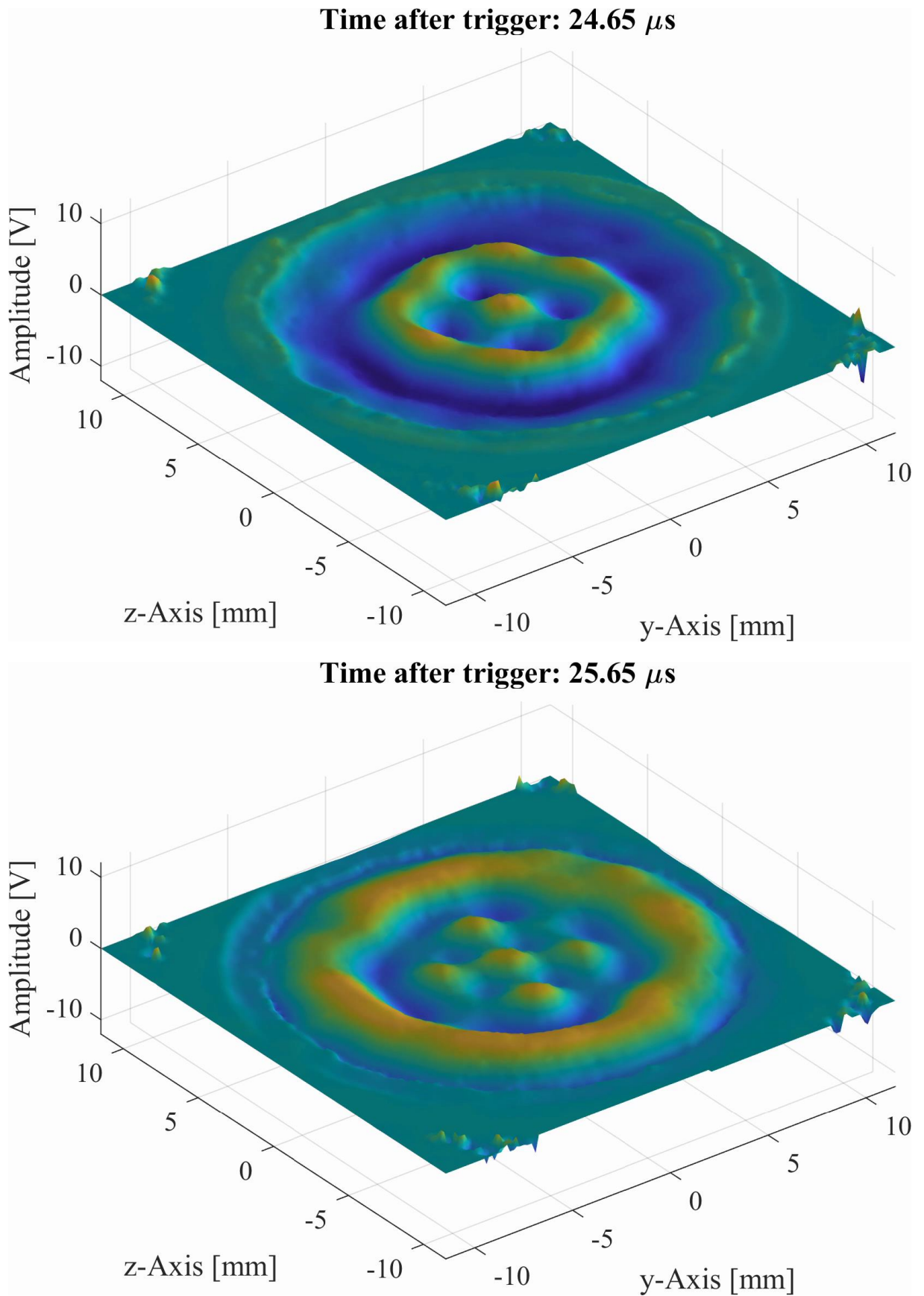


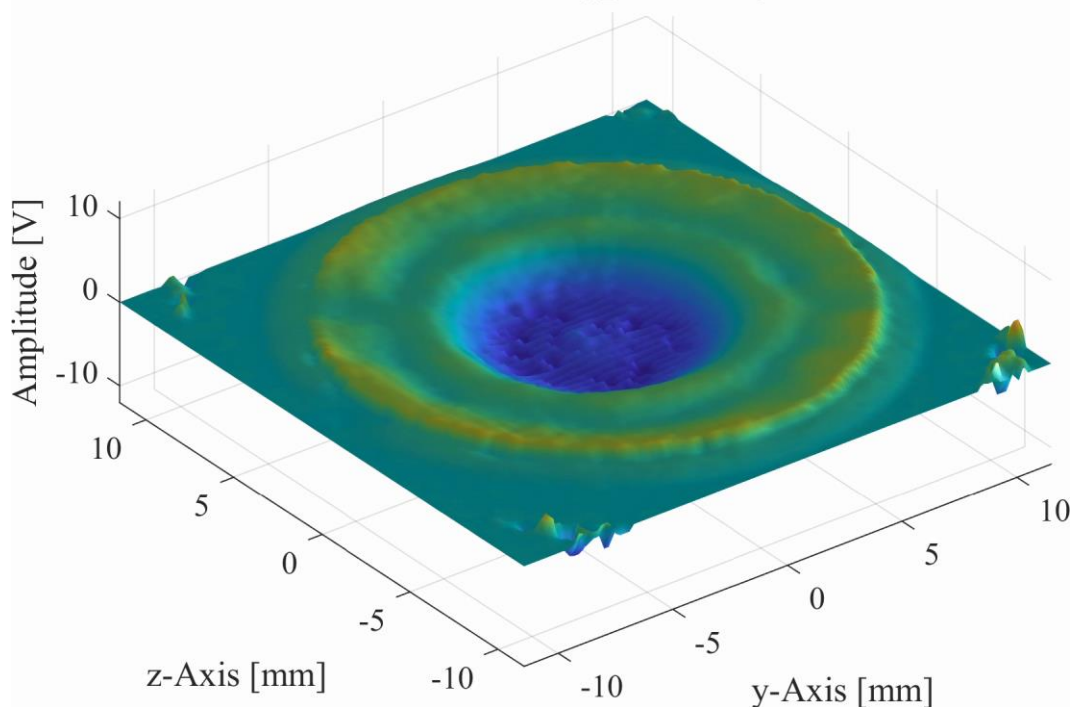
Figure 4.12: Selected frames of the surface scan (displacement data). Transducer: CF400-3E with excitation of outer ring only (100 V, 5 pulses).

The oscillation behavior when only the outer ring is excited is depicted in Figure 4.12. A pair of frames shows about a half-period ($1.25 \mu\text{s}$) of the mode shapes.

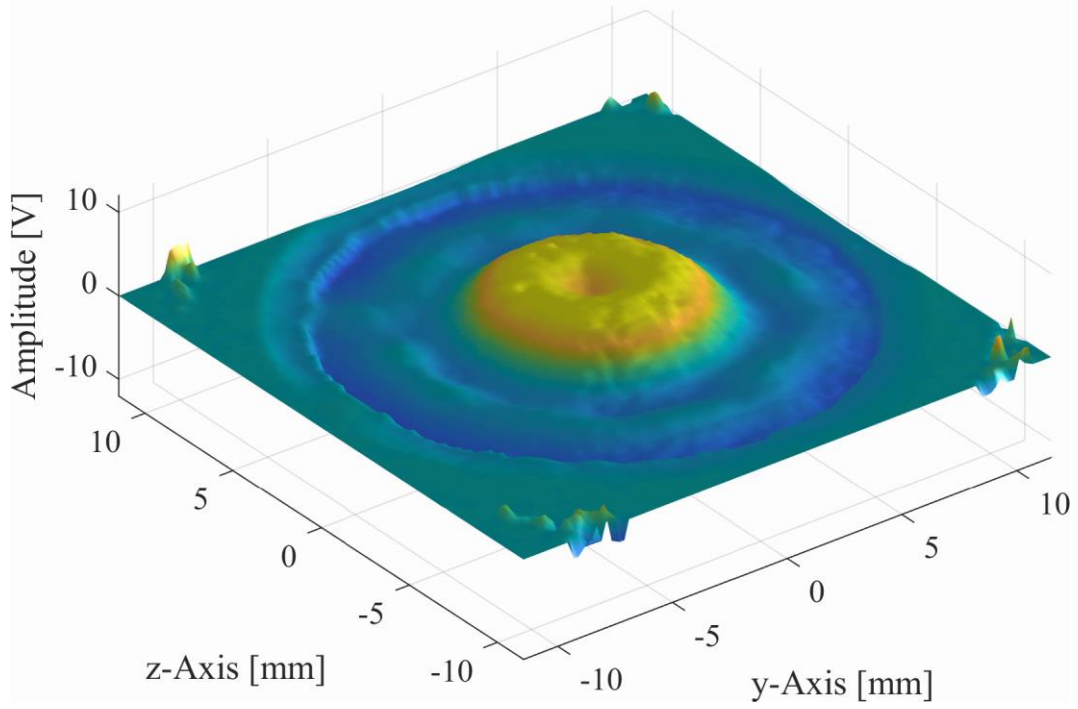
In the first pair, concentric rings are visible again, with a prominent nose-like shape in the center similar in size to the one observed in Figure 4.11. The images look remarkably similar to a higher order of the $(0, m)$ shapes presented in the theory section. It should be noted however that these are not mode shapes as the waves created by the outer ring are moving towards the center. The phase velocity of these waves is approximately 1400 m/s - 1900 m/s . The lower velocity is calculated with the excitation frequency and the wavelength measured in the data. The upper bound is obtained by measuring the phase velocity directly, analogously to the proceeding in section 4.1.1. With these values it is possible to calculate the travel time of the wave through the distance between the electrodes (1 mm). The resulting value is about 500 ns - 700 ns , which is in the order of the applied phase shift difference between the individual electrodes (Figure 4.13 and Section 4.3).

In the second pair of frames (3 and 4), a cross shape is clearly visible, which persists for over five vibration cycles. It is remarkable that the arms of the cross are so symmetric, to which no equivalent mode shapes exist. Therefore, it is hypothesized that this shape occurs due to a structural property of the transducer as this cross shape was also observed in the oscillation of the physically focused transducer. Furthermore, the frequency of this mode seems to match the excitation frequency as it occurs quite prominently. It should also be noted that the later oscillations starting at about $90 \mu\text{s}$ (not presented here) show again a standing wave as in the fourth frame of Figure 4.10 although with much lower amplitude.

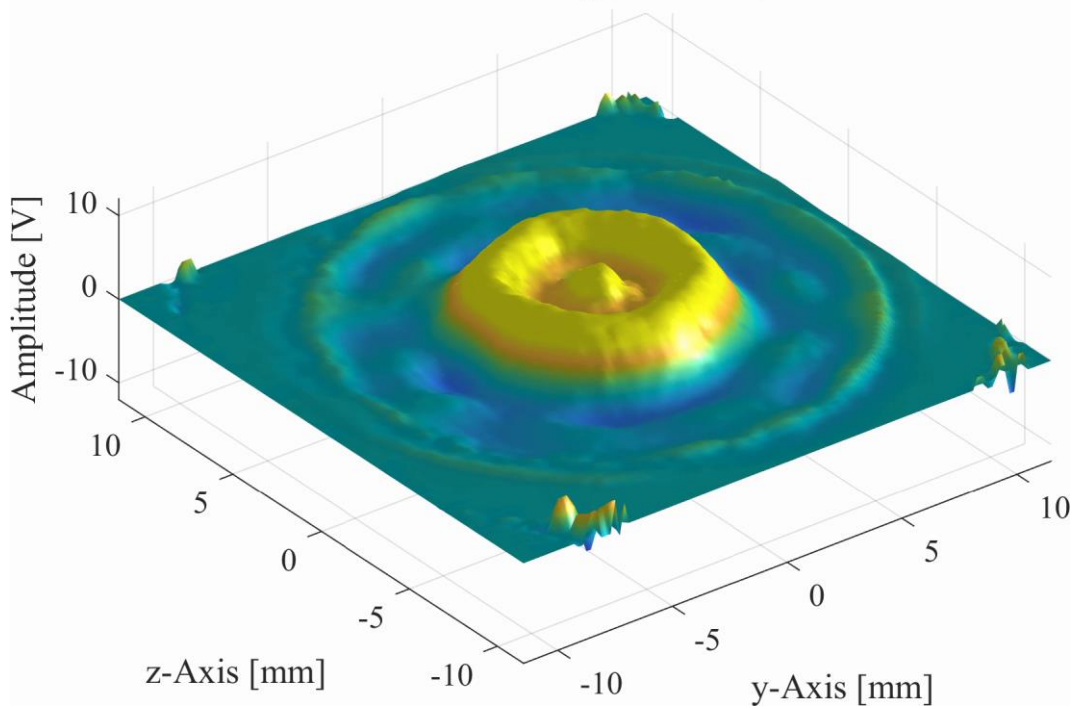
Time after trigger: $16.65 \mu\text{s}$



Time after trigger: 17.90 μs



Time after trigger: 25.00 μs



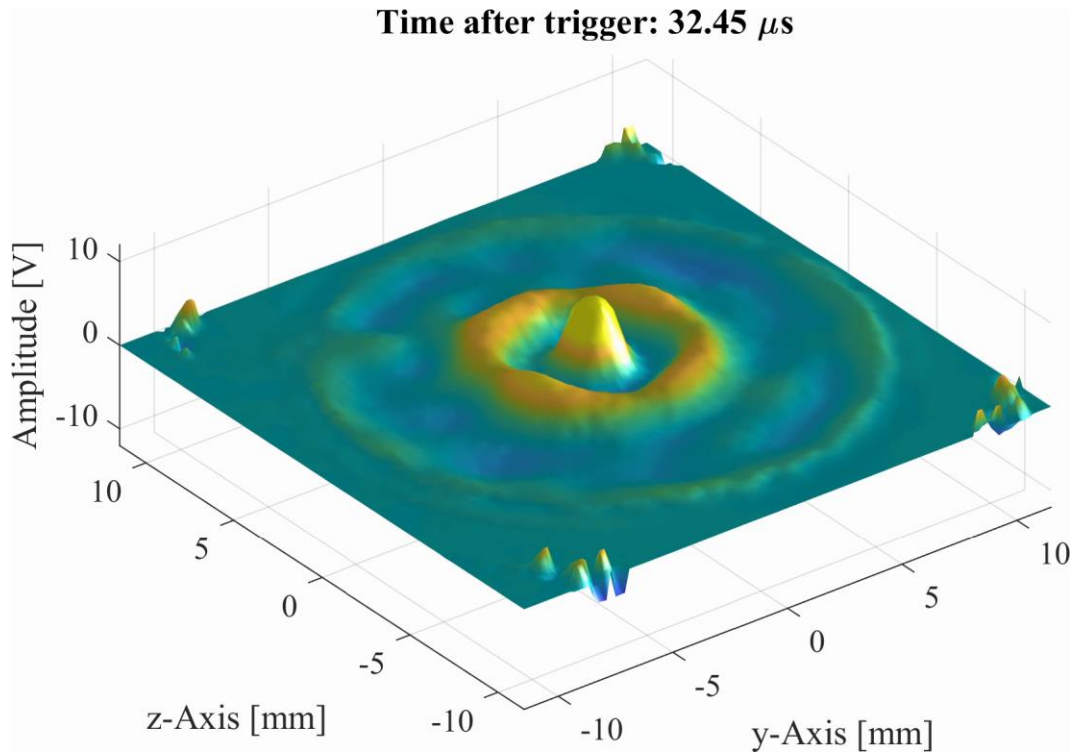


Figure 4.13: Selected frames of the surface scan (displacement data). Transducer: CF400-3E with phase shift 0-900-1800 ns (100 V, 5 pulses).

Figure 4.13 shows the oscillation of the transducer with a 0-900-1800 ns phase shift. The first frame shows the third excitation of the outer and middle ring, while the inner area is still recessed. In the second frame the situation half a period length later is visible, with the inner circle already having a larger amplitude at an earlier time than in the second frame of Figure 4.11. A small spot in the middle is still recessed, however. The third and fourth frames both show the prominent nose-like shape in the middle of the transducer and both have the same basic structure, but the deformation amplitude in the third frame is much higher. This oscillation shape explains the focusing behavior (shown in 4.3.2), as the kinetic energy is transferred from the outer rings to the inner circle and then oscillates at high amplitudes.

All configurations showed an oscillation pattern with long duration in the form of the (1,1) or (1,2) towards the end of their oscillation. This also appeared in the surface scans of the CF400, making it probable that it was caused by the “ringing” of the matching layer or the whole dynamic system.

A summary of the maximum amplitudes measured with the vibrometer is given in Table 4.5. The sensitivity settings of the LDV were constant for all presented configurations, it should be acknowledged however that to obtain the physical quantities from the measured voltages, only the given conversion factors were employed. No in-depth error analysis with the frequency-dependent sensitivity values given by the manufacturer was carried out.

Table 4.5: Maximum values of the measured displacement and velocity for various configurations. The physical quantities were calculated with the conversion factors 50 nm/V for displacement and 100 mm/s/V for velocity

Configuration	Displacement [V]	Displacement [nm]	Velocity [V]	Velocity [mm/s]
CF400, 10 V, 5 pulses	1.40	70	5.72	571.7
CF400, 100 V, 1 pulse	5.20	260	4.08	407.7
CF400, 100 V, 5 pulses	7.73	386,5	11.56	1156
CF400-3E, 100V, 5 pulses, outer ring	6.72	336	8.53	853.2
CF400-3E, 100V, 5 pulses, inner ring	9.71	485,5	11.24	1124
CF400-3E, 100V, 5 pulses, 0-900-1800 ns phase shift	10.77	538,5	11.50	1150

4.2.2 Power Distribution and Inhomogeneities

The relative power distribution was determined again as the square of the RMS level of the obtained signal at each point in space. The whole recorded signal with a length of 253 μ s was taken into account for the calculation.

CF400

Figure 4.14 shows the surface power distribution of the transducer CF400. The left image shows the measurement recorded with the usual orientation of the marker pointing upwards. A slight interlacing effect is observable in this image, due to some corrupt data in the last measured line. After the inhomogeneity was observed in the lower half of the power distribution a second measurement was done with the transducer rotated by 90° counter clockwise to evaluate whether it was caused by the relative orientation of LDV and the surface or the vibration itself. The resulting power distribution rotates correspondingly, showing that the inhomogeneity was caused by the surface vibration. Coincidentally, the marker was applied on the transducer such that the images recorded in normal orientation are nearly symmetric with respect to the z-axis. This also affects the transient sound fields, as discussed in 4.1.1, where the lower half had a higher amplitude and prolonged oscillation compared to the upper half.

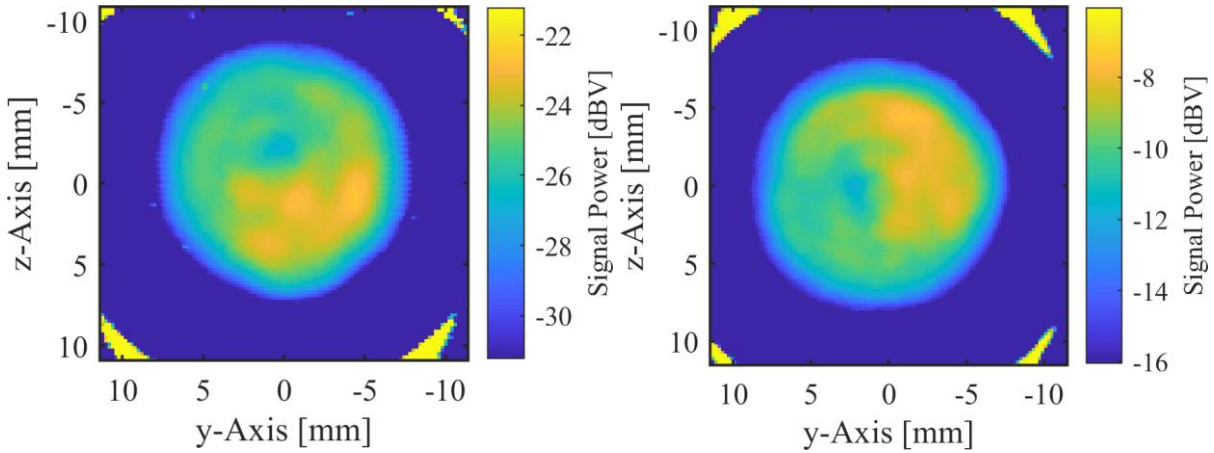


Figure 4.14: Surface scan power distribution (displacement data) of CF400 in usual orientation with 10 V, 5 pulse excitation (left) and rotated 90° counter clockwise with 100 V, 1 pulse excitation (right). Note the different signal power levels due to the different excitation settings.

There are numerous possible explanations for the observed behavior: It is known that the matching layer can cause so-called “ringing” due to its narrow band properties, where a sound pulse is prolonged when an eigenfrequency is excited. Another possibility is the inhomogeneous contact between transducer and backing material, causing some parts of the piezo element to be more damped than others. It has been shown that the transducer oscillation is significantly influenced by contact to other materials [Pohl et al. 2010]. This effect depends on the backing material and method of bonding however, which are both unknown at this point. The last possibility discussed here is partial depolarization. As the transducer was excited with a voltage higher than its maximum rated voltage [López Baos 2018], depolarization of the material likely occurred. Depending on the actual arrangement of the electric contacts, it is possible that the piezo composite was depolarized locally. However, as the images from the time-evolving surface scan reveal (Figure 4.10), this effect is barely observable in the forced vibration phase where the transducer receives the excitation voltage. Thus, this effect is subordinate to the other two.

Because of this asymmetry, the signal power received by the optical microphone depends on its position relative to the transducer. The SNR can be improved if the microphone is positioned over the transducer area with high output, i.e. over the lower half if the transducer is mounted in the usual orientation where the marker is on top.

CF400-3E

In Figure 4.15, images of the electronically focused transducer with two different excitation configurations are shown. The image with the phase shift 0-900-1800 ns according to [Mück 2018] shows that the oscillation is concentrated in a smaller circle than when only the inner electrode is excited. Consequently, the -6 dB radius is 4.0 mm for the left image and 4.5 mm for the right. The maximum power observed is 1 dB higher in the configuration with all rings excited than in the one where only the inner circle receives a signal. Thus, a focusing effect is

observable, especially considering that the higher amplitude oscillation of the left image is distributed over a larger area. This results in an increase in sound energy output.

There are two radial areas of higher power in the right image at 11 and two o'clock. They are part of the mode shape which is also slightly visible in the left image, but with different orientation: The more prominent arms are at half-past 12 and four o'clock. The cross-shaped mode in the center ring was discussed in the previous section (4.2.1).

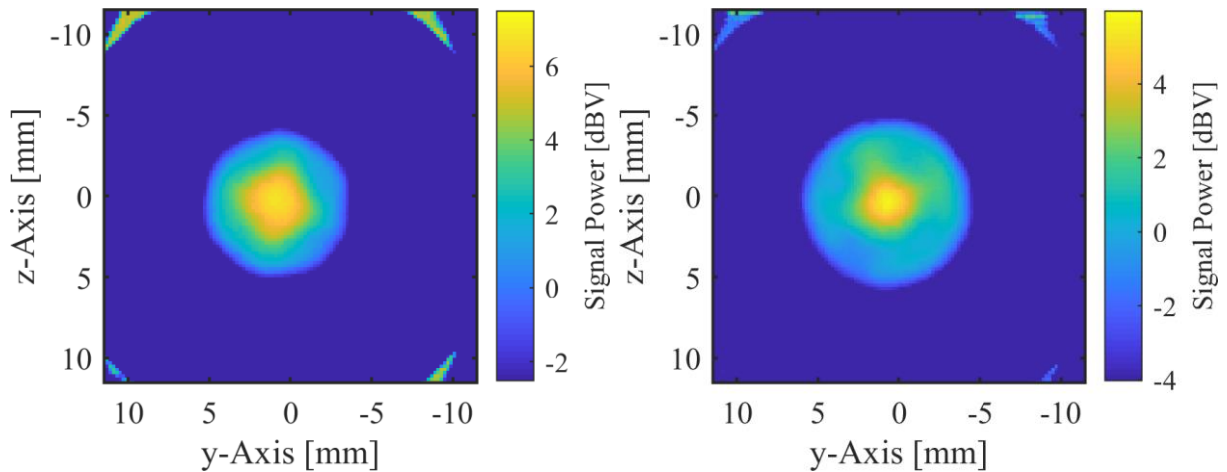


Figure 4.15: Surface scan power distribution (displacement data) of CF400-3E. Left: Excitation with phase shift 0-900-1800 ns, 100 V, 5 pulses. Right: Excitation of inner circle only, 100 V, 5 pulses

The power distribution image in Figure 4.16, where only the outer ring is excited, is qualitatively different to the previously introduced images. The whole transducer surface is visible, however there is no direct indication of the excited outer ring, to which the geometry is given in Figure 3.7. Instead, a ring of high amplitude with a radius of about 5.5 mm is observable, with very high amplitudes in the upper right quadrant but also some very low ones, the range being almost 6 dB. Two opposing areas where the sound power is low directly at the transducer border are visible at 10 and 5 o'clock. It is presumed that these areas stem from the voltage supply to the electrodes, which locally decreases the oscillation amplitude.

In the middle a small circle of with high amplitude is visible with a -6 dB radius of only 1.1 mm, the same radius as observed in the transient data. Surrounding it are some geometric shapes corresponding to the plate modes discussed in the previous section. It is remarkable that these shapes are visible so clearly even in this representation. The modes of the physically focused transducer could not be seen in the respective power distribution.

Comparing the surface power distributions of the two transducers further, one observes that the electronically focused transducer has much less pronounced inhomogeneities than the physically focused transducer. As both transducers are manufactured by the same company, it is probable that both use the same material as backing, piezo element and matching layer. Thus, it is likely that the cause of the inhomogeneous oscillation of the physically

focused transducer is due to the increased manufacturing difficulty of the curved piezo element.

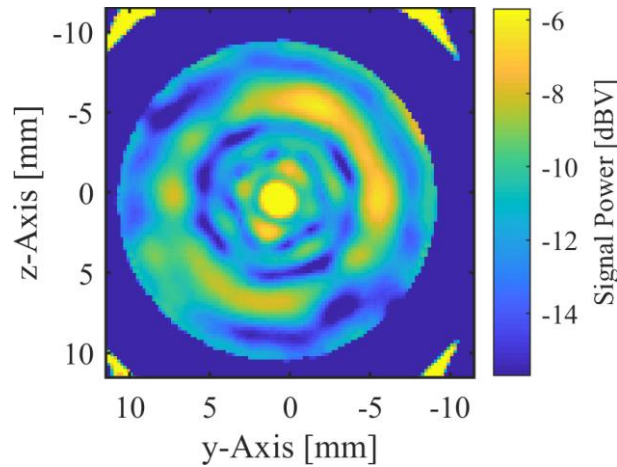


Figure 4.16: Surface scan power distribution (displacement data) of CF400-3E with excitation of the outer ring only, 100 V, 5 pulses.

4.3 Optimal Phase Shift for Electronically Focused Transducer

The electronically focused transducer requires special investigation, as there are more parameters to be determined than with the other transducers. As the research of [López Baos 2018] was inconclusive whether a clear focusing effect could be achieved, this section aims to give an answer to this question. In the first part calculations are made to determine an optimal phase shift between transducer rings through geometric considerations. The found configuration is then experimentally tested and compared to the phase shift suggested by the manufacturer [Mück 2018]. Finally, explanations are given as to why there is such a large discrepancy between both phase shift configurations and results. All electrodes may be referred to as “rings” in this section, although the innermost one is actually a circle.

4.3.1 Theoretical Calculation

The three separate electrodes applied to the electronically focused transducer (CF400-3E, depicted in Figure 3.7) can be excited with a configurable phase shift. To determine this phase shift, it was assumed that the sound waves should constructively interfere at a given distance from the surface of the transducer. This distance was chosen to 25 mm for the course of this calculation. The geometric setup is visible in Figure 4.17.

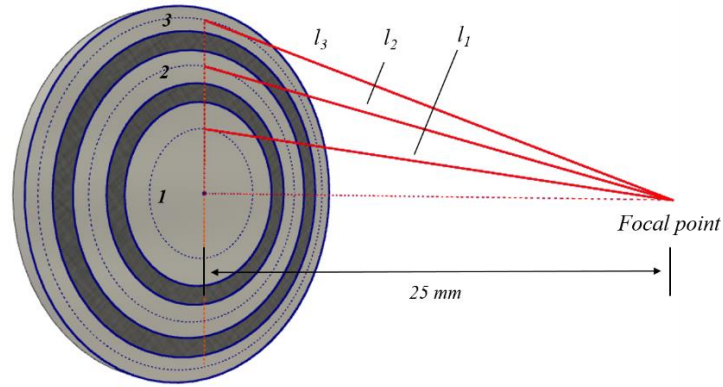


Figure 4.17: Visualization of the geometric setup for phase shift calculation.

It was further defined that the outer ring should have no phase shift since the sound wave will have the longest travel time from this ring to the focal point. With a speed of sound in air of $c \approx 343$ m/s under typical conditions (Table 2.1) the phase shift could be calculated along the transducer radius with

$$t_p = \frac{l_3 - d(r)}{c} \quad (4.1)$$

Here, l_3 is the distance from the point with no phase shift to the focal point, $d(r)$ is the distance of the point at radius r to the focal point. The resulting phase shift is denoted with t_p . A plot of phase shift against transducer radius can be seen in Figure 4.18.

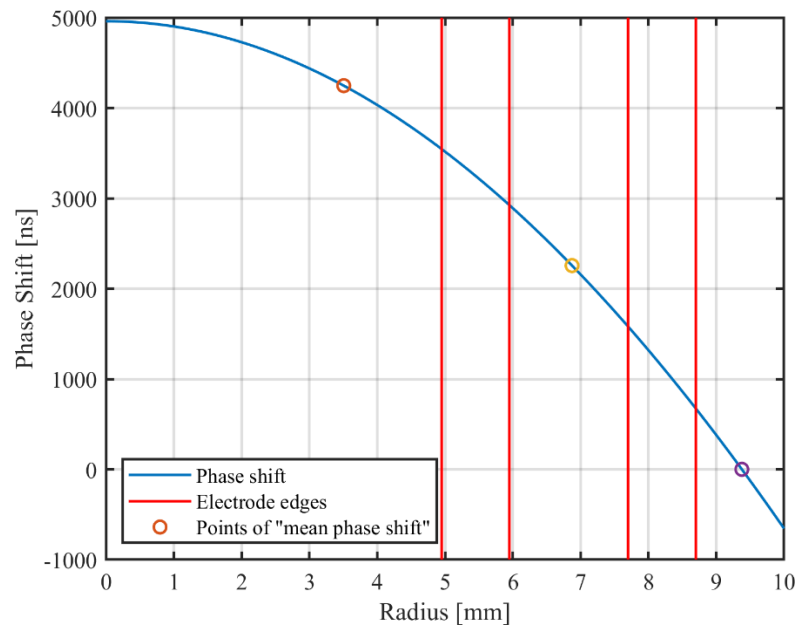


Figure 4.18: Calculated phase shift vs. transducer radius. The vertical lines mark the electrode edges, the round marker specify the points at which the phase shift was taken for each ring.

The phase shift follows a continuous curve over the radius. As the electrode has a certain width the required phase shift for inner and outer radius will differ considerably. Therefore, we decided to use the circle halving the surface area of the electrode as mean radius. This

results in the point of optimal phase shift not laying exactly in the middle of the inner and outer radius but rather a bit more outwards. The reason for this decision is the area-specific emission of sound, meaning that with said selection 50 % of the emitted sound energy will arrive “too late” at the focal point and 50 % will arrive “too early”. We considered this preferable to the alternative of taking the arithmetic mean of inner and outer radius.

For the specified values, the phase shifts are 0 ns, 2255 ns and 4246 ns for the third, second and first ring respectively (configuration 1). We decided against rounding these values to significant digits since the phase shift input of the amplifier is exact to one ns. These calculated phase shifts are very different compared to the ones given by *SONOTEC* of 0 ns, 900 ns, 1800 ns again from the outermost ring to the innermost one (configuration 2). In both phase shift configurations, the innermost ring has roughly double the phase shift of the middle ring.

4.3.2 Experimental Validation

The sound field measurements made to validate the calculated phase shifts had the same settings as all other sound fields described in section 4.1. The obtained sound field is visible in Figure 4.19. No focusing effect can be observed, on the contrary the sound field seems to diverge from the beginning, without a visible near field. However, there are clear interference effects occurring in the sound field, the most prominent one being in the area of $y = 20$ mm to $y = 45$ mm centered around $z = 0$ mm. This is the area in which the interference should appear according to the calculations, considering the width of the electrodes. It becomes apparent from the sound field that this is not the only place at which constructive interferences occur.

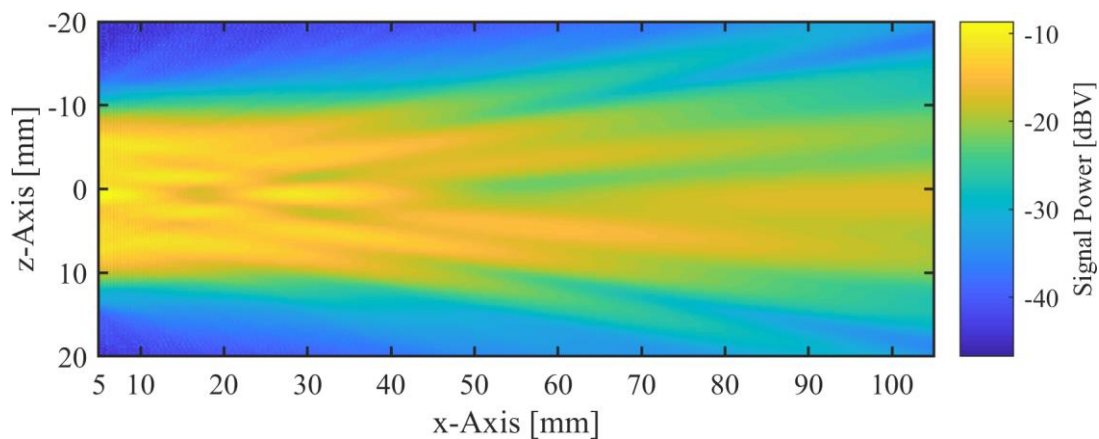


Figure 4.19 Power distribution of CF400-3E with phase shift 0-2255-4246 ns. The desired focusing effect does not occur, instead rather prominent grating lobes are present.

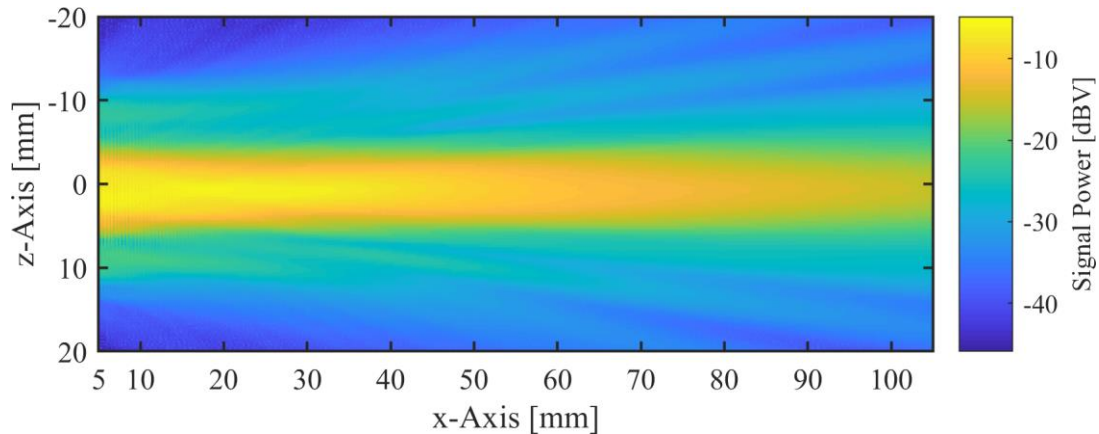


Figure 4.20: Power distribution of CF400-3E with phase shift 0-900-1800 ns. The beam with high intensity is narrow compared with the other phase shift configuration.

Comparing Figure 4.19 to Figure 4.20, which was obtained by applying the phase shifts given by *SONOTEC*, significant differences are visible in the diameter of the sound beam. While the diameter in configuration 1 is never lower than 17 mm, it reaches as low as 6 mm in configuration 2 when applying a -6 dB threshold. The diameter for configuration 2 is higher than the one given by [Mück & Scheunemann 2018], and it is not quite as low as the beam width of the physically focused CF400.

The center focusing area of configuration 1 is from $x = 20$ mm to $x = 40$ mm and symmetric about the central axis. However, its peak value is 5 dB lower than the maximum in configuration 2, where the focus area is centered around $x = 20$ mm.

Comparing the results to the sound fields of [Steinhausen et al. 2016a] again an increased sensitivity and resolution can be observed. In the mentioned work, sound field measurements were carried out on an earlier version of the electronically focused transducer. They were conducted both with a LDV and by means of a small spherical reflector sending the sound waves to another ACU transducer outside the sound field.

From observing Figure 4.20 and comparing it to Figure 4.19 it can be concluded that the phase shift pattern as calculated is not the cause for the focusing behavior of the 0-900-1800 ns phase shift. This can already be predicted from the pitch of the electrodes, which at ten times the size of the wavelength is too large to permit focusing through interference in air. Thus, the focal law introduced by the manufacturer relies on the interference of surface waves instead, which have been observed in the surface scan of this transducer (Figure 4.12 and Figure 4.13). The middle and inner ring should therefore be excited exactly at the time when the wave coming from the outer ring travels over them. With the phase velocity of the surface waves according to 4.2.1, the time difference of the electrodes was calculated to 500-700 ns which is in the order of the phase shift given by the manufacturer. López Baos (2018) also observed a focusing behavior for 0-400-800 ns and 0-800-1600 ns phase shifts between the electrodes, although his data should perhaps be re-analyzed to reach full comparability due to

the different evaluation methods. No publications could be found that investigated an electronically focused transducer with large pitch such as the present one. There exist however some papers on phased arrays with zero grating lobes, where the pitch is smaller than half a wave length [A. Jäger et al. 2017, E. Konetzke et al. 2015, Montero de Espinosa et al. 2004]. One of the works [Montero de Espinosa et al. 2004] presents a linear phased-array transducer operating at 800 kHz used to inspect paper by lamb-wave generation. No sound pressure levels were given in the work; therefore, it cannot be determined if the transducer is suitable for through transmission testing. The transducers presented in the other two works are not designed for testing of materials and thus either do not emit large sound powers or do so in an unfocused way. None of the found works reported a focusing behavior that relies on surface waves.

With the chosen phase shift configuration (0-900-1800 ns), surface waves interfere in the middle part of the transducer, which results in it oscillating much higher than when it is excited solely. This effectively creates a transducer with smaller active radius and with higher oscillation amplitude than would be possible with the given excitation voltage. It was hypothesized that the higher oscillation amplitude could lead to depolarization due to the direct piezoelectric effect. However, as voltage measurements of the transducer during excitation revealed, no significant voltage increase is visible due to the focusing.

Additional images showing the surface oscillation with 0-900-1800 ns phase shift and the time-evolving sound field for 0-2255-4246 ns as well as 0-900-1800 ns can be found in Appendix D.

5 Conclusion

In this work, various transducers were investigated and characterized regarding their oscillation behavior and resulting sound fields. To obtain the desired quantities, measurements were conducted with a laser-doppler vibrometer and a novel optical microphone. The laser doppler vibrometer recorded the transducer surface oscillation and the optical microphone the transient sound field. Both methods increased resolution and sensitivity of the results compared to older works. The two physically focused transducers investigated were additionally measured with a confocal scanning microscope to obtain their spherical radius and predict the focal length.

The software for data processing was optimized and restructured for ease of use with multiple measurements, accelerating the visualization process. Two different methods of data representation were chosen for this work, one creates transient videos of the volume-scan data, the other visualizes the received signal power in one image. Both methods were applied to each measurement type, as they highlight different information aspects of the data. Numerous other methods have been tested and realized, such as side-by-side visualization of a transducer surface cross section and the corresponding sound field. As these methods rely on a digital screen, they were not included in this document form.

From the obtained data, the phase velocity of the sound waves was calculated, and the dispersive behavior observed through the difference in phase velocity. The occurring echoes were classified according to their virtual wavelength and their origin (the optical microphone itself) was identified. Focusing effects could be clearly seen in the sound fields of the physically focused transducers and in the data presented for the power distribution. More prominent side lobes were present for the transducer with lower focal length (ULT200). Different damping behaviors of the transducers were visible in the transient visualization of the data, from which the use of different backing materials could be concluded. Furthermore, an asymmetric oscillation was observed for the CF400 transducer in both the sound field and surface scan measurements. This behavior can be caused by inhomogeneous backing, oscillation of the matching layer (“ringing”), depolarization or a mixture of all the mentioned effects. As this behavior is documented now, for further tests with plates the optical microphone can be positioned relative to the lower half of the transducer and not its center to increase the received signal power. Comparing the characteristics (near field distance, -6 dB beam radius, opening angle) of all investigated transducers, large differences between theory and experimental results were observed and related to missing standards in ACU transducer characterization.

Laser doppler vibrometer measurements revealed some mode shapes of the CF400 and CF400-3E transducers, however a stationary excitation with a single frequency is needed to

produce a high-amplitude mode shape. The individual excitation of the electronically focused transducer's electrodes revealed traveling surface waves. A separate investigation was made to determine the optimal phase shift of the electronically focused transducer. The experiments showed that this transducer does not operate under the conventional phased-array principles as expected, but rather utilizes mode excitation to increase amplitude and achieve its focusing effect.

As for possible subsequent research, several possibilities can be given:

- The repaired optical microphone ETA 450 Ultra, which arrived just after measurements for this work were completed, could be calibrated with known sources and compared to the ETA 250 Ultra used in this work. This is necessary to give quantitative results of the measured SPL and its dependency on the frequency.
- With the new microphone, testing on plates can resume. It is for example possible to mount the microphone to the robot arm available in the laboratory and conduct tests on a curved surface.
- Another option is to test different measurement configurations, as the optical microphone is in principle well suited for one-sided inspection. Pulse-echo and Pitch-Catch [Guruschkin 2015] configurations, along with the reception of lamb-waves [Rohringer et al. 2018] have been tested. The pulse-echo configuration is especially promising in combination with a broadband transducer, such as a thermo-acoustic or ferroelectret transducer, as short pulses are possible which could give depth-information of the defects.
- A novel measurement configuration which has yet to be tested with the newest version of the optical microphone is the two-receiver configuration [Steinhausen et al. 2016b], where two receivers are positioned at equal distances from the source in a one-sided configuration. The signals of the two receivers are subtracted, making this a promising application for the optical microphone as no resonance frequency is to be expected and the frequency behavior of different microphones should be nearly identical. Tests with the earlier versions of the optical microphone did not yield results due to the lower sensitivity [Steinhausen 2019].
- Based on the present work, simulations will be carried out to compare analytical and numerical models with real measurements. The data obtained with the LDV can be taken as input, and the simulation output then be compared to the sound field measurements. This should give further insight into what effects each part of the transducer has on the oscillation behavior, and explain the large differences observed when comparing calculated and measured quantities of a sound field. A complete simulation of the oscillation would also be possible; however, the geometric and material properties of the simulated transducer would have to be known.

- The present work furthermore can be used as a basis for the optimization and further development of ACU transducers. The electronically focused transducer could be subject to other investigations now that the focusing mechanism is known.

Literature

- A. Jäger, D. Großkurth, M. Rutsch, A. Unger, R. Golinske, H. Wang, ... M. Kupnik. (2017). Air-coupled 40-KHZ ultrasonic 2D-phased array based on a 3D-printed waveguide structure. In *2017 IEEE International Ultrasonics Symposium (IUS)* (pp. 1–4). <https://doi.org/10.1109/ULTSYM.2017.8091892>
- Alexandrov, O. (2008). *Illustration of vibrations of a drum*. [Matlab].
- Álvarez, F. J., & Kuc, R. (2008). Dispersion relation for air via Kramers-Kronig analysis. *The Journal of the Acoustical Society of America*, *124*(2), p. EL57–EL61. <https://doi.org/10.1121/1.2947631>
- Alvarez-Arenas, T. E. G. (2004). Acoustic impedance matching of piezoelectric transducers to the air. *IEEE Transactions on Ultrasonics, Ferroelectrics and Frequency Control*, *51*(5), p. 624–633. <https://doi.org/10.1109/TUFFC.2004.1320834>
- Böttcher, C. J. F., Belle, O. C. van, & Böttcher, C. J. F. (1973). *Dielectrics in static fields* (2d ed. completely rev). Elsevier Scientific Pub. Co, Amsterdam, New York.
- Ciddor, P. E. (1996). Refractive index of air: new equations for the visible and near infrared. *Applied Optics*, *35*(9), p. 1566. <https://doi.org/10.1364/AO.35.001566>
- Cristalli, C., Torcianti, B., & Vass, J. (2006). *A new method for filtering speckle noise in vibration signals measured by Laser Doppler Vibrometry for on-line quality control*. - art. no. 63450Y (Vol. 6345). <https://doi.org/10.1117/12.693104>
- Deutsch, V., Platte, M., & Vogt, M. (1997). *Ultraschallprüfung*. Springer Berlin Heidelberg, Berlin, Heidelberg. <https://doi.org/10.1007/978-3-642-59138-9>
- E. Konetzke, M. Rutsch, M. Hoffmann, A. Unger, R. Golinske, D. Killat, ... M. Kupnik. (2015). Phased array transducer for emitting 40-kHz air-coupled ultrasound without grating lobes. In *2015 IEEE International Ultrasonics Symposium (IUS)* (pp. 1–4). <https://doi.org/10.1109/ULTSYM.2015.0019>
- Edlén, B. (1966). The Refractive Index of Air. *Metrologia*, *2*(2), p. 71–80. <https://doi.org/10.1088/0026-1394/2/2/002>
- Fischer, B. (2016). Optical microphone hears ultrasound. *Nature Photonics*, *10*, p. 356.
- Fischer, B., Reining, F., & Wintner, E. (2015). *US 2015/0139451 A1*. Vienna.
- Gamper, J. (2017). *Entwicklung eines neuen Messkonzepts zur luftgekoppelten Ultraschallprüfung von Faserverbundwerkstoffen* (Master Thesis). Technische Universität München, München.
- Grager, J.-C. (2014). *Quantitative Impact- und Porositätscharakterisierung an CFK-Werkstoffen mittels zerstörungsfreier Prüfmethoden* (Master Thesis). Technische Universität München, München.
- Gronauer, M., & Fricke, J. (1986). *Acoustic Properties of Microporous SiO₂-Aerogel* (Vol. 59).
- Guruschkin, E. (2015). *Berührungslose Prüfung von Faserverbundwerkstoffen mit Luftultraschall* (Master Thesis). Technische Universität München, München.
- Hirsh, I. J. (1952). *The measurement of hearing*. McGraw-Hill, New York, NY, US.

- Huang, C.-H., Lin, Y.-C., & Ma, C. C. (2004). Theoretical analysis and experimental measurement for resonant vibration of piezoceramic circular plates. *IEEE Transactions on Ultrasonics, Ferroelectrics and Frequency Control*, 51(1), p. 12–24. <https://doi.org/10.1109/TUFFC.2004.1268463>
- Ing. Büro Dr. Hillger. (2018). Datenblatt Airtech Prüfköpfe. Ing. Büro Dr. Hillger. Retrieved from <http://www.dr-hillger.de/PDF/Pruefkoepfe.pdf>
- isel Germany AG. (n.d.). Techn. & Bestellanlagen, Masszeichnungen Flachbetteinheiten FB 2. Retrieved from <https://www.isel.com/de/mwdownloads/download/link/id/9152/>
- Jenderka, K.-V., Steinhausen, R., Kopp, A., Pientschke, C., & Kiel, M. (2015). Möglichkeiten zur räumlichen und zeitlichen charakterisierung von Ultraschallfeldern in Luft mit scannender Laser-Doppler-Vibrometrie. In *Fortschritte der Akustik - DAGA 2015* (Vol. 41, p. 8). Nürnberg.
- Klaas Bente, Daniel Kotschate, Saskia Wendland, & Mate Gaal. (2018). The thermoacoustic effect and its application in air-coupled testing of composite structures. In *10th International Symposium on NDT in Aerospace* (p. 8). Dresden.
- KL/TBE. (2014, January 9). TranAX 3 Messdaten-Erfassung und Analyse. Elsys AG.
- Krautkrämer, J., & Krautkrämer, H. (1990). *Ultrasonic Testing of Materials*. Springer Berlin Heidelberg, Berlin, Heidelberg. <https://doi.org/10.1007/978-3-662-10680-8>
- Kuttruff, H. (1988). *Physik und Technik des Ultraschalls*. Hirzel, Stuttgart.
- Lahrz, T., Bischof, W., & Sagunski, H. (2008). Gesundheitliche Bewertung von Kohlendioxid in der Innenraumluft: Mitteilungen der Ad-hoc-Arbeitsgruppe Innenraumrichtwerte der Innenraumlufthygiene-Kommission des Umweltbundesamtes und der Obersten Landesgesundheitsbehörden. *Bundesgesundheitsblatt - Gesundheitsforschung - Gesundheitsschutz*, 51(11), p. 1358–1369. <https://doi.org/10.1007/s00103-008-0707-2>
- Lenz, M., Gust, N., Wolf, M., Kühnicke, E., & Rodig, T. (2013). Transducer characterization by sound field measurements. *IEEE Transactions on Ultrasonics, Ferroelectrics and Frequency Control*, 60(5), p. 998–1009. <https://doi.org/10.1109/TUFFC.2013.2658>
- Lerch, R., Sessler, G., & Wolf, D. (2009). *Technische Akustik*. Springer Berlin Heidelberg, Berlin, Heidelberg. <https://doi.org/10.1007/978-3-540-49833-9>
- López Baos, A. (2018). *Laser-based air-coupled ultrasonic testing of CFRP plates* (Masterarbeit). Technische Universität München, München.
- Martarelli, M., & Ewins, D. J. (2006). Continuous scanning laser Doppler vibrometry and speckle noise occurrence. *Mechanical Systems and Signal Processing*, 20(8), p. 2277–2289. <https://doi.org/10.1016/j.ymssp.2005.06.003>
- Montero de Espinosa, F., Chávez, J. A., Yañez, Y., Salazar, J., Turó, A., Chinchurreta, F. J., & García-Hernandez, M. (2004). AIR-COUPLED PIEZOELECTRIC ARRAY TRANSDUCERS FOR NDT APPLICATIONS. In *16th WCNDT 2004* (Vol. 16, p. 6). Montreal, Canada.
- Mück, A. (2018). Phased array probes for non-contact ultrasonic testing. In *ECNDT 2018* (Vol. 12, p. 348). SONOTEC Ultraschallsensorik Halle GmbH, Gothenburg. Retrieved from <http://www.ndt.net/?id=22861>
- Mück, A., & Scheunemann, S. (2018). Phased-Array-Prüfköpfe für die koppelmittelfreie Ultraschallprüfung, p. 7.

- Owens, J. C. (1967). Optical Refractive Index of Air: Dependence on Pressure, Temperature and Composition. *Applied Optics*, 6(1), p. 51. <https://doi.org/10.1364/AO.6.000051>
- Panda, P. K. (2017). Piezoceramic Materials and Devices for Aerospace Applications. In N. E. Prasad & R. J. H. Wanhill (Eds.), *Aerospace Materials and Material Technologies* (pp. 501–518). Springer Singapore, Singapore. https://doi.org/10.1007/978-981-10-2134-3_23
- Peck, E. R., & Reeder, K. (1972). Dispersion of Air*. *Journal of the Optical Society of America*, 62(8), p. 958. <https://doi.org/10.1364/JOSA.62.000958>
- Pohl, J., Mook, G., Lammering, R., Ende, S. von, & Tomasini, E. P. (2010). Laser-vibrometric measurement of oscillating piezoelectric actuators and of Lamb waves in CFRP plates for structural health monitoring (pp. 65–72). Presented at the 9TH INTERNATIONAL CONFERENCE ON VIBRATION MEASUREMENTS BY LASER AND NON-CONTACT TECHNIQUES AND SHORT COURSE, Ancona (Italy). <https://doi.org/10.1063/1.3455490>
- Pohl, J., Willberg, C., Gabbert, U., & Mook, G. (2012). Experimental and Theoretical Analysis of Lamb Wave Generation by Piezoceramic Actuators for Structural Health Monitoring. *Experimental Mechanics*, 52(4), p. 429–438. <https://doi.org/10.1007/s11340-011-9503-2>
- Polytec GmbH. (2006). Nature & Technology: Vibrations Everywhere! Advancing Measurements, p. 1.
- Rembe, C., & Dräbenstedt, A. (2015). D1.1 - Speckle-Insensitive Laser-Doppler Vibrometry with Adaptive Optics and Signal Diversity. *AMA Service GmbH, P.O. Box 2352, 31506 Wunstorf, Germany*. <https://doi.org/10.5162/sensor2015/d1.1>
- Rogovsky, A. J. (1991). Development and Application of Air-Coupled Ultrasonic Dry-Contact and Air-Coupled C-Scan Systems for Nondestructive Evaluation of Aerospace Composites. *Matl. Eval.*, 50(12), p. 1401–1497.
- Rohringer, W., Heine, T., Sommerhuber, R., Lehmann, N., & Fischer, B. (2018). Optical Microphone as Laser-Ultrasound Detector. Presented at the DAGA 2018, München.
- SONOTEC Ultraschallsensorik Halle GmbH. (2018, November 4). Katalog Prüfköpfe für die zerstörungsfreie Prüfung. SONOTEC Ultraschallsensorik Halle GmbH. Retrieved from https://www.sonotec.de/fileadmin/media/DE/Produkte/Zerstoerungsfreie_Material_Pruefung/KAT_Pruefkoepfe_ZfP_SONOTEC_dt_Rev_4.0_2018-04-11_Online_Version.pdf
- Steinhausen, R. (2019, January). *Luftultraschallprüfung: Von den Grundlagen bis zur Anwendung an diversen Materialien und Bauteilen*. Presented at the 313. Sitzung des Arbeitskreises, Ismaning.
- Steinhausen, R., Kiel, M., Pientschke, C., Hahn, K., Höhndorf, T., & Heuert, U. (2016a). Elektronisch fokussierbare Wandler für die Luftultraschallprüfung (p. 8). Presented at the DACH Jahrestagung, DGZFP, Salzburg. Retrieved from www.ndt.net/?id=18974
- Steinhausen, R., Kiel, M., Pientschke, C., Muench, H.-J., Mueck, A., & Hahn, K. (2016b). New approaches to air-coupled ultrasound testing of composite lightweight materials. (Vol. 19). Presented at the World Conference on Non-destructive Testing 2016, Munich.

- Stößel, R. (2004, February 19). Air-coupled ultrasound inspection as a new non-destructive testing tool for quality assurance. Universität Stuttgart. <https://doi.org/10.18419/opus-1625>
- The Ultran Group. (2018, January 10). Ultrasonic Transducers. Retrieved from <http://ultrangroup.com/wp-content/uploads/transducer-catalog.pdf>
- Tufoi, M., Gillich, G.-R., Praisach, Z.-I., Ntakpe, J. L., & Hatiegan, C. (2014). *An Analysis of the Dynamic Behavior of Circular Plates from a Damage Detection Perspective* (Vol. 11).
- Xarion Laser Acoustics GmbH. (2017, February). Datasheet Eta250 Ultra. Xarion Laser Acoustics. Retrieved from <http://xarion.com/products/eta250-ultra>
- Zhang, Y., Wang, L., & Qin, L. (2018). Equivalent parameter model of 1-3 piezocomposite with a sandwich polymer. *Results in Physics*, 9, p. 1256–1261. <https://doi.org/10.1016/j.rinp.2018.04.046>

List of figures

Figure 2.1 : Wave types. Upper part: Longitudinal wave, lower part: Transversal wave.	4
Figure 2.2 : Schematic of sound waves at an interface.	6
Figure 2.3 : Schematic of a plate made from piezo-composite material.....	10
Figure 2.4 : Structure of an ACU-transducer. Augmented representation following [Gamper 2017].....	10
Figure 2.5 : Schematic of the sound field emitted from a plane transducer and sound pressure distribution along the central axis. Graphic following [Krautkrämer & Krautkrämer 1990].....	12
Figure 2.6 : Selected vibration modes of an ideal circular membrane. The first index gives the number of nodal axes, the second the number of nodal rings (including the circumference). Recreated from [Alexandrov 2008]	14
Figure 2.7 : Internal structure of the optical microphone. Translated from [Guruschkin 2015].....	16
Figure 2.8 : Airy-function for the etalon of the optical microphone. [US 2015/0139451 A1 2015].....	17
Figure 2.9 : Functioning principle of the laser-doppler vibrometer. Image courtesy of [Polytec GmbH 2006].....	19
Figure 3.1 : Schematic of the components in the measurement setup and their connection. The arrows of the dashed lines indicate where the measurement point is.	21
Figure 3.2 : Right: Granty Table System – FB2 by ISEL with visualization of the transducer (not to scale) and coordinate axes (blue) [isel Germany AG n.d.]. The applied marker for transducer orientation is indicated in orange.	22
Figure 3.3 : Voltage Peaks from signal Amplifier. Top: schematic drawing with high damping (but still not ideal), V_e is the set voltage. Bottom: actual oscilloscope output with connected transducer.	23
Figure 3.4 : From left to right: <i>SONOTEC</i> CF400 3E & CF400 (with markers), <i>The Ultran Group</i> ULT200, <i>Ingenieurbüro Dr. Hillger</i> AT200 & AT75.....	24
Figure 3.5 : Profile lines of the two physically focused transducers measured with CLSM (5x magnification) and result of the fitting algorithm. Left: CF400 with radius $R=73.3$ mm, right: ULT200 with radius $R=45.4$ mm.....	26
Figure 3.6 : 3D surface of transducer CF400 measured with CLSM (20x magnification). The height of the vesicles is about 80-90 μm	27
Figure 3.7 : Left: Piezo composite transducer SONOSCAN CF400 3E (image by [Mück & Scheunemann 2018], licensed under CC 4.0) with three separate silver electrodes. Right: Schematic of phase shift and focusing effect.	28
Figure 3.8 : Spatial relation of transducer, measurement device (optical microphone or laser-doppler vibrometer) and scanning directions with coordinate system.	32
Figure 3.9 : Photo of the arrangement for measurements with the laser-doppler vibrometer ..	32

Figure 3.10 : Photo of the optical microphone (with large deviation from vertical alignment) in front of the transducer. The yellow fiber optic cable is visible in the background.	32
Figure 3.11 : Visualization of the A-Scan and B-Scan representations. Row and Line direction represent the moving directions of the scanning device. Augmented representation following [Grager 2014]	35
Figure 3.12 : Visualization of the volume-scan and the extraction of C-Scans as video-frames at different time instances. The axes are the same as in Figure 3.11.....	37
Figure 3.13 : Transducer surface with speckle noise (left) and with smoothed-out speckle noise (right). The two images were taken from measurements with the same configuration.	39
Figure 3.14 : Data flow for the TRANAX oscilloscope, which was used for all measurements in this work. The .bdf files are created when measuring in Single- or Multichannel ECR-mode	39
Figure 3.15 : Overview of the signal flow in the measurement setup (in downwards direction). The left column contains the device or medium in which the signal travels, in the right column some disturbances are given. The rows of the measurement device are split, since optical microphone and vibrometer were used interchangeably at this point. The colors reference the input signal type of the respective device. Augmented representation following Gamper (2017).....	41
Figure 4.1 : Extracted frames of the sound field time-evolution. Transducer: CF400. The title of each frame includes a timestamp indicating the time since the trigger signal (rising edge). The axes indicate the respective distance to the center of the transducer surface.....	46
Figure 4.2 : Frame of the time-evolving sound field with drastically reduced colormap limits. Echoes up to the fourth order are visible (marked) and their wavelengths are distinguishable. An oscillation with lower frequency and amplitude is also observable. The same plotting conventions as in Figure 4.1 apply.	49
Figure 4.3 : Extracted frames of the sound field time-evolution. Transducer: ULT200. The same plotting conventions as in Figure 4.1 apply.	50
Figure 4.4 : Frame of the time-evolving sound field of the ULT200 transducer with drastically reduced colormap limits. Interference patterns are visible in the middle and echoes with different propagation directions are observable. The method of determining the wavelength is visualized in orange. Here, $i \in \mathbb{N}$ The same plotting conventions as in Figure 4.1 apply.	51
Figure 4.5 Power distribution of transducer CF400 (physically focused). Settings: 100 V, 5 pulses, 0 dB gain.	53
Figure 4.6 : Power distribution of transducer ULT200 (physically focused). Prominent side lobes are visible. Settings: 100 V, 5 pulses, 0 dB gain.....	54

Figure 4.7 : Power distribution of transducer AT200 (planar). As the trigger setting was incorrect for this measurement, the first 15 mm on the x-Axis are defined by the echo. Settings: 100 V, 5 pulses, -12 dB gain.	54
Figure 4.8 : Power distribution of transducer AT75. The measurement area is not large enough to fully depict the sound field. Settings: 100 V, 5 pulses, -12 dB gain.	55
Figure 4.9 : Visualization used to determine the opening angle with modified colormap. Transducer: ULT200. Orange lines: measured (full) and calculated (dashed) opening angles (rounded to full degrees). An asymmetry in the divergence angle is visible.	57
Figure 4.10 : Selected frames of the surface scan (velocity data). Transducer: CF400 with 100 V and 1 pulse excitation, rotated 90° counter clockwise.	59
Figure 4.11 : Selected frames of the surface scan (displacement data). Transducer: CF400-3E with excitation of inner circle only (100 V, 5 pulses). Note the small time difference between the frames.	61
Figure 4.12 : Selected frames of the surface scan (displacement data). Transducer: CF400-3E with excitation of outer ring only (100 V, 5 pulses).	63
Figure 4.13 : Selected frames of the surface scan (displacement data). Transducer: CF400-3E with phase shift 0-900-1800 ns (100 V, 5 pulses).	66
Figure 4.14 : Surface scan power distribution (displacement data) of CF400 in usual orientation with 10 V, 5 pulse excitation (left) and rotated 90° counter clockwise with 100 V, 1 pulse excitation (right). Note the different signal power levels due to the different excitation settings.	68
Figure 4.15 : Surface scan power distribution (displacement data) of CF400-3E. Left: Excitation with phase shift 0-900-1800 ns, 100 V, 5 pulses. Right: Excitation of inner circle only, 100 V, 5 pulses	69
Figure 4.16 : Surface scan power distribution (displacement data) of CF400-3E with excitation of the outer ring only, 100 V, 5 pulses.	70
Figure 4.17 : Visualization of the geometric setup for phase shift calculation.	71
Figure 4.18 : Calculated phase shift vs. transducer radius. The vertical lines mark the electrode edges, the round marker specify the points at which the phase shift was taken for each ring.	71
Figure 4.19 Power distribution of CF400-3E with phase shift 0-2255-4246 ns. The desired focusing effect does not occur, instead rather prominent grating lobes are present.	72
Figure 4.20 : Power distribution of CF400-3E with phase shift 0-900-1800 ns. The beam with high intensity is narrow compared with the other phase shift configuration.	73

List of tables

Table 2.1: Sound velocities for air (at different temperatures and values of humidity), water and piezo electric materials. With data from [Krautkrämer & Krautkrämer 1990].	5
Table 2.2: Phase refractivity of Dry Air with 450 ppm CO ₂ ($\lambda = 633$ nm). Values by [Ciddor 1996].	15
Table 3.2: Settings for sound field measurement and surface scan. Some settings were maintained from the work of López Baos (2018)	31
Table 4.1: Results of the phase velocity obtained from the transient sound fields for three different sections. Section 1: 20 mm to 50 mm, Section 2: 50 mm to 100 mm, Section 3: 20 mm to 100 mm. The velocities are all given in [m/s].	47
Table 4.2: Maximum measured voltages and calculated SPL (considering the amplification) for the sound field of each measured transducer. *The recording range for the ULT200 was set too low, thus data clipping occurred.	48
Table 4.3: Wavelengths of the transducers (measured and calculated)	51
Table 4.4: Extracted values of the sound fields compared with calculated values.	56
Table 4.5: Maximum values of the measured displacement and velocity for various configurations. The physical quantities were calculated with the conversion factors 50 nm/V for displacement and 100 mm/s/V for velocity	67

Appendix

Appendix A CLSM images of transducer surfaces

Microscopic images of the CF400 transducer surface, obtained by overlaying optical and laser data, are found in 0. The outer ring, seemingly covered by a tape, has a different structure than the uncovered area.

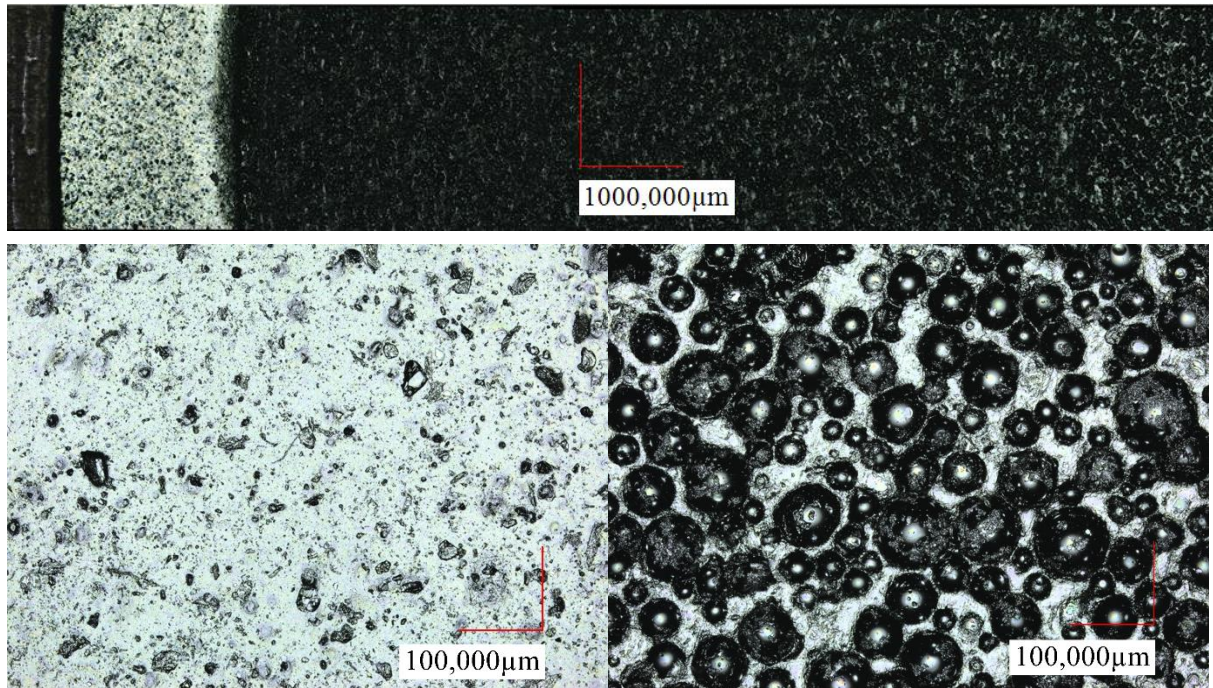


Figure A-1: CLSM images of the CF400 transducer surface (combined laser+optical). Upper image: overview of a section of the surface (5x magnification). Lower left: Area covered with tape-like material, corresponding to white section in the upper image. Lower right: Uncovered area, same measurement as Figure 3.6. Both lower images were measured with 20x magnification

Images recorded with the same measurement setup for the ULT200 transducer are depicted in 0.

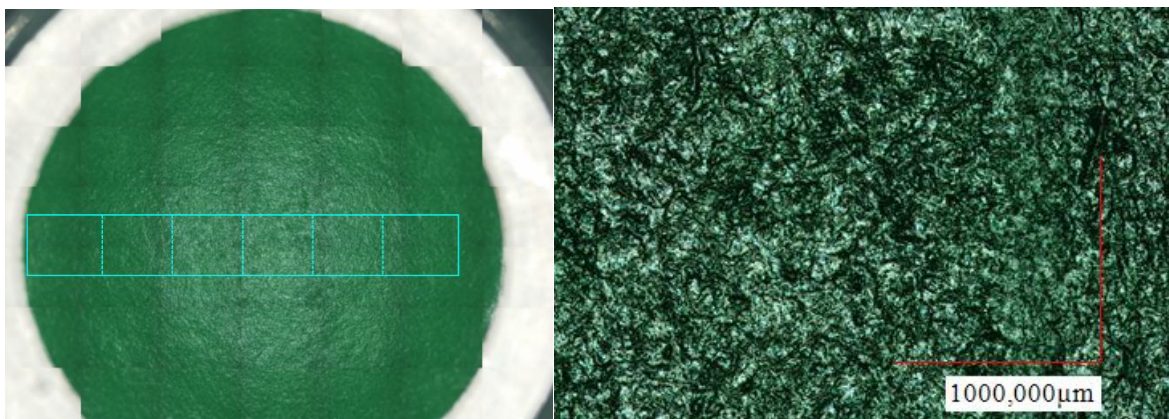


Figure A-2: CLSM images of the ULT200 transducer surface. Left: overview of scanning area for profile line in Figure 3.5. Right: combined laser+optical image recorded with 20x magnification.

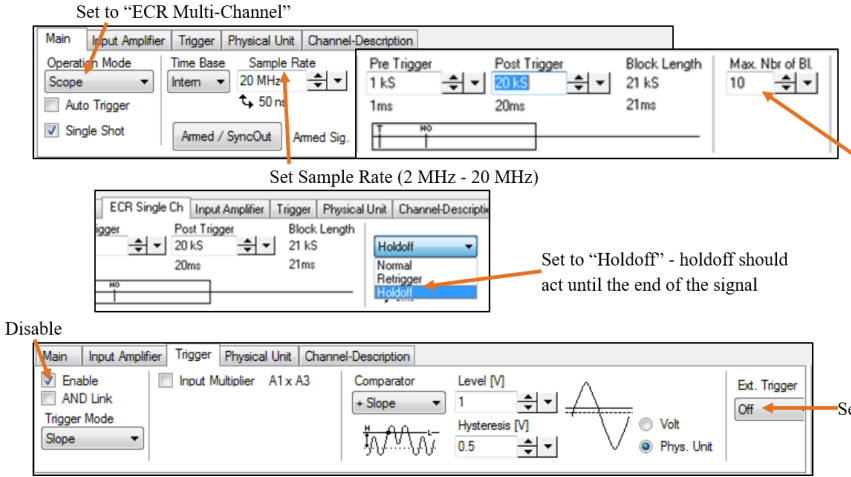
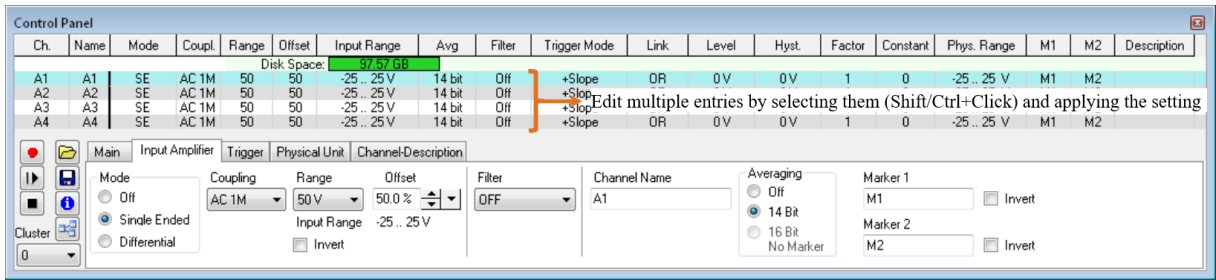
Appendix B Measurement Procedure

The following is a step-by-step instruction to set up and perform the measurements as described in this thesis. It is assumed that the CNC table, optical microphone and amplifier/encoder are set up as they were for the duration of this work. Depending on the current state of the general setup, some steps may need to be added or omitted which may not have been considered here. One important step when switching measurement directions is to attach the encoder cable (orange cable) to the correct axis (“Line” axis). Otherwise, the trigger signal will not be sent as it should. It is also recommended to read the “SonoStudio User Manual” in the Appendix of López Baos (2018) and the TranAX user manual [KL/TBE 2014], chapter 6.4 describes the ECR mode in more detail.

- If the Vibrometer is used: Set up the tripod, fasten the mounting plate to the vibrometer head (3/4” thread) and secure it to the tripod (it clicks when its fastened).
- Set up the decoder on a table (the oscilloscope can later be placed on top of the decoder)
- Carefully (!) mount the cable connecting the vibrometer head to the decoder. Apply a tension relief: Use the tripod handle as fastening point. Be sure not to apply excessive torsional force to the cable, as it is extremely fragile.
- Start by setting up the TranAX oscilloscope on a table, connect all power cables and the BNC cable(s) coming from the measurement device to the first (3) input(s) on the back (depending on whether the vibrometer is used).
- Connect the BNC trigger cable with the oscilloscope: You will need a male-to-male adapter and the BNC to ext.-trigger input adapter for this. The second adapter has its corresponding input labeled on the oscilloscope. This setup permits an easy configuration in the oscilloscope software
- Set up the transducer and measurement device according to the experiment needs. If a plate is tested, the blue mounts can be screwed to the rails in the CNC table and the plate fixed to them.
- Power up all five devices: Encoder, Amplifier, Opt. Microphone/Vibrometer, Laptop and Oscilloscope
- Press the orange lighted button on the encoder to unlock the axis of the CNC table
- Start “SonoStudio” on the laptop and “TranAX” on the oscilloscope.
- TranAX-Software: Activate the Channels to which BNC cables are connected and set the measurement frequency and Voltage Ranges for each of them. Set “Ext. Trigger” to “+Slope” and change the mode to “ECR Multi-Channel”. Then, set the number of blocks in a file to the desired value and apply your trigger settings (pre-trigger, trigger and holdoff)

-
- If the measurement device is powered up already (wait 5 min. for the lasers to calibrate) you should get a read out on the oscilloscope. Press the “F6” key to start data acquisition and you should see some graphs appearing in the read-out screen. If not, simply select the channel icons in the window to the left and drag them onto the green screen, then the data should appear.
 - Open the “TransAS” folder on the oscilloscope computer and delete all files in it. This makes it easier to identify the files written by your measurement afterwards. It is good practice to do this after every measurement and especially after the last one on a day.
 - SonoStudio-Software: Start by moving the CNC table to the correct position. This can be done with the cog-icon in the middle of the screen (also see 0). Be sure that nothing is in the way, as the table will take the direct path to the set point. You can also specify the desired location axis-by-axis i.e. first move the table to the desired x-location, then y and then z.
 - If you need to change the measurement directions from the default (i.e. from xz-plane to yz-plane or vice versa), change the “Isel*AxisMeanderDirection” (where * stands for either X, Y or Z) settings (accessed by clicking “Settings” in the top left). Don’t forget to save by clicking the disk symbol; it’s better to click it twice and reopen the settings window to make sure the settings really have been saved. After that, be sure to reposition the orange decoder cable to the appropriate axis (The one with “Line” in the settings)
 - If you don’t trust the CNC machine or the software, additionally set the “Isel*AxisMin” and “Isel*AxisMax” values so that the arm cannot go over a certain coordinate. This might lead to an unexpected “Workspace Violation” error when the starting point coordinate + line length is the limit value, as the final position is usually 0.25 mm over the set distance. The error can be resolved either by decreasing the “Line length” or adjusting the limits
 - Set the signal generator according to López Baos (2018). You can additionally set the “Averaging Number” if you want averaged recording of the data. Keep in mind that the “Averaging Period” setting gives the time after which the next averaging pulse is sent, so the same limits for data storage apply as with “Pulse Period”. Additionally, the table does not stop during the averaging, so there is a finite distance between averaging points. Each data point is at the current time saved as separate measurement, as no on-line averaging method could be found in the Multi-Channel ECR mode of the oscilloscope. The averaging is then carried out in post-processing.
 - Set the mechanical parameters in the “Position Device” window according to López Baos (2018). The settings used for the measurements in this work are summarized in Table 3.2. Be sure to click the “Set” button to set the scan origin when you are satisfied with the current position.
-

- To start the scan, move the scanning head away from the scan origin. This gives you time to start the oscilloscope after you hit “Start Scan” in SonoStudio. As no trigger is sent while the table is moving to the scan origin, this is the only method of aligning the first data point of the oscilloscope with the first trigger signal sent by the encoder.
- Press “Start Scan” in SonoStudio, then hit “F4” in the oscilloscope to start the auto-sequence before the scan origin is reached. Enjoy the measurement (it normally takes about 5-10 Minutes)
- After the scan is completed, hit “F6” quickly to terminate the data recording without too much excess data. Locate the “*.bdf” files that were written during the measurement in the “TransAS” folder on the oscilloscope computer. Copy the files to a folder created specifically for this measurement (without any other files in it). Copy the address of the folder with the files in it.
- In the TranAX-software, go to View -> Formula-Editor. This should show a file converting the .bdf files to .tpc5 files which can be processed by Matlab. Paste the address of the folder with the files you want to convert in the “directory name” variable. Execute the script and wait for it to finish. (3-5 Minutes together with the step before)
- Copy the .tpc5 files to an external hard drive / USB drive. (~2 Minutes depending on Measurement Size)
- Copy the files to your computer with Matlab installed and open the “TPC5toMATimproved_final.m” script. To execute this script, you need the functions “AvAndSetNan.m”, ”convert2VolumeScan.m” and “MegaEinleser_2018_11_12.m”. Execute the script.
- Enter the measurement settings you previously set in SonoStudio and information regarding flipping the data and filtering. If you perform multiple measurements with exactly the same settings, you can import the “Settings.mat” file of an earlier measurement and only change the “directory” variable to match the new measurement folder.
- Wait for the Script to finish. (10-20 Minutes)
- Now you have two (or four, depending on the measurement device) new files in the folder with the data files. All .mat files containing measurements are three dimensional matrices. The row dimension of the matrix is also the row (i.e. horizontal) dimension in the scanning process; the same applies for the column dimension. The third dimension is time, i.e. the samples of the individual A-Scans are saved here. Using `imagesc(VScan(:, :, index))` or will therefore plot the recorded data for the time instant "index" in the correct orientation according to the measurement settings. The settings used for the Scan are saved in the "Settings.mat" file.
- With the volume-scan as .mat file, you can easily apply any other script to visualize the data (see Appendix C).



Set number of blocks in each file such that the file transition overlaps with a line change of the CNC table. E.g., if one measurement line consists of 201 measurement points, the block number could be set to 201, 402 or 603... files. It is advisable although not necessary to set the number of blocks such that the last point of measurement corresponds to the last block in a file.

Figure B-1: TranAX software with important annotations.

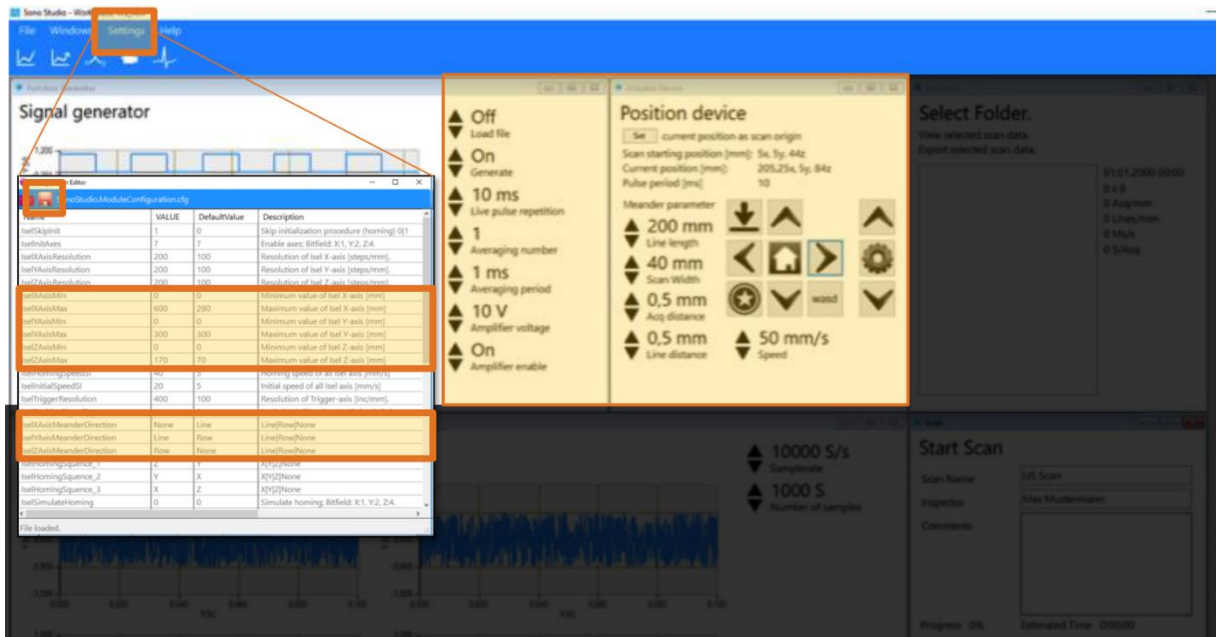


Figure B-2: SonoStudio user interface with highlighted important areas.

Appendix C MATLAB code

```
%This Script Changes the Settings.mat of each subfolder to the current one
%(useful if working on more than one computer) and makes one struct (d)
%with all the subfolder's names
%Construct Matrix with Folder Names
pathFolder = pwd;
d = dir('*100x40*');
isub = [d(:).isdir]; %# returns logical vector
nameFolds = {d(isub).name}';

%Add each element to path
for i = 1:length(d)
    direct = [d(i).folder '\\' d(i).name];
    settings.load([direct '\\' 'Settings.mat']);
    settings.directory = direct; %Change directory in settings directory of
the file on this computer
    save(strcat(direct, '\\', 'Settings'), '-struct', 'settings');
end

function signalOut = AvAndSetNan(signalIn, avNum, leng, samp)
%Averages the Data while Masking out the Data Blocks where Clipping occurred
% Specify clipVal as the maximum value a data point can take, dif is
% used to account for asymmetries from + to - and threshold specifies
% how many data points have to be clipped so that a block gets excluded
% from averaging.

if avNum == 1 %Exit if there is no averaging to be made
    signalOut = signalIn;
    return;
end

st.ma = max(max(signalIn));
st.mi = min(min(signalIn));
dif = abs(st.ma-abs(st.mi))*1.1; %Difference is 10% larger than difference
of min and max values
if st.ma > st.mi
    clipVal = st.mi;
else
    clipVal = st.ma;
end
thresh = 0.01 * samp; %Mask out Data if 1% is clipped

temp = reshape(signalIn, avNum, leng, samp); %Rearrange for calculating
mean
bool = (abs(abs(temp)-clipVal) < dif); %Vector is true if the value is less
than dif away from the clipVal
bool = sum(bool,3) > thresh; %Third dimension is sample dimension
bool = repmat(bool,1,1,samp);
temp(bool)=NaN;
temp1 = mean(temp, 1,'omitnan'); %Calculate mean without NaN Values
signalOut = squeeze(temp1);

end
```

```

%This File assumes that ALL FILES HAVE THE SAME SETTINGS (samples, block
%numbers, measuring frequency, voltage settings etc.) so you NEED to have
%your files from different measurements
%in different folders and only execute this script for one single CScan.

%The Script will also only work if the number of total measurement points
%does not exceed the number of points in each file times the number of
files,
%so there MUSTN'T be any extra data.

%The Script will output two .mat files:
%One with the Volume-Scan in a three-dimensional matrix. The row dimension
of the matrix is also the row (i.e. horizontal) dimension in the scanning
process; the same applies for the column dimension. The third dimension is
time. Using imagesc(filt(:,:,index)) or imagesc(CScan(:,:,index)) will
therefore plot the recorded data for the time instant "index" in the cor-
rect orientation according to the given specifications.
%One with the settings of the scan used for plotting the CScan

%Values for ommitting extremely clipped data (from speckle noise)
clipVal = 10.0;
dif = 0.3;
thresh = 100; %Set to high values if you want to include clipped data

% Populate Settings-Structure to use later and to save for the generation
% of CScans
d = input('Are the settings already in the workspace? y/n: ', 's');

if strcmp(d, 'n')
    directory = input('Copy the name of the folder you want to convert
(should be a subfolder of the folder of this script): ', 's');%[pwd '\\' in-
put('Copy the name of the folder you want to convert (should be a subfolder
of the folder of this script): ', 's')];
    transducerFreq=input('Excitation/Nominal frequency of the transducer
(in kHz): ')*10^3;
    Acq=input('Enter ACQ distance set in SonoStudio: ');
    Line=input('Enter Line distance set in SonoStudio: ');
    SCAN_L=input('Enter value of "Line length": ')/Acq+1;
    SCAN_W=input('Enter value of "Scan width": ')/Line+1;
    samples = input('Enter no. of samples that have been recorded by the
oscilloscope in each measurement block: ');
    fs = input('Enter measurement frequency (inb MHz): ')*10^6;
    LinesInFile = input('How many lines of measurement are there in one
file? ');
    AveragingNumber = input('Averaging Number set in SonoStudio? ');
    channels = input('How many data channels were recorded? ');

    leri = input('Was the first movement of the measured object in relation
to how it should be viewed in the image to the left or right? l/r: ', 's');
    if strcmp(leri,'l')
        flip_lr = 1;
    elseif strcmp(leri, 'r')
        flip_lr = 0;
    else
        msgID = 'TPC5toMAT:InputError';
        msg = 'Character not recognized';
        baseException = MException(msgID,msg);
        throw(baseException);
    end
end

```

```

    updo = input('Was the movement of the measuring object in relation to
how it should be viewed in the image up or down? u/d: ', 's');
    if strcmp(updo, 'u')
        flip_ud = 0;
    elseif strcmp(updo, 'd')
        flip_ud = 1;
    else
        msgID = 'TPC5toMAT:InputError';
        msg = 'Character not recognized';
        baseException = MException(msgID, msg);
        throw(baseException);
    end

    vibro = input('Was the measurement performed by the vibrometer (i.e.
should the moving median filter be applied)? y/n: ', 's');
    if strcmp(vibro, 'n')
        vibrometer = 0;
        displacementChannel = 0;
    elseif strcmp(vibro, 'y')
        vibrometer = 1;
        displacementChannel = input('Which channel was the displacement
channel (for filtering static displacement)? ');
    else
        msgID = 'TPC5toMAT:InputError';
        msg = 'Character not recognized';
        baseException = MException(msgID, msg);
        throw(baseException);
    end

    pixels = SCAN_L*SCAN_W;

    settings.directory = directory;
    settings.Acq = Acq;
    settings.Line = Line;
    settings.SCAN_L = SCAN_L;
    settings.SCAN_W = SCAN_W;
    settings.samples = samples;
    settings.pixels = pixels;
    settings.LinesInFile = LinesInFile;
    settings.fs = fs;
    settings.AveragingNumber = AveragingNumber;
    settings.channels = channels;
    settings.flip_ud = flip_ud;
    settings.flip_lr = flip_lr;
    settings.vibrometer = vibrometer;
    settings.displacementChannel = displacementChannel;
    settings.transducerFreq=transducerFreq;

    save(strcat(directory, '\', 'Settings'), '-struct', 'settings'); %save
number of AScans as control measure
elseif strcmp(d, 'y')
    pixels = SCAN_L*SCAN_W;
    %Populate settings-struct
    settings.directory = directory;
    settings.Acq = Acq;
    settings.Line = Line;
    settings.SCAN_L = SCAN_L;
    settings.SCAN_W = SCAN_W;
    settings.samples = samples;

```

```

settings.pixels = pixels;
settings.LinesInFile = LinesInFile;
settings.fs = fs;
settings.AveragingNumber = AveragingNumber;
settings.channels = channels;
settings.flip_ud = flip_ud;
settings.flip_lr = flip_lr;
settings.vibrometer = vibrometer;
settings.displacementChannel = displacementChannel;
settings.transducerFreq=transducerFreq;
save(strcat(directory, '\', 'Settings'), '-struct', 'settings');
else
msgID = 'TPC5toMAT:InputError';
msg = 'Character not recognized';
baseException = MException(msgID,msg);
throw(baseException);
end

for f = 1:length(d)
load([directory '\', 'Settings.mat']);
list = dir([directory, '\*.tpc5']);
membuffer=memory; % For MegaEinleser

%-----
%-----PROGRAM START-----
%-----

%create struct
measurement = struct();

%%%%%%%%%%%%%%%%%%%%%%%%%%%%%%%%%%%%%%%%%%%%%%%%%%%%%%%%%%%%%%%%%%%%%%%%
%read measurement attributes
%%%%%%%%%%%%%%%%%%%%%%%%%%%%%%%%%%%%%%%%%%%%%%%%%%%%%%%%%%%%%%%%%%%%%%%%
fid = H5F.open(strcat(directory, '\',
list(1).name), 'H5F_ACC_RDONLY', 'H5P_DEFAULT');

%read no. of blocks
gid = H5G.open(fid, '/measurements/00000001/channels/00000001/blocks/');
buffer = H5G.get_info(gid);
numBlocks = uint16(buffer.nlinks);
measurement.numBlocks = numBlocks;
H5G.close(gid);
%get number of samples
dset_id = H5D.open(fid, ['/measurements/00000001/channels/'
sprintf('%08d',1) '/blocks/' sprintf('%08d',1) '/raw']);
dspace_id = H5D.get_space(dset_id);
[~, numSamples] = H5S.get_simple_extent_dims(dspace_id);
%volt constants
gid = H5G.open(fid, '/measurements/00000001/channels/00000001/');
binToVoltConstant =
H5A.read(H5A.open_by_name(fid, ['/measurements/00000001/channels/'
sprintf('%08d',1)], 'binToVoltConstant'), 'H5ML_DEFAULT');
binToVoltFactor =
H5A.read(H5A.open_by_name(fid, ['/measurements/00000001/channels/'
sprintf('%08d',1)], 'binToVoltFactor'), 'H5ML_DEFAULT');
H5G.close(gid);
%sample rate
gid = H5G.open(fid, ['/measurements/00000001/channels/' sprintf('%08d',1)
'/blocks/' sprintf('%08d',1)] );

```

```
attr_id = H5A.open(gid, 'sampleRateHertz', 'H5P_DEFAULT');
rate = H5A.read(attr_id, 'H5ML_DEFAULT');
H5A.close(attr_id);
H5G.close(gid);

%Find the correct number of A-Scans even if it does not equal the number of
blocks times
%the number of files
numFiles = SCAN_W/LinesInFile;
ascans = cast(numBlocks, 'double') * numFiles/AveragingNumber; %Number of
AScans that were performed during the test. This number is equal to the
number of pixels in the CScan

if ascans~=pixels
    msgID = 'TPC5toMAT:PixelsAndAscans';
    msg = 'The number of Pixels and the number of A-Scans do not match. Did
you transfer the settings from sonostudio correctly, or are there .tpc5
files missing?';
    baseException = MException(msgID,msg);
    throw(baseException);
end

if numSamples~=samples
    msgID = 'TPC5toMat:Samples';
    msg = 'The number of Settings put in does not match the number in the
files. Perhaps you want to check which one is correct?';
    baseException = MException(msgID,msg);
    throw(baseException);
end

Signals = repmat( struct( 'twoD', zeros(ascans, numSamples), 'temp'
,zeros(numBlocks,numSamples)), channels, 1 );

MeasurementsInFile = SCAN_L * LinesInFile;

%Iterate over Measurement files
for k=1:ceil(numFiles)

    %open file
    fid = H5F.open(strcat(directory, '\',
list(k).name), 'H5F_ACC_RDONLY', 'H5P_DEFAULT');

    %%%%%%%%%%%%%%%%%%%%%%%%%%%%%%%
    %read measurement attributes
    %%%%%%%%%%%%%%%%%%%%%%%%%%%%%%%
    %read no. of blocks
    gid = H5G.open(fid, '/measurements/00000001/channels/00000001/blocks/');
    buffer = H5G.get_info(gid);
    numBlocks = uint16(buffer.nlinks);
    measurement.numBlocks = numBlocks;
    H5G.close(gid);

    %%%%%%%%%%%%%%%%%%%%%%%%%%%%%%%
    %read signals and block attributes
    %%%%%%%%%%%%%%%%%%%%%%%%%%%%%%%
```

```

for i = 1:channels
    Signals(i).temp = zeros(numBlocks,numSamples);
end

for block = 1:numBlocks
    if (k-1)*MeasurementsInFile+block > ascans %This is to ensure that
the number of measurements written aligns with the settings of the user.
        break
    end
    measurement = MegaEin-
leser_2018_11_12(fid,channels,block,membuffer); %In This case, only one
channel is measured
    for i = 1:channels
        Signals(i).temp(block,:)=cast(measurement.(['Channel'
num2str(i)], 'double') * binToVoltFactor + binToVoltConstant;
    end

end

for i = 1:channels
    if sum(Signals(i).temp(end,:)) == 0
        disp(['There might have been data loss in line ' num2str(block)
' of file ' list(k).name ' in Channel ' num2str(i)]);
    end
end

kMeas = k*MeasurementsInFile; %calculate the indices which mark the
start and end of the file that has just been read
kMeasLow = ((k-1)*MeasurementsInFile+1); %CHANGE IT SO THAT THE NEXT
FILE IS ALWAYS APPENDED IN A NEW LINE?

if k*MeasurementsInFile < pixels
    for i = 1:channels
        Signals(i).twoD(kMeasLow:kMeas,:) =
AvAndSetNan(Signals(i).temp, AveragingNumber, SCAN_L, numSamples);
    end
else
    for i = 1:channels
        Sig-
nals(i).twoD(kMeasLow:kMeasLow+ceil(size(Signals(i).temp,1)/AveragingNumber
)-1,:) = AvAndSetNan(Signals(i).temp,AveragingNumber, SCAN_L, numSamples);
    end
end

H5F.close(fid);
end

%Make sure Signal has the right size

for i = 1:channels
    if length(Signals(i).twoD) > pixels
        Signals(i).twoD = Signals(i).twoD(1:pixels,:);
        disp(['Truncating data of channel ' num2str(i) '. Perhaps you wait-
ed too long to end the measurement?']);
    elseif length(Signals(i).twoD) < pixels
        Signals(i).twoD = [Signals(i).twoD; zeros(pixels-
length(Signals(i).twoD), samples)];
        disp(['There might have been data loss in the measurement, or the
scan values were not set correctly. Filling up the missing data of channel
' num2str(i) ' with zeros...']);

```

```
    end
end

for i = 1:channels
    if i == displacementChannel
        VScan = con-
vert2VolumeScan(settings,Signals(i).twoD,flip_lr,flip_ud,vibrometer,1);
    else
        VScan = con-
vert2VolumeScan(settings,Signals(i).twoD,flip_lr,flip_ud,vibrometer,0);
    end

    save(strcat(directory, '\', 'VolumeScan_Ch', num2str(i)), 'VScan');
    disp(['Saved data of channel ' num2str(i) ' to ' directory
'\VolumeScan_Ch' num2str(i)]);

end

disp('Done. ');
end
```

```

%-----
% Name: CScan_GENERATOR
%
% Description: Generation of a C-Scan from the signal data vector
%              Air-coupled Ultrasound testing
%
% Author: David Kulla & Andres Lopez Baos
%
% Date:        05.07.2018
%
% Last update: 31.01.2019
%-----
%% 1st SECTION: Scan parameters

%INSTRUCTIONS OF USE:
%           1) Generate 3-dimensional matrix and settings file
with
%           TPC5toMATimproved
%           2) Set issoundfield and make sure the variable names
%           are referenced correctly
%           3) RUN the program

issoundfield = 1; %1 for sound field, 2 for transducer surface scan or
CScan of a plate, any other number just exits the program

for f = 1:length(d)
    close all;
    clear Signal Signal1 Signal_filt Signal_fft fft T_max CScan filt tpd
    voltagevalues;
    directory = [d(f).folder '\' d(f).name];
    load([directory '\' 'Settings.mat']);
    load([directory '\' 'CScan1.mat']);
    directory = [d(f).folder '\' d(f).name]; %repeat since settings would
    otherwise overwrite directory
    filename = [directory '\' 'CScan_Power_6dB_relative'];

    %% 2nd SECTION: Lecture of the signal data vector

    if issoundfield == 1
        T_max = rms(CScan,3).^2; %Calculate signal power with square of RMS
    elseif issoundfield == 2
        T_max = rms(filt,3).^2;
    else
        return
    end

    T_max(T_max==0)=NaN; %Mark corrupted data points

    %Back up of the data
    voltagevalues = T_max;

    %% 3rd SECTION: Digital Signal Processing and C-Scan
    %Note: when having a back-up file RUN only this section

    % Change from linear to logarithmic scale

```

```

T_max = (10.*log10(T_max)+300)-300; %Same functionality as pow2db, but
doesnt give error at 0

scanlength = (SCAN_L-1)*Acq;
scanheight = (SCAN_W-1)*Line;

if issoundfield == 1
    Vol_max(f) = max(max(max(abs(CScan))));
    SPL(f) = 20*log10(Vol_max(f)/(5*10^(-3))/(2*10^(-5))); %Calculate
recorded sound-pressure level
    x = [5 scanlength+5]; %Shift x axis by 5 mm to account for minimal
distance
    y = [-scanheight/2 scanheight/2]; %Arrange limits so that y=0 is the
center line
    clim = [min(min(T_max)) max(max(T_max))]; %Same as standard im-
agesc() without clim specified.
    pos=[4,519,1073,459]; %For sound fields on 1080p monitor
elseif issoundfield ==2
    T_max = fliplr(T_max); %Depending on scan settings, this might not
be correct!
    x = [-scanlength/2 scanlength/2]; %Arrange axis so that (0,0) is in
the center
    y = [-scanheight/2 scanheight/2];
    CA_max(f) = mean(mean(T_max(ceil(SCAN_W/2)-
10:ceil(SCAN_W/2)+10,ceil(SCAN_L/2)-10:ceil(SCAN_L/2)+10)))+3; %Max Value
for colorbar
    clim = [CA_max(f)-10 CA_max(f)];
    pos=[2, 42, 954, 854]; %For Transducer Surface on 1080p monitor
else
    return
end

% C-Scan matrix Generator:
h = figure('Position',pos);
imagesc(x,y,T_max, clim)
c = colorbar;
c.Label.String = 'Relative Signal Power';

ylim([y])
xlim([x])
daspect([1 1 1])
if issoundfield == 1
    xticks([5 10 20 30 40 50 60 70 80 90 100]); %Manual xticks, only
correct for 100mm scan length
    ylabel('z-Axis [mm]')
    xlabel('x-Axis [mm]')
    title('Power Distribution - Sound Field')
elseif issoundfield == 2
    ylabel('z-Axis [mm]')
    xlabel('y-Axis [mm]')
    title('Power Distribution - Surface Scan')
else
    return
end

%set(gca, 'YDir', 'normal') %Reverse Y axis direction to yield right-
handed coordinate system
set(gca, 'fontsize',20)

```

```
set(gcf, 'color', 'w');
set(findall(gca, 'Type', 'Line'), 'LineWidth', 2);
frame = getframe(h); %for writing to image/video
im = frame2im(frame);
[imind, cm] = rgb2ind(im, 256);

savefig(filename); %Save as fig and png
imwrite(imind, cm, [filename '.png'], 'png');

close all;
end
```

```

% The CScan will be plotted as "seen" by the sensor, a mirroring in the
% up-down direction can be additionally applied if a scan of an object is
% performed while the sensor is still

issoundfield = 2; %1 for sound field, 2 for transducer surface scan or
CScan of a plate
if issoundfield == 1
    amp = [3 3 5 5 5 2.5 2.5 5 2.5 2 2 2 2.5]; %Amplitudes to use for
Soundfields
elseif issoundfield == 2
    amp = [10 10 10 5 10 10 0.5]; %Amplitudes to use for Vibrometer
else
    return
end

for f = [1 2 3 4 6 7] %1:length(d)
    close all;
    clear Signal Signal1 Signal_filt Signal_fft fft T_max CScan_filt tpd
voltagevalues;
    directory = [d(f).folder '\' d(f).name];
    load([directory '\' 'Settings.mat']);
    load([directory '\' 'CScan3_filt.mat']); %Pay attention, as the matri-
ces might load as different variables (in old measurements)
    directory = [d(f).folder '\' d(f).name]; %repeat since settings would
otherwise overwrite directory

    scanlength = (SCAN_L-1)*Acq;
    scanheight = (SCAN_W-1)*Line;

    if issoundfield == 1
        startframe = 1; %First frame of the video
        endframe = 1000; %Last frame of the video
        x = [5 scanlength+5]; %Shift x axis by ...mm to account for minimal
distance
        y = [-scanheight/2 scanheight/2]; %Arrange limits so that y=0 is the
center line
        pos=[4,519,1073,459]; %For sound fields on 1080p monitor
    elseif issoundfield == 2
        CScan = fliplr(filt);
        startframe = 220;
        endframe = 3200;
        x = [-scanlength/2 scanlength/2];
        y = [-scanheight/2 scanheight/2];
        pos=[2, 42, 954, 854]; %For Transducer Surface on 1080p monitor
    else
        return
    end

    filename = [directory '\' 'CScan_2D_skip1_Ch3_Lowamp'];
    skipframes = 1; %How many data points to skip between images

    v = VideoWriter([filename '.mp4'], 'MPEG-4');
    open(v);
    h = figure('Position',pos);
    clim = [-amp(f) amp(f)];

    for i=startframe:skipframes:endframe
        imagesc(x,y,squeeze(CScan(:,:,i)), clim)
        colormap(gray);
        c = colorbar;

```

```
c.Label.String = 'Amplitude [V]';

ylim(y)
xlim(x)
daspect([1 1 1])

if issoundfield == 1
    xticks([5 10 20 30 40 50 60 70 80 90 100]); %Manual xticks, on-
ly correct for 100mm scan length
    ylabel('z-Axis [mm]')
    xlabel('x-Axis [mm]')
    title(['Sound Field (Time-Evolution) - Time: '
sprintf('%5.1f',i/fs*10^6) '\mus / ' sprintf('%5.1f',samples/fs*10^6) '
\mus'])
elseif issoundfield == 2
    ylabel('z-Axis [mm]')
    xlabel('y-Axis [mm]')
    title(['Surface Scan (Time-Evolution) - Time: '
sprintf('%5.1f',i/fs*10^6) '\mus / ' sprintf('%5.1f',samples/fs*10^6) '
\mus'])
else
    return
end

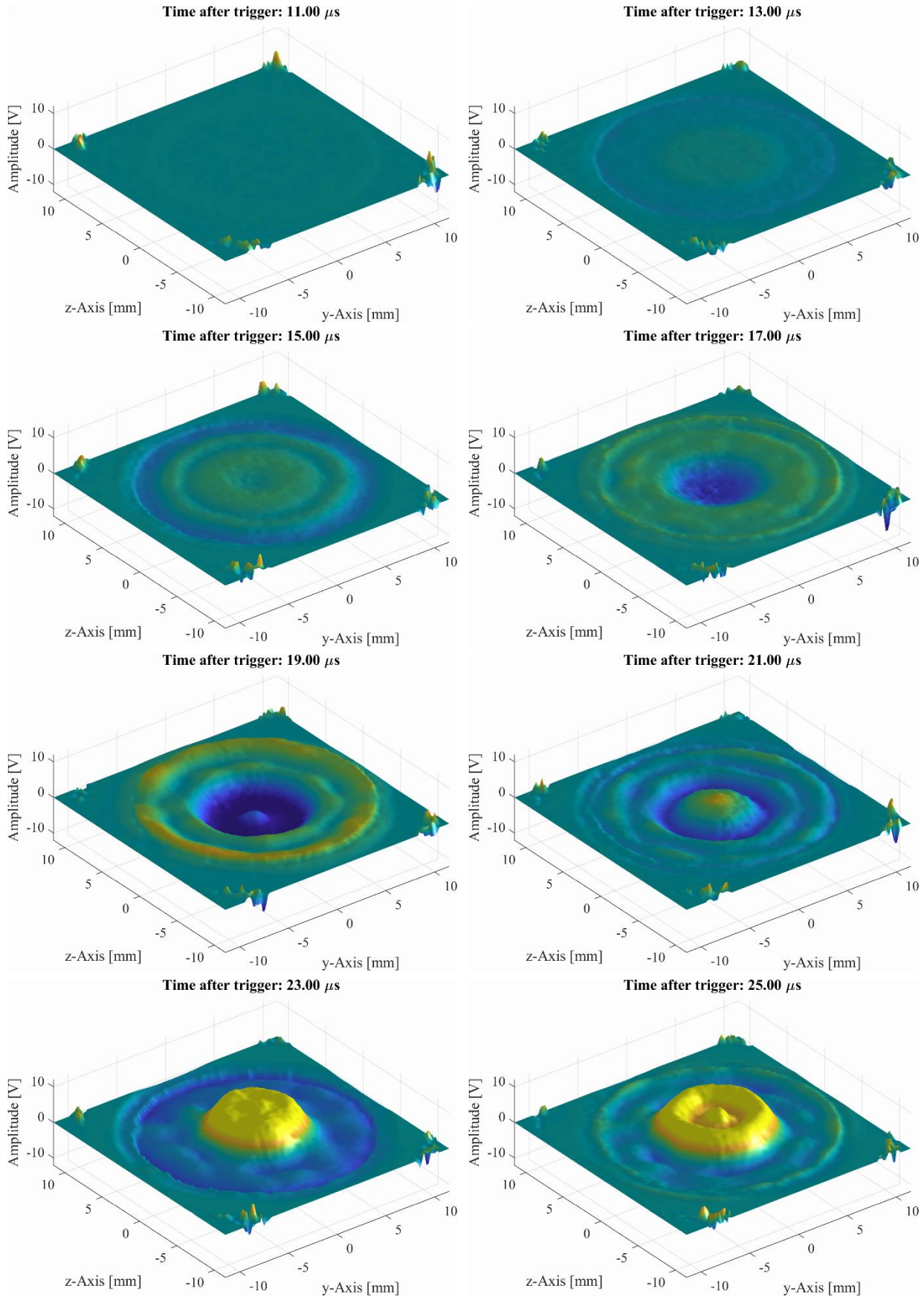
%set(gca, 'YDir', 'normal') %Reverse Y axis direction to yield
right-handed coordinate system
set(gca, 'fontsize',20)
set(findall(gca, 'Type', 'Line'), 'LineWidth',2);
set(gcf, 'color', 'w');

frame = getframe(h); %for writing
writeVideo(v, frame);

end
close(v);

end
close all;
```

Appendix D Data of Electronically Focused Transducer



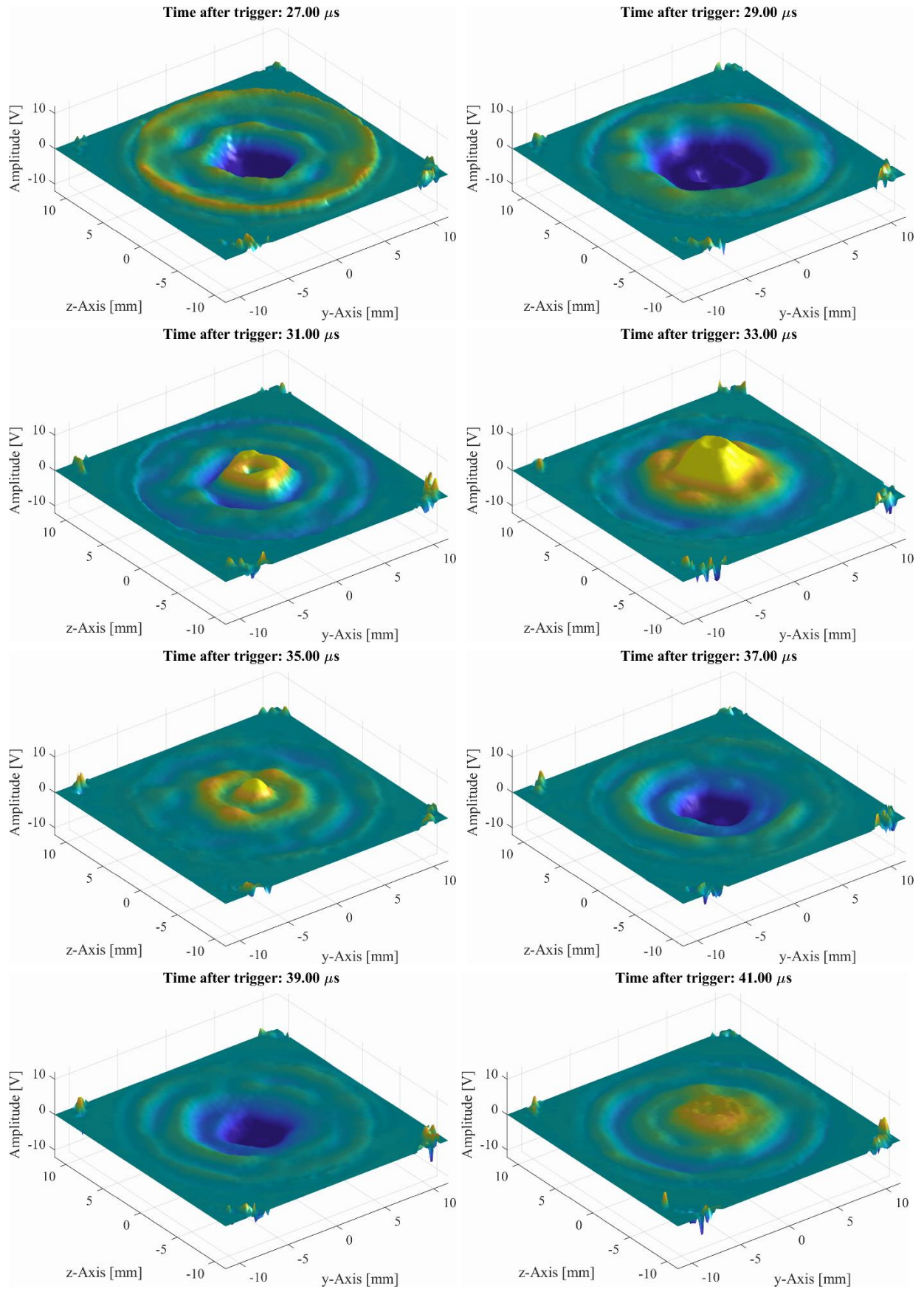


Figure D-1: Frames of the surface scan with 2 μs time difference (displacement data). Transducer: CF400-3E with phase shift 0-900-1800 ns (100 V, 5 pulses).

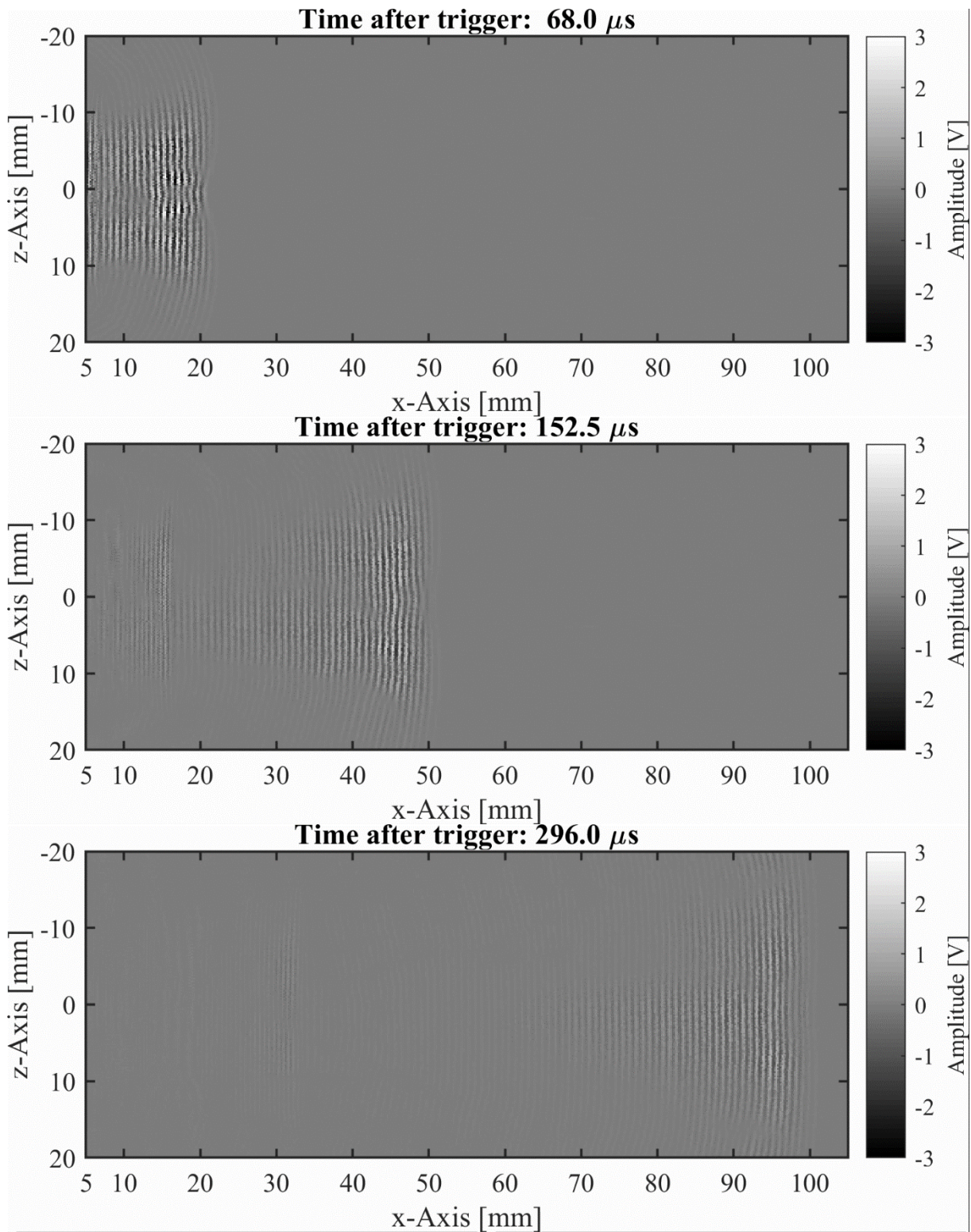


Figure D-2: Extracted frames of the sound field time-evolution. Transducer: CF400-3E with phase shift 0-2255-4246 ns. The same plotting conventions as in Figure 4.1 apply.

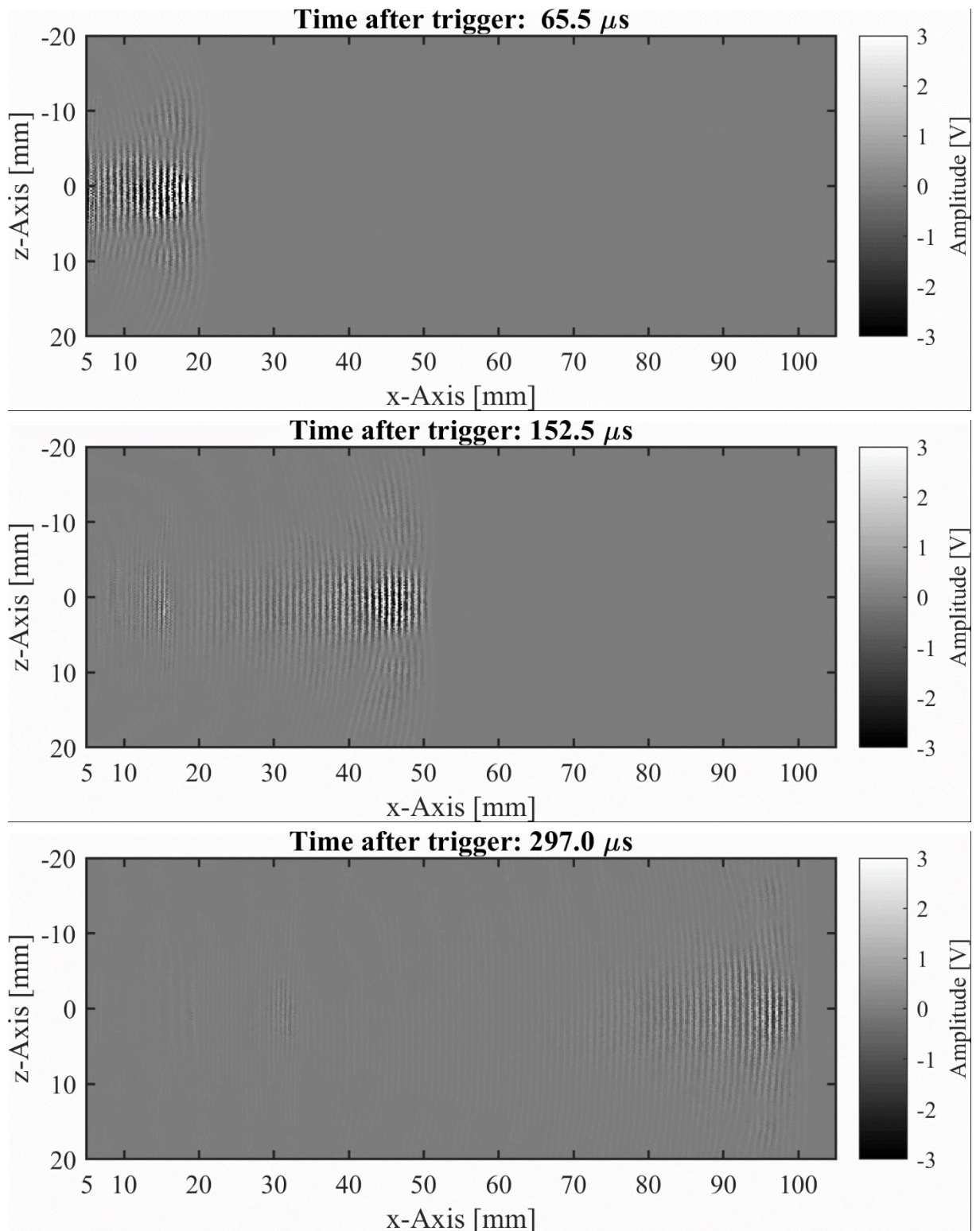


Figure D-3: Extracted frames of the sound field time-evolution. Transducer: CF400-3E with phase shift 0-900-1800 ns. The same plotting conventions as in Figure 4.1 apply.